DISS. ETH No. 17807

FINITE-FREQUENCY EFFECTS IN GLOBAL SEISMOLOGY:

FORWARD MODELING AND IMPLICATIONS ON TOMOGRAPHIC IMAGING

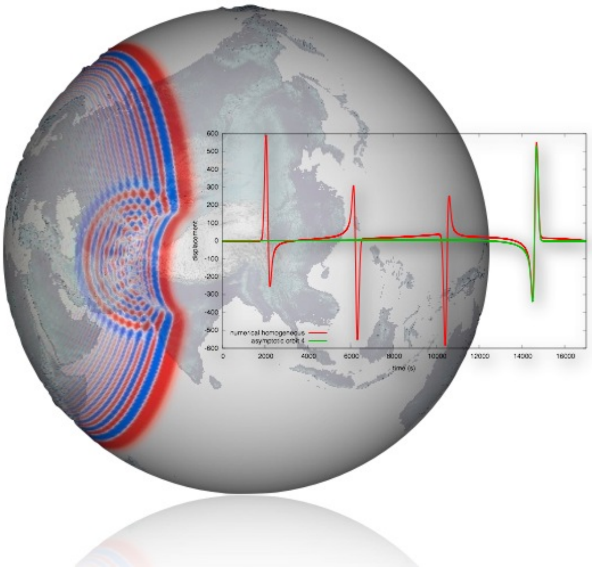
600
500
400
300
200
100
0
-100
-200
-300
-400
-500
-600
displacement
0
2000
4000
6000
8000
10000
12000
14000
16000
time (s)
numerical homogeneous
asymptotic orbit 4

A dissertation submitted to
ETH ZURICH
for the degree of
Doctor of Sciences
presented by
Daniel B. Peter

Dipl. phys. ETH, ETH Zurich
born November 22, 1973
citizen of Sargans, SG, Switzerland

accepted on the recommendation of
Prof. Dr. Domenico Giardini, examiner
Dr. Lapo Boschi, co-examiner
Prof. Dr. John H. Woodhouse, co-examiner
Prof Dr. Jeannot Trampert, co-examiner
2008

Abstract

In seismology, earthquakes can be used to explore the inner structure of our planet. Similar to medical applications of high-energy electromagnetic radiation, seismologists use seismic waves traveling through the body of the Earth to image its interior. These tomographic images show distributions of seismic velocities. Such velocities themselves depend upon material composition and physical properties such as temperature and pressure. Therefore, interpreting these velocity distributions is important to understand the Earth's structure and dynamics.

An important goal in global seismic tomography is to improve the resolution of these velocity models. A promising approach involves the full numerical forward modeling of seismic waves. Most tomographic models of the Earth have not yet made use of it; instead, they almost always relied on ray theory, which simplifies the formulation of both forward and inverse problems. But we have to be aware that ray theory is an infinite-frequency approximation. In practice, this means that it is valid only provided that the wavelength of considered seismic phases is short compared to the spatial extent of Earth's heterogeneities. Obviously, this limits the resolution power, and such approaches fail to detect very small-scale heterogeneities. Especially for low-frequency surface waves, one should ultimately formulate the inverse problem via more accurate descriptions of wave propagation. Finite-frequency theory is such a description, in that it considers the single scattering of seismic waves at small anomalies. Taking this into account, finite-frequency theory replaces rays with complicated kernel functions covering large regions, where seismic measurements are sensitive to heterogeneity.

The first part of my Ph.D. work consisted of computing such sensitivity functions relating seismic phase-delay measurements of surface waves to two-dimensional phase-velocity structures. I combined the computational benefits of a simplified description of forward surface-wave propagation and a time-reversal, adjoint method to construct, by a fully numerical procedure, sensitivity kernels employed in the tomographic inverse problem. In the second part, the effects of such numerical finite-frequency sensitivity kernels upon tomographic imaging were investigated. I compared the finite-frequency and ray-theoretical approaches for both the forward and the inverse problem in global surface-wave tomography. The benefits of finite-frequency theory on tomographic images is demonstrated by a controlled-environment exercise for surface-wave phase-velocity inversions. The third part of this work applies numerical, two-dimensional finite-frequency kernels to derive a high-resolution dataset of dispersion curves for a regional study. With focus on Europe and the Mediterranean region, such datasets are inverted for the three-dimensional, seismic shear-velocity structure of the upper mantle. Conducting an exhaustive search over all possible depth profiles for both, ray-theoretical- and finite-frequency-derived dispersion datasets, the most probable seismic shear-velocity models are found, which were compared to independent studies. Considering the reliability of our derived models, further efforts in improving seismic measurements together with finite-frequency descriptions in inverse approaches will lead to a better knowledge of Earth's structure and processes.

Résumé

En sismologie, les tremblements de terre sont étudiés pour améliorer la connaissance de la structure interne de notre planète. A l'instar de la tomographie médicale, les sismologues étudient les ondes sismiques se propageant à travers la Terre pour en imager l'intérieur. Ces images tomographiques révèlent des distributions de vitesse sismique qui dépendent de la composition minéralogique et des propriétés physiques du sous-sol comme la température et la pression. L'interprétation de ces distributions de vitesse est déterminante pour une meilleure compréhension de la structure de la Terre et de ses processus géodynamiques. Cependant, ces images tomographiques globales restent aujourd'hui encore approximatives.

Un objectif important de la tomographie sismique réside dans l'amélioration de la résolution des modèles de vitesse. Une approche prometteuse implique l'utilisation de modélisations numériques de la propagation des ondes sismiques. Cependant, à ce jour, la plupart des modèles tomographiques globaux ont employé la théorie des rais qui simplifie la description de la propagation des ondes dans les problèmes direct et inverse des études tomographiques. La théorie des rais est une approximation des fréquences infinies. En pratique, elle implique que la longueur d'onde des phases sismiques considérées doit être plus petite que les hétérogénéités que l'on cherche à imager. Cette approximation limite évidemment le potentiel de résolution de cette approche pour détecter des perturbations de vitesse de petite taille, notamment lors de l'utilisation des ondes de surface basse-fréquence. Pour ces dernières, une description plus précise de la propagation des ondes, comme celle énoncée par la théorie des fréquences finies, est nécessaire dans les approches d'imagerie inverse. En effet, la théorie des fréquences finies, qui prend en compte la dispersion des ondes sismiques aux petites hétérogénéités, transforme des rais en noyaux complexes au niveau lequel les mesures sismiques sont sensibles.

La première partie de ma thèse consistait à calculer ces noyaux de sensibilité reliant les mesures d'anomalies des phases sismiques aux vitesses de phases des ondes de surface. Pour cela, les avantages numériques d'une description simplifiée de la propagation des ondes de surface ont été combinés à une méthode adjointe.

Durant la deuxième partie de ma thèse, j'ai examiné les effets de ces noyaux de sensibilité des fréquences finies sur l'imagerie de tomographie globale. Les deux approches basées sur la théorie des rais et celle des fréquences finies ont été comparées dans le cadre des problèmes direct et inverse. La supériorité de la théorie des fréquences finies a été démontrée par des tests synthétiques pour les inversions de vitesse de phase des ondes de surface.

Dans la troisième partie de ma thèse, j'ai utilisé les noyaux des fréquences finies numériques 2D pour dériver un jeu de courbes de dispersion à l'échelle régionale. Pour la région Euro-Méditerranéenne, ces courbes de dispersion ont été inversées pour obtenir le modèle 3D de vitesse de cisaillement du manteau supérieur. Pour chaque courbe de dispersion, dérivée par la théorie des rais et par celle des fréquences finies, une recherche exhaustive des modèles en profondeur a été effectuée pour déterminer les modèles de vitesse de cisaillement les plus probables. La comparaison de ces modèles avec ceux d'études indépendantes suggère que l'approche des fréquences finies est plus cohérente. Néanmoins, l'incertitude dans les modèles dérivés est trop importante pour conclure définitivement; seule une amélioration des mesures sismiques utilisées dans mon étude permettrait de démontrer, de façon probante, l'efficacité de l'approche des fréquences finies.

Contents

Abstract III

Résumé V

1 Introduction 1

2 Membrane waves 9

2.1 Introduction . . . 10
2.2 The forward problem: membrane waves . . . 12
2.2.1 Theory . . . 12
2.2.2 Meshing the Earth's surface . . . 14
2.2.3 Finite-difference scheme . . . 14
2.2.4 Computational considerations . . . 19
2.3 Membrane-wave sensitivity functions . . . 20
2.3.1 A "direct" approach . . . 20
2.3.2 The adjoint approach . . . 24
2.3.3 Some practical considerations . . . 28
2.4 Results . . . 29
2.4.1 Sensitivity kernels for a homogeneous (spherical-Earth) starting model . . . 30
2.4.2 Sensitivity kernels for a laterally heterogeneous starting model . . . 32
2.4.3 A test of the first-order scattering approximation . . . 36
2.4.4 Application to fundamental-mode surface wave tomography . . . 39
2.5 Conclusions . . . 46

3 Resolution benchmark 55

3.1 Introduction . . . 56
3.2 Asymptotic theory for membrane waves . . . 59
3.2.1 Standing waves . . . 59

3.2.2 Traveling waves on a homogeneous membrane 63
3.2.3 Ray theory on a heterogeneous membrane 64
3.3 Benchmark of different approaches to the forward problem 67
3.3.1 Benchmark of ray theory 68
3.3.2 Benchmark of finite-frequency theory 70
3.3.3 Multiple ray-path example 75
3.4 Benchmark of different approaches to the inverse problem 78
3.4.1 Data coverage 78
3.4.2 Scalelength test 80
3.4.3 Noise test 83
3.4.4 Amplitude test 85
3.4.5 Realistic input model test 86
3.5 Conclusions 89

4 European-Mediterranean tomography 95
4.1 Introduction 96
4.2 Data 97
4.3 Method 98
4.4 Results 99
4.5 Discussion 102
4.6 Conclusions 104

5 Conclusions 111

A Petascale Computing 113
A.1 Introduction 114
A.2 Limiting factors of tomographic resolution 114
A.3 Statistically sound, linearized ray-theory tomography 116
A.4 Numerical finite-frequency tomography 118
A.4.1 Implementation and computational cost 119
A.5 Summary 121

Acknowledgments 127

Curriculum vitae 129

1 Introduction

Natural disasters have had and will always have a major impact on human society. Earthquakes can ravage large areas and bring suffering and grief to many people living in such regions. Why and how do earthquakes occur, and which physical laws govern their behavior? We know a lot more today than only a hundred years ago. Still, there are many unanswered questions and more work will be needed to better understand these phenomena. My thesis can only point out a very small aspect of this area of research: namely, the problem of imaging heterogeneous structures within the Earth. Knowledge of Earth's heterogeneity is tremendously important to accurately locate earthquakes, to discriminate nuclear explosions, or to understand physical processes that take place within the Earth.

The tomographic method for seismic imaging began to be developed about three decades ago due to the pioneering work of Keiti Aki and coworkers A. Christofferson and E. Husebye (Aki *et al.* 1977), as well as Adam Dziewonski and coworkers B. Hager and R. O'Connell (Dziewonski *et al.* 1977). Tomography turned out to be very successful in revealing relatively detailed structures within the Earth, giving a present-day snapshot of mantle dynamics, important to understand plate tectonics and its surface expression. Tomographic models also started to play a crucial role in discriminating and validating nuclear explosions for the survey of the nuclear-test-ban treaty.

The main goal of this thesis is to evaluate the performance of different theoretical descriptions of seismic wave propagation in the tomographic imaging process. I examine, in particular, the potential benefits of finite-frequency theory versus ray theory. Ray theory[1] is an infinite-frequency approximation, valid under the condition that the scalelength of heterogeneities be large compared to the wavelength of the propagating wave. In seismology, until recently, almost all tomographic images rely on ray theory, but especially for long-period surface waves the condition of ray-theory validity is not necessarily fulfilled.

---

[1] Ray theory is a concept from optics, were it is very successful in describing and explaining various natural phenomena, such as e.g. the occurrence of rainbows (Descartes 1637). But even simple questions, like e.g. why the sky is blue, must be explained by scattering effects (Rayleigh 1899).

Finite-frequency tomography accounts for first-order scattering (single scattering) of seismic waves, i.e. waves that are refracted and reflected at small-scale heterogeneities in the Earth. Scattered seismic waves arriving at a measurement station interfere with the direct arrivals of seismic phases, perturbing the measurement in a complicated fashion and making it sensitive, in principle, to elastic heterogeneity at any location within the Earth. Perhaps the first question I asked myself at the beginning of my doctoral studies was whether finite-frequency methods can improve the resolution of tomography[2].

Membrane waves and tomographic resolution

How do we identify, in the single-scattering formulation, the sensitivity kernels relating a small perturbation in the measurement to a small variation of the underlying seismic structure? A comprehensive work introducing this issue was conducted by Henk Marquering, together with F. Dahlen and G. Nolet (Marquering *et al.* 1999), introducing the "banana-doughnut" paradox. Marquering *et al.* (1999) clearly showed that the sensitivity of travel-time measurements to Earth structure is actually zero on the ray-theory path, and has its maximum off this ray.

The next challenge resides in implementing the actual computation of such sensitivity kernels. Theoretically, there is one main assumption that is usually made to find analytical expressions for propagating seismic waves, which is the far-field approximation. This approach leads to artifacts, as the earthquake source and the measurement receiver location become mathematical singularities. The fully numerical calculation of sensitivity kernels can avoid shortcomings like this, provided that efficient and accurate algorithms exist, to model the propagation of seismic waves. For example Jeroen Tromp and his Ph.D. students C. Tape and Q. Liu use the adjoint method to numerically calculate the sensitivity kernels in a very efficient way (Tromp *et al.*, 2005). Still, as a result of the forward simulation of seismic wave propagation, the calculation of sensitivity kernels is computationally very expensive (Appendix A investigates this issue for future applications). For seismic surface waves, the forward simulation can be simplified when one considers only surface waves in a narrow frequency-band. This simplified description was introduced as the "membrane surface wave method" by Toshiro Tanimoto (Tanimoto 1990). In this thesis, I use this method extensively to calculate the sensitivity of a phase-delay measurement to a local perturbation in phase-velocity[3].

---

[2] The difference between ray and finite-frequency theory is difficult to describe without proper use of mathematical formulations (see e.g. Dahlen *et al.* 2000 and Nolet *et al.* 2005 for a simplified formulation). Maybe ray theory is a bit like sightseeing with a group of people in a town, but using only the metro. All you will glimpse of the town is the dark, narrow tube of the tunnel in front of you (with a few advertisements that are hanged out at the tunnel's wall). Your view will be very limited while traveling from your departure to the destination location.

With finite-frequency theory, you would take a bus with a comfortable panorama deck to move from point A to point B. You could look everywhere around. Still, we're going to simplify the theory, basically allowing you only one stop in between the departure and destination points. You could choose by yourself where this intermediate stop would be. Then, once you were arriving at the destination, you could exchange your experience with the others of the group and might have a pretty good impression of the city.

The inverse problem in seismology deals with mapping seismic structures, and ultimately the purpose of employing finite-frequency sensitivity kernels is to improve the resolution of tomography. In this sense, I quantify in chapter 2 the performance of the membrane wave method applied to the seismic inverse approach of imaging regional phase-velocity heterogeneity; I first describe the theoretical and numerical background to calculate the corresponding sensitivity kernels for surface-wave phase-delay measurements, then show an application to real data.

Chapter 3 investigates in a more detailed way the resolution potential of this method, using the membrane wave model to generate synthetic measurements; the resolution limit of a ray-theoretical approach can so be compared to a finite-frequency one. In this context, I also address the general problem of poor data coverage and measurement errors in the seismic inverse problem[4].

---

[3] In general, the measurements of phase-delay apply narrow frequency-bandpass filters to recorded seismograms in order to separate distinct surface waves periods from each other (see e.g. Ekström *et al.* 1997). This simplifies the consecutive separation of fundamental- and over-tone surface-wave modes. They lead to global phase-delay databases, which can be inverted for local phase-velocities. The derived phase-velocity models are a compact way of representing these databases, and can be used in a second step to derive the underlying three-dimensional Earth structures (Trampert & Woodhouse 2001).

[4] Panza *et al.* (2007) phrase it in a very nice way: "Seismic tomography is a technique to image the Earth interior with waves generated by earthquakes. The method is comparable to that applied in medical tomography although it is much more complicated because: (1) apart from a few nuclear tests, it is not in our power to locate or time the natural sources of seismic waves (earthquakes); (2) apart from a few ocean-bottom seismographs (OBS), the sensors are located on land and their distribution is discrete; (3) in seismology the ray-path is usually not straight (Nolet 1987). As a consequence of (1) and (2), some areas are sampled by wave paths that mostly go along some preferred direction, while others are not sampled, with obvious consequences of the resolving power of the data. (...)"

Mediterranean tomography

Chapter 4 is devoted to an application of the membrane wave method to a regional, three-dimensional seismological problem. The two theoretical approaches of ray and finite-frequency theory are compared in one focus area, well covered by the data: Europe and the Mediterranean basin. There are various reasons to focus on this region: seismological reference models help to accurately locate earthquake sources and lead also to more accurate descriptions of seismic source mechanisms. They help discriminating natural sources of ground motion from man-made ones, an important step to provide accurate seismic hazard maps without contamination by falsely identified sources (Jimenez *et al.* 2003). An additional goal is to improve the monitoring of nuclear explosions for the comprehensive nuclear-test-ban treaty (CTBT). More accurate global references but also good regional models are needed if one wants to achieve this goal (Pasyanos *et al.* 2004).

The European-Mediterranean region is highly complex due to the interactions between the African, Eurasian and Arabian plates. Throughout the past few million of years, subduction zones, alpine roots and extensional basins were formed (McKenzie 1972). A better knowledge of these complex geological features helps constraining geodynamical modeling and ultimately understand mantle dynamics. In this context, tomographic studies are the most successful tools to provide the necessary boundary conditions. Geodynamical processes take place on all scales, from large-scale mantle flows to micro-scale fluid migrations. Again, there is a need for higher resolution in tomographic models, and, equally important, for estimates of the uncertainties associated with the same models.

How can surface wave tomography help us to find three-dimensional, heterogeneous structures within the Earth? Seismic surface waves are dispersive, i.e. their phase velocities depend on their wavelengths. This is a consequence of the Earth's heterogeneity. Especially in the crust and upper mantle, surface waves are strongly sensitive to perturbations in the velocity of shear waves, and tomographers can then use observations of surface waves to map shear-wave velocity. In chapter 4, I use a two-step procedure to find three-dimensional Earth structure from surface-wave data. Phase-anomaly measurements are first used to map the phase velocity as a function of location. Phase-velocity maps are found for every observed surface-wave period, spanning the whole Earth's surface; thus, at each location the specific surface-wave dispersion curve is determined. The second and final step consists of finding the appropriate seismic velocity-structure as a function of depth, at each surface location, in order to accurately explain the dispersion curve for that particular location (e.g. Panza *et al.* 2007).

My final goal in chapter 4 is to investigate the effects of different theoretical assumptions on the inversions of seismic depth profiles. I therefore employ either ray or finite-frequency theory in order to derive phase-velocity maps at the first step of the procedures described above. The second step is then applied to both resulting databases of surface-wave dispersion. I make use of a high-resolution parameterization over Europe and the Mediterranean region to derive the three-dimensional seismic models for both theoretical approaches and compare the seismic structures revealed by them with those predicted by independent studies of the region's dynamics.

Bibliography

[1] Aki , K., A. Christofferson and E. Husebye, 1977. Determination of the three-dimensional structure of the lithosphere, *J. geophys. Res.,* **82**, 277–296.

[2] Dahlen, F. A., S. H. Hung and G. Nolet, 2000. Fréchet kernels for finite-frequency traveltimes - I. Theory, *Geophys. J. Int.,* **141**(1), 157–174.

[3] Descartes, R., 1637. “La dioptrique” and “Les meteores”. Printed in Oeuvres, Vol. VI, 105-165. 229-366 (Charles Adam and Paul Tanney, eds. 1897-1913. 12 Volumes and supplément. Paris)

[4] Dziewonski, A.M., B.H. Hager and R.J. O’Connell, 1977. Large scale heterogeneities in the lower mantle, *J. geophys. Res.,* **82**, 239–255.

[5] Ekström, G., J. Tromp and E. W. F. Larson, 1997. Measurements and global models of surface wave propagation, *J. geophys. Res.,* **102**, 8137–8157.

[6] Jimenez, M-J., D. Giardini and G. Grünthal, 2003. The ESC-SESAME Unified Hazard Model for the European-Mediterranean Region, *EMSC/CSEM Newsletter*, 19, 2-4.

[7] Marquering, H., F. A. Dahlen and G. Nolet, 1999. Three-dimensional sensitivity kernels for finite-frequency traveltimes: the banana-doughnut paradox, *Geophys. J. Int.,* **137**, 805–815.

[8] McKenzie, D., 1972. Active Tectonics of the Mediterranean Region *Geophys. J. Int.,* 30 (2) , 109—185.

[9] Nolet, G., 1987. In: Nolet, G., Reidel, D. (Eds.), Seismic tomography with applications in global seismology and exploration geophysics. Publ. Company, Dordrecht, Holland.

[10] Nolet, G., F.A. Dahlen, and R. Montelli, 2005. Travel times of seismic waves: a re-assessment. In A. Levander and G. Nolet, Editors, Seismic Earth: Array analysis of broadband seismograms, p. 37–47, AGU, Washington, D.C.

[11] Panza, G. F., A. Peccerillo, A. Aoudia and B. Farina, 2007. Geophysical and petrological modelling of the structure and composition of the crust and upper mantle in complex geodynamic settings: The Tyrrhenian Sea and surroundings, *Earth-Science Reviews*, *80*: p. 1-46.

[12] Pasyanos, M.E., W. R. Walter and S. E. Hazler, 2004. A Surface Wave Dispersion Study of the Middle East and North Africa for Monitoring the Comprehensive Nuclear-Test-Ban Treaty, *Pure and Applied Geophysics*, **158** (8), 1445 – 1474.

[13] Lord Rayleigh (J. W. Strutt), 1899. On the transmission of light through an atmosphere containing small particles in suspension, and on the origin of the blue of the sky, *Philos. Mag.* 47, 375–384.

[14] Spakman, W., S. van der Lee and R. van der Hilst, 1993. Travel-Time Tomography of the European Mediterranean Mantle down to 1400 Km, *Phys. Earth planet. Inter., 79*: p. 3-74.

[15] Tanimoto, T., 1990. Modeling Curved Surface-Wave Paths - Membrane-Surface Wave Synthetics, *Geophys. J. Int., 102*: p. 89-100.

[16] Trampert, J. and J. H. Woodhouse, 2001. Assessment of global phase velocity models, *Geophys. J. Int., , 144*: p. 165-174.

[17] Tromp, J., C. Tape and Q. Y. Liu, 2005. Seismic tomography, adjoint methods, time reversal and banana-doughnut kernels, *Geophys. J. Int., , 160*: p. 195-216.

2 Surface wave tomography: global membrane waves and adjoint methods

2.1 Introduction

2.2 The forward problem: membrane waves

- 2.2.1 Theory
- 2.2.2 Meshing the Earth's surface
- 2.2.3 Finite-difference scheme
- 2.2.4 Computational considerations

2.3 Membrane-wave sensitivity functions

- 2.3.1 A "direct" approach
- 2.3.2 The adjoint approach
- 2.3.3 Some practical considerations

2.4 Results

- 2.4.1 Sensitivity kernels for a homogeneous (spherical-Earth) starting model
- 2.4.2 Sensitivity kernels for a laterally heterogeneous starting model
- 2.4.3 A test of the first-order scattering approximation
- 2.4.4 Application to fundamental-mode surface wave tomography

2.5 Conclusions

This chapter has been published in *Geophys. J. Int.*, 2007. Co-authors were Carl Tape, Lapo Boschi and John Woodhouse.

Summary

We implement the wave equation on a spherical membrane, with a finite-difference algorithm that accounts for finite-frequency effects in the smooth-Earth approximation, and use the resulting “membrane waves” as an analogue for surface wave propagation in the Earth. In this formulation, we derive fully numerical 2-D sensitivity kernels for phase anomaly measurements, and employ them in a preliminary tomographic application. To speed up the computation of kernels, so that it is practical to formulate the inverse problem also with respect to a laterally heterogeneous starting model, we calculate them via the adjoint method, based on back-propagation, and parallelize our software on a Linux cluster. Our method is a step forward from ray theory, as it surpasses the inherent infinite-frequency approximation. It differs from analytical Born theory in that it does not involve a far-field approximation, and accounts, in principle, for nonlinear effects like multiple scattering and wavefront healing. It is much cheaper than the more accurate, fully 3-D numerical solution of the Earth’s equations of motion, which has not yet been applied to large-scale tomography. Our tomographic results and trade-off analysis are compatible with those found in the ray- and analytical-Born-theory approaches.

2.1 Introduction

One of the important challenges in seismology is to enhance the tomographic resolution of the Earth’s interior. A way to achieve this goal is by elaborating more accurate theoretical descriptions of seismic wave propagation and using them to formulate the tomographic inverse problem. The Born approximation (single-scattering theory) represents a possibly significant improvement with respect to simple ray theory; for some time now it has been known to be valid at least for weak scattering in the Earth (Hudson & Heritage 1981; Wu & Aki 1985). On the basis of the Born approximation, the “banana-doughnut” paradox, or the prediction that the sensitivity of seismic travel time observations be maximum away from the ray-theoretical path, was pointed out most clearly by Marquering *et al.* (1999) (but see also Kennett 1972; Woodhouse & Girnius 1982; Snieder 1987; Snieder & Nolet 1987; Li & Tanimoto 1993; Li & Romanowicz 1995); numerous studies have been made to understand the nature of this phenomenon (Dahlen *et al.* 2000; Hung *et al.* 2000; Zhao *et al.* 2000; Spetzler & Snieder 2001; Spetzler *et al.* 2002; Baig *et al.* 2003; Tanimoto 2003; Baig & Dahlen 2004; Tromp *et al.* 2005; de Hoop *et al.* 2005).

The Born approximation, while representing an improvement with respect to simple ray theory, cannot reproduce nonlinear effects that take place in reality (Wielandt 1987; Nolet & Dahlen 2000; Hung *et al.* 2001; Baig *et al.* 2003). In addition, implementations of Born theory found in the literature are typically based on far-field expressions of the wavefield, giving rise to singularities in the computed Fréchet derivatives (sensitivity kernels) (Favier *et al.* 2004). In practice, the forward problem is formulated under the assumption that scattering occurs only at distances from source and receiver much larger than the wavelength, but its solution is then used to compute the values of sensitivity kernels in the vicinity of source and receiver as well, where the kernels are actually singular. This singularity appears to be integrable (Friederich 1999, Appendix E), but it remains unclear to what extent these asymptotic kernels are valid near the source and receiver. Capdeville (2005) proposed an efficient way to overcome this problem in the computation of sensitivity kernels, combining adjoint methods (Tromp *et al.* 2005 and references therein) and normal mode summation, though his approach has not yet been applied in practice to the inversion of real seismic data.

Direct numerical integration of the equations of motion is another way to avoid the far-field approximation, and simulate, at least to some extent, the nonlinear phenomena mentioned above. Computational power has grown tremendously in recent years thanks to a combined improvement in processor performance and in size of multi-processors clusters (Bunge & Tromp 2003; Boschi *et al.* 2007); over the last decade, the average growth-per-year in the computational performance of supercomputers has slightly exceeded Moore's law, which predicts a factor of 2 in 18 months (Strohmaier *et al.* 2005). Seismologists with access to large parallel computers are now able to calculate seismic waves propagating through a three-dimensional, complex medium closely resembling the Earth. Nevertheless, such simulations can take quite a long time even for a single earthquake and on large cluster systems; for example, Tsuboi *et al.*'s (2002) simulation of the Denali earthquake in a very realistic Earth model took about 15 hours on one of the fastest supercomputers in the world. It is therefore too time-consuming to perform the large number of full numerical integrations required to set up an inverse problem numerically unless one simplifies the problem (e.g., Tape *et al.* 2007).

Here we explain how the 3-D problem of fundamental-mode surface wave propagation is represented by a 2-D, zero-thickness membrane analogue. We then use the membrane wave analogue to compute sensitivity functions relating surface wave phase measurements to lateral anomalies in the phase velocity of surface waves. This is a notoriously time-consuming endeavour, but we reduce its cost through the application of an adjoint-method approach (e.g., Tarantola 1984) similar to that of Tromp *et al.* (2005). We apply the sensitivity functions in an inversion of real data to derive phase-velocity maps of the Earth, which we compare in the last part of this work with those obtained from ray-theory and analytical Born-theory tomography (e.g., Spetzler *et al.* 2002; Boschi 2006).

2.2 The forward problem: membrane waves

Membrane waves as an analogue for surface waves were introduced by Tanimoto (1990), to investigate locally the strong effects of lateral heterogeneity on short-period surface waves (10 and 20 s). We follow the same approach to derive a numerical model for the propagation of intermediate-period surface waves at the global scale, which requires special spherical grids and numerical techniques (e.g., Sword *et al.* 1986). In the interest of simplicity, we give only a detailed theoretical treatment of the Love-wave case below. Working with a Rayleigh wave *Ansatz* leads to an algebraically more complicated, but qualitatively analogous derivation (Tanimoto 1990; Tromp & Dahlen 1993).

2.2.1 Theory

Given the equation of motion (Aki & Richards 2002)

$$\rho\ddot{\mathbf{u}} = \nabla \cdot \boldsymbol{\tau}, \tag{2.1}$$

with ρ denoting density, $\mathbf{u}$ displacement, $\boldsymbol{\tau}$ stress, and accompanied by initial conditions accounting for the seismic source, we Fourier-transform it and replace $\mathbf{u}$ with the Love wave *ansatz* (Tanimoto 1990)

$$\mathbf{u}_L = W(r)(-\hat{\mathbf{r}} \times \nabla_1) s(\vartheta, \varphi), \tag{2.2}$$

with $W(r)$ depending only upon depth, and $\hat{\mathbf{r}}$ denoting the unit vector, ∇_1 the surface gradient (e.g. Dahlen & Tromp 1998) and $s(\vartheta, \varphi)$ a scalar "potential" at colatitude ϑ and longitude φ. It follows that for an isotropic stress-strain relation and in the smooth-Earth approximation, s satisfies

$$\nabla_1^2 s + \frac{\omega^2}{c^2(\vartheta, \varphi; \omega)} s = 0, \tag{2.3}$$

valid at each frequency ω and corresponding phase velocity c (Tanimoto 1990; Tromp & Dahlen 1993; Yoshizawa & Kennett 2005). We solve eq. (2.3) numerically in the time domain, with a prescribed initial displacement and source-time function. Notice that we have implicitly assumed the medium to be isotropic, with smooth lateral variations of the shear modulus, so that its gradient can be neglected; in practice, we are restricting ourselves to a similar approximation as those implicit in perturbation (Born) theories based upon ray theory (e.g., Dahlen *et al.* 2000; Spetzler *et al.* 2002).

In order for an analytical solution to be available in the homogeneous Earth case, we prescribe a forcing term

$$f(\vartheta, \varphi) = g(\Delta)\, h(t), \tag{2.4}$$

consisting of an initial displacement

$$g(\Delta) = \frac{e^{-\Delta^2/2\mu^2}}{\mu^2}, \tag{2.5}$$

with $\Delta(\vartheta, \varphi) \in [0, \pi]$ denoting arc-distance from the source, and a source-time function

$$h(t) = \frac{-t}{\sigma^2} \frac{e^{-t^2/2\sigma^2}}{\sqrt{2\pi}\sigma} \tag{2.6}$$

(Tape 2003, eq. 3.31). Here σ and μ act as source parameters, governing the characteristic frequency content of the source. To avoid the introduction of absorbing boundary conditions and to allow for multi-orbit surface wave propagation, the membrane spans the whole globe.

2.2.2 Meshing the Earth's surface

It is impossible to evenly distribute more than 20 points on the surface of the sphere, a distribution of points describing a platonic dodecahedron. Modeling on the sphere at regional scalelengths requires thousands of points, and thus the grids will have at least some undesired irregularities. Spherical geodesic grids of triangular faces, first introduced in the context of meteorological flow modeling (Williamson 1968; Sadourny *et al.* 1968), are one approach to the nontrivial problem of uniformly discretizing the Earth's surface (Cui & Freeden 1997; Saff & Kuijlaars 1997).

In practice, the sphere is first discretized by a platonic solid, i.e. a regular polyhedron consisting of identical cell faces. We find the initial triangular mesh combining the vertices of a dodecahedron and an icosahedron (Tape 2003), also known as a truncated icosahedron or a buckyball. We then refine the grid iteratively, using the midpoints of the three sides of each spherical triangle to divide it into four new smaller triangles, forming the next finer grid. This method will be referred as *dyadic refinement* (Baumgardner & Frederickson 1985). The corresponding hexagonal/pentagonal (in the following loosely referred to as hexagonal) grid is constructed from the triangular grid. The corner of each hexagonal or pentagonal face is found by calculating the central point of each spherical triangle from the corresponding triangular grid. Vertices of the triangular grids then coincide with the cell centers of the hexagonal grids.

As we shall show in the next section, s is evaluated at the vertices of the triangular grid, while the computation of its Laplacian involves the areas of the hexagonal grid cells, so that the properties of both grids are relevant to our implementation. Comparisons in Table 2.1 show that our hexagonal grid has a more uniform distribution than others based on the icosahedron as the initial triangular grid (e.g. Wang & Dahlen 1995; Heikes & Randall 1995a). A further improvement of the distribution could still lead to an even more accurate numerical solution; in the next section we show that our hexagonal grid is sufficiently good to provide a valuable basis for the numerical computations.

2.2.3 Finite-difference scheme

Both global (e.g., spectral) and local (e.g, finite-difference) numerical methods have been applied to meteorological problems associated with spherical geodesic grids (see Stuhne & Peltier 1996; Randall *et al.* 2002). Inspired by the studies of Heikes & Randall (1995a,b), we use a simple finite-difference scheme to compute the Laplacian, which is

Table 2.1: Properties of spherical grids. Comparison between spherical grids based on icosahedral (ico) and icosahedral-dodecahedral (ico-dod) initial platonic solids. The membrane wave calculations use the hexagonal grid based on the second combination of two platonic solids (ico-dod). Values for the icosahedral case are taken from the twisted grid used by Heikes & Randall (1995a).

refinement level		ratio of cell area A_{min}/A_{max}	ratio of cell distance d_{min}/d_{max}
0	ico	0.885	0.881
	ico-dod	0.941	0.894
1	ico	0.774	0.848
	ico-dod	0.914	0.861
2	ico	0.763	0.840
	ico-dod	0.907	0.852
3	ico	0.742	0.838
	ico-dod	0.878	0.850
4	ico	0.736	0.837
	ico-dod	0.870	0.849
5	ico	0.733	0.837
	ico-dod	0.868	0.849
6	ico	..*	..*
	ico-dod	0.868	0.849

* no information

required to solve eq. (2.3) for the wavefield s. The Laplacian of a function $\alpha(\vartheta, \varphi)$ at a cell center point $\mathbf{P_i}$ on the hexagonal grid described above is approximated by

$$\nabla^2 \alpha \Big|_{\mathbf{P_i}} \approx \frac{1}{A_i} \sum_{n=1}^{N} \frac{l_n}{L_n} (\alpha_n - \alpha_i), \tag{2.7}$$

where N denotes the number of edges of the i-th cell (5 or 6), l_n is the length of its n-th edge and L_n the distance between the centers of the i-th cell and of its neighbor, which shares its n-th edge. α_i denotes the value of α at $\mathbf{P_i}$ and α_n the value of α at the centers of the neighboring cells. A_i is the area of the spherical polygon identifying the cell on the sphere's surface. All these parameters are computed numerically at the outset.

Equation (2.7) shows that the calculation of the Laplacian for a given cell requires only information on the neighboring cells. This is why this scheme is said to be a "local" method, in contrast to other “global” numerical implementations like the spectral methods mentioned above. The advantage of local methods is that they can be parallelized in a very efficient way.

We validate eq. (2.7) using spherical harmonic functions Y_{lm} (Dahlen & Tromp 1998, eq. B.11), which are eigenfunctions of the Laplacian operator,

$$\nabla^2 Y_{lm}(\vartheta, \varphi) = -l(l+1) Y_{lm}(\vartheta, \varphi). \tag{2.8}$$

Hence, differences between the numerically evaluated Laplacian of Y_{lm}, and its analytical values, are readily calculated at the location of each cell. We find that differences are not uniformly distributed on the spherical grid; in fact, although errors become very small as soon as we have a sufficiently fine grid, there exist certain cells where, above a certain level, further refinements of the mesh do not reduce the error significantly.

We explain this effect introducing “grid distortion” as the distance between the midpoint of the segment connecting two neighboring cell centers, and the midpoint of the corresponding cell edge, divided by the cell edge length (Heikes & Randall 1995b, section 2). At each cell, we average grid distortion over all its neighbors, and plot the result in Fig. 2.1a. When the plotted value is zero, the cell is symmetric and the grid is not distorted at the corresponding location. We find the Laplacian to be nearly second-order accurate at most gridpoints (see also Heikes & Randall 1995b). A few cells exist with a particularly high distortion (∼2% or less). Table 2.1 confirms, nevertheless, that our grid is more uniform (hence, less distorted) than alternatives found in current literature.

In a numerical simulation relying on eq. (2.7), cells with high distortion will generate non-physical scattered waves. We test the accuracy of the numerical scheme comparing numerical and analytical solutions found for a constant-velocity membrane. Using the source described by equations (2.5) and (2.6), the following analytical solution was determined for example by Tape (2003, equation 3.34):

$$s(\vartheta, \varphi, t) = c^2 \sum_{l=0}^{\infty} (l + \frac{1}{2}) I_l(\mu) cos(\omega_l t) e^{-\omega_l^2 \sigma^2 / 2} P_l(cos(\vartheta)), \tag{2.9}$$

where

$$\omega_l = \frac{c\sqrt{l(l+1)}}{a} \tag{2.10}$$

Figure 2.1: Properties of the hexagonal grid. (a) Distortion measured by the midpoint ratio of distance between cell centers and cell edges to corresponding cell edge length (Heikes & Randall 1995b). (b) Accuracy of Laplacian for a spherical harmonic function ($l = 6$, $m = 1$). Differences between numerical and analytical values are normalized to the maximum value of the analytical Laplacian. View from North Pole down projected onto the equatorial plane.

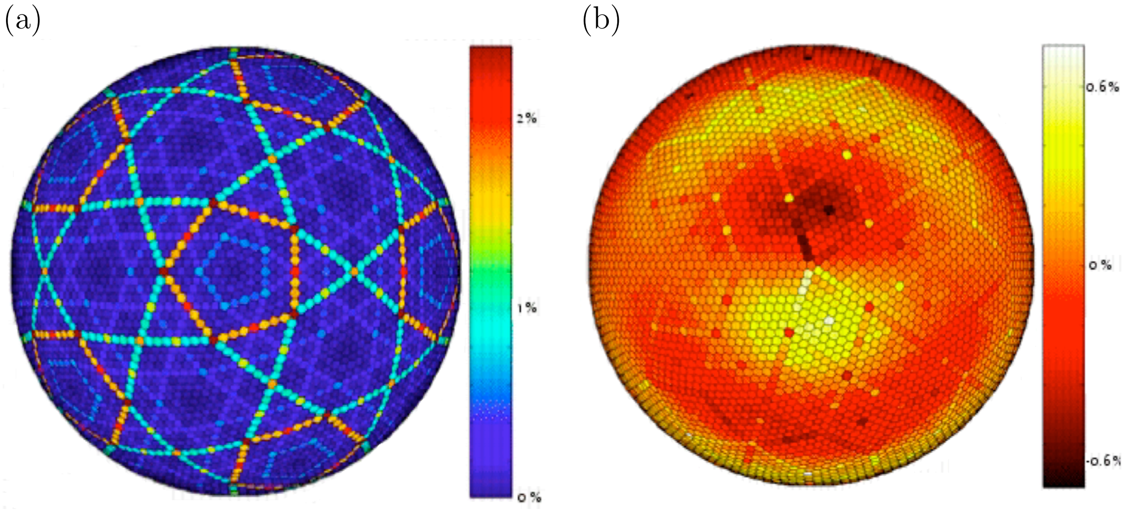

with a the radius of the sphere, and the integrals

$$I_l(\mu) = \int_0^{\pi} P_l(cos(\theta)) \frac{e^{-\theta^2/2\mu^2}}{\mu^2} sin(\theta) d\theta \tag{2.11}$$

are calculated numerically with the Legendre polynomials P_l of angular degree l.

Fig. 2.2 shows a snapshot of the scalar potential solution to the wave equation (2.3) derived numerically over the whole sphere. Fig. 2.3 shows the resulting scalar potential solutions and phaseshifts between the analytical and numerical solutions for Love waves at 150 s period. Phaseshifts are shown for filtered and unfiltered solutions; the simple source mechanism described by equations (2.5) and (2.6) excites a wider range of frequencies, which have to be filtered out in order to isolate the frequency of interest. We examine this in more detail in section 2.3.3.

We find that differences between the analytical and numerical solutions are small enough that the numerical algorithm can be considered valid, and can be applied to evaluate the effects of small lateral heterogeneities, or formulate a tomographic inverse

Figure 2.2: Snapshot of wave propagation on the spherical membrane for a source at the North Pole. Wavefield s is plotted on a spherical-triangular grid with 7682 vertices.

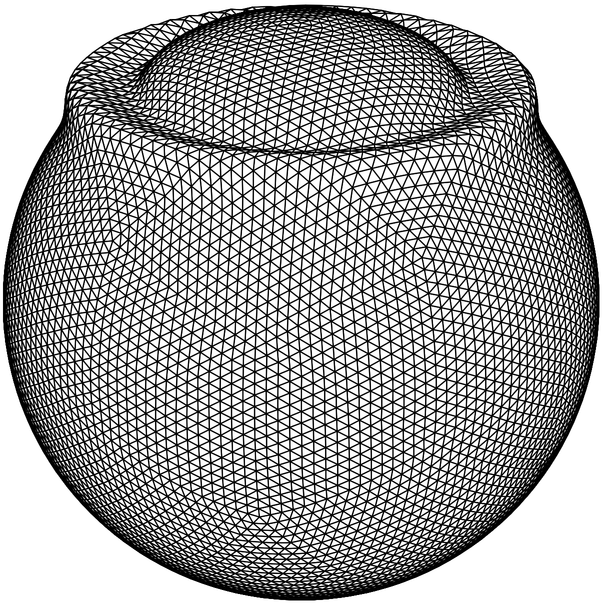

problem. We conduct numerical integrations on the grid defined by 6 successive dyadic refinements, yielding 122,882 hexagonal or pentagonal cells. On the basis of Fig. 2.3, we consider this mesh a good compromise between the cost of further refinements, and inaccuracies introduced by making the grid coarser. The grid spacing, or average distance between the centers of neighboring cells, is ~70 km, corresponding to about 10 grid points per dominant wavelength for the reference case of 150 s period waves.

A final remark concerns the stability of our numerical scheme. If the timestep dt becomes too small, the numerical errors can grow exponentially and become unstable within the time window of the simulation. On the other hand, dt must satisfy

$$dt \leq dx/R, \tag{2.12}$$

where dx is the average distance between grid nodes, and the threshold value R has to be determined as described, e.g., by Moczo *et al.* (2004). In the case of our spherical

Figure 2.3: Accuracy of numerical membrane waves. (a) Analytically (dashed) and numerically (solid) calculated membrane wave s, generated from a source at (0°N, 0°E) and recorded at (0°N, 90°E). (b) Phase-shift between the analytical and numerical, filtered (solid) and unfiltered (dashed) solutions shown in (a), for different levels of grid refinements. Filtering is discussed in section 2.3.3.

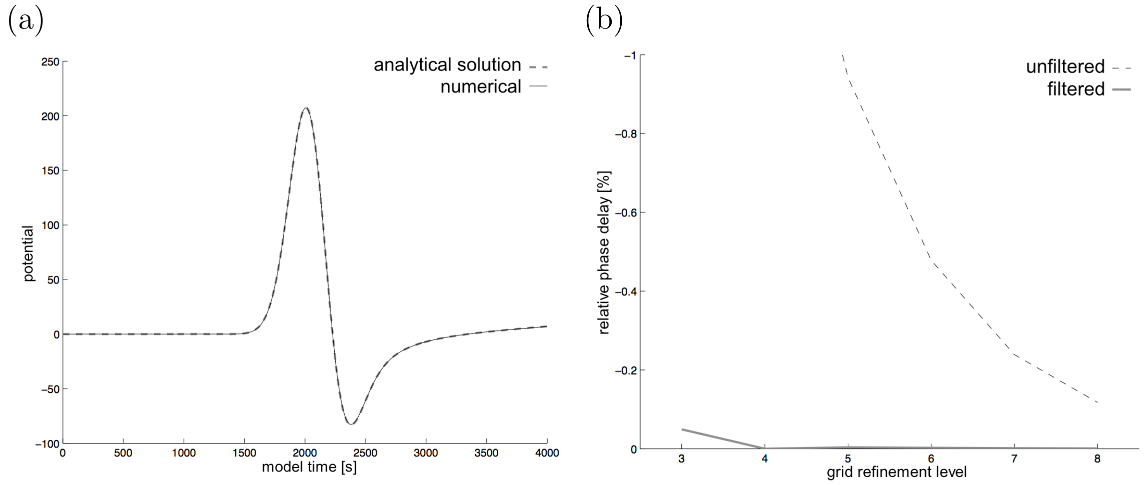

grid, Tape (2003) found empirically

$$dt \approx \frac{dx}{\bar{c}\sqrt{2}}, \tag{2.13}$$

where $\bar{c}$ is the average phase velocity of the model. Simulations with a timestep smaller than (2.13) will require a longer computation time without increasing the precision. The timestep also limits the sampling rate of modeled waves; in section 2.4, we will apply a quadratic interpolation between sampled times to cross-correlate accurately our computed traces (e.g., Smith & Serra 1987; Press *et al.* 1992).

2.2.4 Computational considerations

The main advantage of collapsing a three-dimensional problem to two dimensions is an order-of-magnitude gain in the speed of simulations. Our software is parallelized to optimize its performance on a Linux cluster. We use the implementation MPICH of the standard message passing interface on a 16-processor cluster. Software performance on parallel computers depends on the amount of communication between different processes needed during a simulation. If no communication were needed, the calculation time would decrease linearly as a function of the number of available processors. The more communication required, the slower the performance will get, and, above a certain number of processors, no further gain in speed will be possible.

Table 2.2a shows how the performance of our implementation scales with respect to the number of processors. It can be seen that if the latter is doubled, runtime decreases by a factor of ∼2. Above 8 processors, the gain in speed falls off. Notice that in principle we should expect the simulation time to increase by a factor 8 for a next finer grid, as there will be 4 times more grid cells due to the dyadic refinement, and the number of timesteps will double due to a halving of the spacestep. Table 2.2b shows the runtimes for single simulations conducted with different grid spacings employing 16 processors in parallel. A single simulation, running in parallel on clusters larger than ours, will nevertheless be punished by the need of data communication between the processes. Since one simulation can be completed within a minute on a single processor (for grid spacings around 70 km), a large cluster system has the obvious advantage that each processor can run a separate simulation.

A single simulation of surface wave propagation via the full numerical integration of the equation of motion in 3-D (e.g., spectral-element methods) would take minutes even on large cluster systems, and can be carried out in seconds by our approximate, 2-D membrane wave algorithm on a small cluster. While analytical methods like that of Spetzler *et al.* (2002) are only proved to perform well in a spherical-background-Earth scenario, we show below that ours, through an application of the adjoint method (Tarantola 1984), can provide a full kernel library in a heterogeneous reference model as well, in a reasonable amount of time.

2.3 Membrane-wave sensitivity functions

2.3.1 A “direct” approach

Let us introduce the single-scattering sensitivity function $K(\vartheta, \varphi)$ (e.g., Spetzler *et al.* 2002), relating a local relative perturbation in phase velocity $\delta c/c$ on the sphere’s surface

Table 2.2: Performance efficiency. Runtimes with (a) different numbers of processors and an average grid spacing of 70 km, (b) 16 processors*, different grid spacings.

(a)

number of processors	runtime $[s]$
1	60.9 s
2	31.8 s
4	15.9 s
8	8.5 s
16	5.5 s

(b)

grid spacing $[km]$	runtime $[s]$
278	0.1 s
139	0.7 s
70	5.5 s
35	42.0 s
17	340.3 s

* processor type: AMD Opteron 64-bit, 2 GHz clock speed

Ω to a relative phase anomaly $\delta\Phi/\Phi$, via the linear equation

$$\frac{\delta\Phi}{\Phi} = \int_\Omega K(\vartheta,\varphi)\frac{\delta c}{c}(\vartheta,\varphi)\,\mathrm{d}\Omega. \tag{2.14}$$

It is intended that $K(\vartheta,\varphi)$ depends on the source-station distance, or, in the case of a laterally heterogeneous Earth (membrane), on the locations of source and station.

For any given source-station combination, $K(\vartheta,\varphi)$ can be determined numerically, performing a set of simulations on a given background phase-velocity model $c(\vartheta,\varphi)$, with one small perturbation at a single cell centered at (ϑ_i,φ_i),

$$\frac{\delta c}{c} = f_i(\vartheta,\varphi) = \begin{cases} \gamma & \text{in the grid-cell centered at } (\vartheta_i,\varphi_i) \\ 0 & \text{everywhere else.} \end{cases} \tag{2.15}$$

Equation (2.14) then becomes

$$\frac{\delta\Phi_i}{\Phi} = \int_\Omega K(\vartheta_i,\varphi_i)\gamma\,\mathrm{d}\Omega = K(\vartheta_i,\varphi_i)\gamma A_i, \tag{2.16}$$

where A_i is the area of the ith cell. We denote $\delta\Phi_i$ the phaseshift associated with the perturbation (2.15), which we calculate by a membrane simulation and subsequent cross-correlation of the modeled phase with the unperturbed one. Then, from (2.16),

$$K(\vartheta_i, \varphi_i) = \frac{\delta\Phi_i}{\Phi A_i \gamma}, \tag{2.17}$$

and $K(\vartheta_i, \varphi_i)$ can be found from the numerically calculated $\delta\Phi_i$. In our calculations of $\delta\Phi_i$, we compute cross-correlation on the basis of Press *et al.*'s (1992) routine, but with quadratic subsample precision (Smith & Serra 1987).

Notice that numerical integration of eq. (2.3) on the membrane involves a simplified representation of the source in terms of initial displacement and source-time function (section 2.2.1). We must therefore neglect the effects on wave propagation of specific seismic source mechanisms (Zhou *et al.* 2004; Yoshizawa & Kennett 2005). This will be the subject of further investigations.

In principle, calculating $K(\vartheta_i, \varphi_i)$ for each cell i requires as many simulations as there are cells. This exercise then has to be repeated, in the case of a homogeneous reference Earth (constant $c(\vartheta, \varphi)$), for a dense set of epicentral distances spanning the range of true epicentral distances at which observations are available. In the case of a laterally heterogeneous reference Earth, it has to be repeated for each combination of source and station locations for which observations are available. The latter endeavour is too costly and we have discarded it; however, in the case of a constant reference phase velocity, it is feasible to calculate kernels via eq. (2.17).

Geometrical setup

We reduce the number of simulations needed to find $K(\vartheta, \varphi)$ in the "direct" approach as follows (Tong *et al.* 1998): after placing the source at, say, the North Pole, we perform one simulation for each scatterer location along one chosen meridian (Fig. 2.4). For each simulation, we save modeled traces at an array of receivers located along the parallels, spaced 1° in longitude and latitude from each other. If the background Earth model is homogeneous, what matters is not the absolute locations of scatterer and receiver, but their relative positions. From the set-up described above we therefore find the same traces that we would find considering one receiver at a time, and performing one simulation per possible scatterer location.

Figure 2.4: Set-up for the "direct" approach to computing sensitivity kernels (section 2.3.1), with one source (star) located at the North Pole, the scatterer position (circle) varying along a single meridian, and a set of receiver stations (triangles) located along parallels.

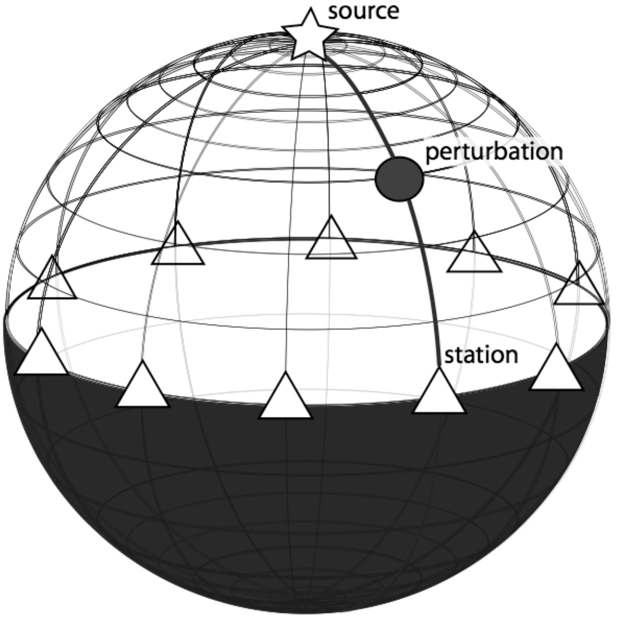

In practice, this results in reducing the number of required simulations from 64,442 to 181 (for the reference case of 1° × 1° sampling of $K(\vartheta,\varphi)$, and using 360 receivers simultaneously). Running our parallel algorithm on 16 processors, with a grid-spacing of about 70 km (level 6 hexagonal grid), we entirely determine $K(\vartheta,\varphi)$, for a given epicentral distance, in about 6 minutes. Without the simplification introduced here, the same computation would take approximately 3 days.

Nonlinearity

In principle, sensitivity functions derived as in section 2.3.1 should not depend on the value of the imposed phase-velocity perturbation γ. However, as γ grows, the problem eventually becomes nonlinear, and the linearized equation (2.14) ceases to be valid, together with the concept itself of sensitivity kernels. Testing the stability of our algorithm, we have found that, above a certain threshold ($\gamma \sim 2\%$), the mentioned nonlinearity comes into play and numerical kernels we find are slightly but visibly affected by changes in the value of γ.

Hung *et al.* (2001) found a similar effect from a set of 3-D spectral element simulations. In their figure 17 they plot traveltime anomaly found by cross-correlation (equivalent to our $\delta\Phi$) as a function of imposed heterogeneity (γ in section 2.3.1 here, ε in Hung *et al.*'s (2001) notation). While Born theory requires that a linear relationship exists between $\delta\Phi$ and γ, the corresponding curve obtained from numerical results is a straight line only for small values of γ. Hung *et al.* (2001, section 5.6) find an asymmetry in the dependence of $\delta\Phi$ on γ for positive vs. negative values of γ. They explain this result as a combination of wavefront healing and the "overhealing" effect of the cross-correlation technique. In our case there is not such a strong asymmetry between the effect of negative and positive anomalies.

2.3.2 The adjoint approach

Our "membrane" algorithm is efficient enough that, on a homogeneous reference Earth, $K(\vartheta, \varphi)$ can be computed by a large set of direct simulations. The number of simulations required to determine $K(\vartheta, \varphi)$, however, is much larger when the reference Earth is laterally heterogeneous, and the "direct" approach outlined above ceases to be practical. Tromp *et al.* (2005) give an overview of the application of back-propagation to the calculation of sensitivity functions, resulting in the "adjoint methods" introduced by Tarantola (1984) or Talagrand & Courtier (1987). In this approach, regardless of the complexity of the reference model, $K(\vartheta, \varphi)$ for a given source-receiver pair can be fully determined with two simulations only: one for the forward-propagating wavefield, from the source to the receiver; another for the back-propagating wavefield, from the receiver to the source. At each point (ϑ, φ), $K(\vartheta, \varphi)$ is found algebraically as a function of the forward- and back-propagating wavefields.

Next we provide a formulation of the adjoint method for the case of surface wave phase-anomaly observations, to be inverted tomographically in our spherical membrane approach. Part of our treatment is very similar to that of Yoshizawa & Kennett (2005, section 2), except that we prefer to work in the time domain; the rest follows Tromp *et al.* (2005, sections 2 and 4.1).

Writing displacement anomalies in terms of the Green's function

The time-domain version of eq. (2.3) is given by

$$\left[\frac{1}{c^2(\mathbf{x})}\partial_t^2 - \nabla_1^2\right] s(\mathbf{x},t) = f(\mathbf{x}_s,t), \tag{2.18}$$

with $\mathbf{x} = (\vartheta, \varphi)$ for brevity, $\mathbf{x}_s$ denoting the location of the source, and $f(\mathbf{x}_s,t)$ a forcing term representing the source. Let us symbolize c_0 and s_0, respectively, the values of phase velocity and of the solution to (2.18) associated with our reference Earth (membrane) model ($c_0(\mathbf{x})$ need not be uniform); then

$$\left[\frac{1}{c_0^2(\mathbf{x})}\partial_t^2 - \nabla_1^2\right] s_0(\mathbf{x},t) = f(\mathbf{x}_s,t). \tag{2.19}$$

After adding a term $\frac{1}{c_0^2(\mathbf{x})}\partial_t^2 s(\mathbf{x},t)$ to both sides of (2.18),

$$\left[\frac{1}{c_0^2(\mathbf{x})}\partial_t^2 - \nabla_1^2\right] s(\mathbf{x},t) = \frac{1}{c_0^2(\mathbf{x})}\left[1 - \frac{c_0^2(\mathbf{x})}{c^2(\mathbf{x})}\right]\partial_t^2 s(\mathbf{x},t) + f(\mathbf{x}_s,t). \tag{2.20}$$

Introducing

$$\delta c(\mathbf{x}) = c(\mathbf{x}) - c_0(\mathbf{x}), \tag{2.21}$$

we simplify the right hand side of (2.20) noting that

$$1 - \frac{c_0^2(\mathbf{x})}{c^2(\mathbf{x})} = \frac{2c(\mathbf{x})\delta c(\mathbf{x}) - [\delta c(\mathbf{x})]^2}{c^2(\mathbf{x})} \approx \frac{2\delta c(\mathbf{x})}{c(\mathbf{x})}, \tag{2.22}$$

after neglecting perturbations of second order in δc. Likewise, introducing $\delta s(\mathbf{x},t) = s(\mathbf{x},t) - s_0(\mathbf{x},t)$ and using the relation (2.19), we reduce (2.20) to

$$\left[\frac{1}{c_0^2(\mathbf{x})}\partial_t^2 - \nabla_1^2\right] \delta s(\mathbf{x},t) = \frac{2\delta c(\mathbf{x})}{c_0^2(\mathbf{x})c(\mathbf{x})}\partial_t^2 s(\mathbf{x},t). \tag{2.23}$$

Since we are neglecting terms of second order in δc, $s(\mathbf{x},t)$ can be replaced by $s_0(\mathbf{x},t)$ in the right hand side.

If we know the Green's function (e.g., Dahlen & Tromp 1998) for the membrane problem in question, defined as the solution $G(\mathbf{x},\mathbf{x}';t,t')$ to

$$\left[\frac{1}{c_0^2(\mathbf{x})}\partial_t^2-\nabla_1^2\right]G(\mathbf{x},\mathbf{x}';t,t')=-\delta(\mathbf{x}-\mathbf{x}')\delta(t-t'), \tag{2.24}$$

we can use it to find a solution to (2.23), i.e.,

$$\delta s(\mathbf{x},t)=\int_0^t\int_\Omega-\frac{2}{c_0^2\left(\mathbf{x}'\right)}G\left(\mathbf{x},\mathbf{x}';t-t'\right)\partial_t^2 s_0\left(\mathbf{x}',t'\right)\frac{\delta c\left(\mathbf{x}'\right)}{c\left(\mathbf{x}'\right)}\,\mathrm{d}\mathbf{x}'\mathrm{d}t'. \tag{2.25}$$

Notice that the procedure we have followed so far is analogous, for example, to those of Snieder & Nolet (1987), Dahlen *et al.* (2000), and Boschi (2006).

Writing travel-time (or phase) anomalies in terms of the Green's function

As in Dahlen *et al.* (2000), we assume that the phase anomaly between two seismograms can be defined as the value of phase-shift between the two, that maximizes their cross-correlation. In terms of travel time T, and relative perturbations in travel time $\frac{\delta T}{T_0}$ (which coincide with relative perturbations in phase), this implies

$$\frac{\delta T}{T_0}=\frac{1}{T_0}\frac{1}{N}\int_0^T w(t)\partial_t s(\mathbf{x}_r,t)\delta s(\mathbf{x}_r,t)\,\mathrm{d}t \tag{2.26}$$

(Tromp *et al.* 2005, eq. (41); Marquering *et al.* 1999), where T is the duration of the seismogram and N is a normalization factor given by

$$N=\int_0^T w(t)s(\mathbf{x}_r,t)\partial_t^2 s(\mathbf{x}_r,t)\,\mathrm{d}t, \tag{2.27}$$

where $w(t)$ denotes the cross-correlation window and $\mathbf{x}_r$ the location of the receiver. Note that N will be different for each source-station pair. Substituting (2.25) into (2.26),

$$\begin{aligned}\frac{\delta T}{T_0}= &\quad \tfrac{1}{T_0}\tfrac{1}{N}\textstyle\int_0^T w\left(t\right)\partial_t s\left(\mathbf{x}_r,t\right)\int_0^t\int_\Omega-\tfrac{2}{c_0^2(\mathbf{x}')}\\ &\times G\left(\mathbf{x}_r,\mathbf{x}';t-t'\right)\partial_t^2 s\left(\mathbf{x}',t'\right)\left(\tfrac{\delta c(\mathbf{x}')}{c(\mathbf{x}')}\right)d\mathbf{x}'\,\mathrm{d}t'\,\mathrm{d}t.\end{aligned} \tag{2.28}$$

Finding membrane sensitivity kernels in the adjoint approach

It is now convenient to make use of the equality (Tromp *et al.*, 2005)

$$\int_0^T h(t)\int_0^t g(t')\,\mathrm{d}t'\,\mathrm{d}t=\int_0^T g(t)\int_0^{T-t} h(T-t')\,\mathrm{d}t'\,\mathrm{d}t, \tag{2.29}$$

valid for any integrable functions $h(t)$, $g(t)$, to rewrite eq. (2.28) in the form

$$\begin{aligned}\frac{\delta T}{T_0}= &\int_\Omega \tfrac{1}{T_0}\tfrac{1}{N}\int_0^T -\tfrac{2}{c_0^2(\mathbf{x}')}\partial_t^2 s\left(\mathbf{x}',t\right)\tfrac{\delta c(\mathbf{x}')}{c(\mathbf{x}')}\int_0^{T-t} G\left(\mathbf{x}',\mathbf{x}_r,T-t-t'\right)\\ &\times w\left(T-t'\right)\partial_t s\left(\mathbf{x}_r,T-t'\right)\,\mathrm{d}t'\,\mathrm{d}t\,d\mathbf{x}'.\end{aligned} \tag{2.30}$$

If one then denotes

$$\bar{s}^\dagger(\mathbf{x}',\mathbf{x}_r,T-t)=\frac{1}{N}\int_0^{T-t} G(\mathbf{x}',\mathbf{x}_r,T-t-t')w(T-t')\partial_t s(\mathbf{x}_r,T-t')\,\mathrm{d}t', \tag{2.31}$$

eq. (2.30) is reduced to

$$\frac{\delta T}{T_0}=-\int_\Omega \frac{1}{T_0}\int_0^T \frac{2}{c_0^2(\mathbf{x}')}\partial_t^2 s(\mathbf{x}',t)\frac{\delta c(\mathbf{x}')}{c(\mathbf{x}')}\bar{s}^\dagger(\mathbf{x}',\mathbf{x}_r,T-t)\,\mathrm{d}t\,d\mathbf{x}'. \tag{2.32}$$

From a comparison of (2.32) with (2.14), we infer

$$K(\mathbf{x},\mathbf{x}_r)=-\frac{2}{T_0\,c_0^2(\mathbf{x})}\int_0^T \bar{s}^\dagger(\mathbf{x},\mathbf{x}_r,T-t)\partial_t^2 s(\mathbf{x},t)\,\mathrm{d}t. \tag{2.33}$$

On the basis of eq. (2.31) and of the definition of Green's function, $\bar{s}^\dagger$ coincides with the wavefield originated on the membrane by a source

$$\bar{f}^\dagger(\mathbf{x},t)=\frac{1}{N}w(T-t)\partial_t s(\mathbf{x}_r,T-t)\delta(\mathbf{x}-\mathbf{x}_r). \tag{2.34}$$

In analogy with Tromp *et al.* (2005), we call $\bar{s}^\dagger$ and $\bar{f}^\dagger$ "adjoint field" and "adjoint source", respectively. Notice that the adjoint source is by definition located at the receiver $\mathbf{x}_r$, and that it contains the time-reversed velocity seismogram from the forward synthetic wavefield.

The practical relevance of equations (2.31) through (2.34) becomes apparent when one realizes that (2.31) can be implemented numerically, feeding $\bar{f}^\dagger$ as defined by (2.34) to a numerical algorithm like our finite-difference membrane scheme, reversed in time. One forward-propagating simulation must be conducted previously, so that $s(\mathbf{x}_r, t)$ be known (its first and second derivatives with respect to time can be determined numerically): the adjoint source is then entirely defined, and one more run of the finite-difference algorithm is sufficient to determine $K(\mathbf{x}, \mathbf{x}_r)$, for all values of $\mathbf{x}$. Whatever the source-station geometry, and the complexity of the starting model $c_0(\mathbf{x})$, $K(\mathbf{x}, \mathbf{x}_r)$ is known after two simulations only.

2.3.3 Some practical considerations

Discretization of the adjoint source

Like the initial displacement (2.5), (2.6), the adjoint source must be discretized on our membrane grid; let us introduce a discretized version $\bar{f}^\dagger_m$ (subscript m for membrane) of $\bar{f}^\dagger$ as defined by equation (2.34),

$$\bar{f}^\dagger_m(\mathbf{x}, t) = \frac{1}{N} w(T-t)\partial_t s(\mathbf{x}_r, T-t) h(\mathbf{x}, \mathbf{x}_r), \tag{2.35}$$

with

$$h(\mathbf{x}, \mathbf{x}_r) = \begin{cases} 1 & \text{when } \mathbf{x} \text{ is in the same grid-cell as } \mathbf{x}_r \\ 0 & \text{elsewhere.} \end{cases} \tag{2.36}$$

Let us then denote $\bar{s}^\dagger_m$ the adjoint field generated by $\bar{f}^\dagger_m$ on the discretized membrane. Then, by definition of Green's function,

$$\begin{aligned}
\bar{s}^\dagger_m(\mathbf{x}, \mathbf{x}_r, T-t) &= \int_0^{T-t} \int_\Omega G(\mathbf{x}, \tilde{\mathbf{x}}, T-t-t') \bar{f}^\dagger_m(\tilde{\mathbf{x}}, t') d\tilde{\mathbf{x}}\, \mathrm{d}t' && (2.37) \\
&= \tfrac{1}{N} \int_0^{T-t} \int_{\text{cell-}\mathbf{x}_r} G(\mathbf{x}, \tilde{\mathbf{x}}, T-t-t') w(T-t') \\
&\qquad \times \partial_t s(\mathbf{x}_r, T-t') d\tilde{\mathbf{x}}\, \mathrm{d}t' && (2.38) \\
&= \tfrac{1}{N} \int_0^{T-t} G(\mathbf{x}, \mathbf{x}_r, T-t-t') w(T-t') \partial_t s(\mathbf{x}_r, T-t')\, \mathrm{d}t' \\
&\qquad \times \int_{\text{cell-}\mathbf{x}_r} d\tilde{\mathbf{x}} && (2.39) \\
&= \bar{s}^\dagger(\mathbf{x}, \mathbf{x}_r, T-t) A_r, && (2.40)
\end{aligned}$$

with cell-$\mathbf{x}_r$ denoting the surface of the grid-cell containing $\mathbf{x}_r$, and A_r its area.

As in practical implementations we shall obtain the "discretized" adjoint wavefield $\bar{s}^\dagger_m$, it makes sense to use (2.40) and replace $\bar{s}^\dagger$ with $\bar{s}^\dagger_m / A_r$ in (2.33), to find an expression for the discrete version K_m of sensitivity kernels

$$K_m(\mathbf{x},\mathbf{x}_r) = -\frac{2}{A_r\, T_0\, c_0^2(\mathbf{x})} \int_0^T \bar{s}_m^\dagger(\mathbf{x},\mathbf{x}_r,T-t)\partial_t^2 s(\mathbf{x},t)\ \mathrm{d}t\,. \tag{2.41}$$

Waveform filtering

While we are interested in the propagation of one mode (one frequency of the dispersive surface wave packet) at a time, our membrane analogue is excited over a range of frequencies, depending on the initial conditions (2.5) and (2.6). To isolate the mode of interest, we bandpass-filter the solution using as center frequency the frequency of the mode of interest, and a half-bandwidth of 2.5 mHz. Spetzler *et al.* (2002) average their sensitivity kernels over the same bandwidth, to account for the fact that single-frequency phase-velocity measurements are not possible, owing to the finite sampling of seismograms and to the finite parameterization of the dispersion curve in the measurement process. The selected value for bandwidth also coincides with the spacing between splines parameterizing the measured dispersion curves in Ekström *et al.* (1997, figure 1), which could be taken as a rough estimate of the accuracy of said dispersion curves (Boschi 2006).

As noted in section 2.2.1, each membrane simulation provides the surface wave potential s associated with one specific surface wave mode. Strictly speaking, only the component of s at the frequency of the mode of interest is then physically meaningful. The relatively large bandwidth of our bandpass filter leads, however, to an effect similar to that found analytically by Spetzler *et al.* (2002), reducing the amplitude of kernels' sidelobes. Filtering can be equivalently applied to the scalar potential s found by numerical integration on the membrane, or to the initial conditions (2.5) and (2.6). We have experimented with both approaches, obtaining practically coincident results. The latter option is naturally more efficient.

2.4 Results

The discussion that follows is limited to phase-velocity kernels of intermediate-to-long period Love waves; we expect that a similar procedure is valid, and the same qualitative results hold for the case of Rayleigh waves.

2.4.1 Sensitivity kernels for a homogeneous (spherical-Earth) starting model

Comparing analytically and numerically determined sensitivity kernels

In Fig. 2.5 we compare a sensitivity kernel calculated numerically in the membrane approach, with one calculated analytically from Boschi's (2006) implementation of Spetzler *et al.*'s (2002) eq. (16), based on Snieder & Nolet's (1987) single-scattering approach. Source (0°N, 0°E) and receiver (0°N, 90°E) locations, and surface wave period (150 s) are the same in both cases. The background value for phase velocity coincides with the Love-wave, PREM-based (Dziewonski & Anderson 1981) value. Numerical kernel values are calculated on the cell midpoints (as described in section 2.2.3) of our grid and then interpolated for plotting with 1° spacing in both latitude and longitude. Analytical values are likewise averaged over each cell and interpolated for plotting.

Figure 2.5: Sensitivity kernel for Love waves at 150 s, spherical Earth model (homogeneous phase velocity), source at (0°N, 0°E) and receiver at (0°N, 90°E), (a) calculated numerically in the "direct" approach; (b) calculated implementing the analytical formula of Spetzler *et al.* (2002).

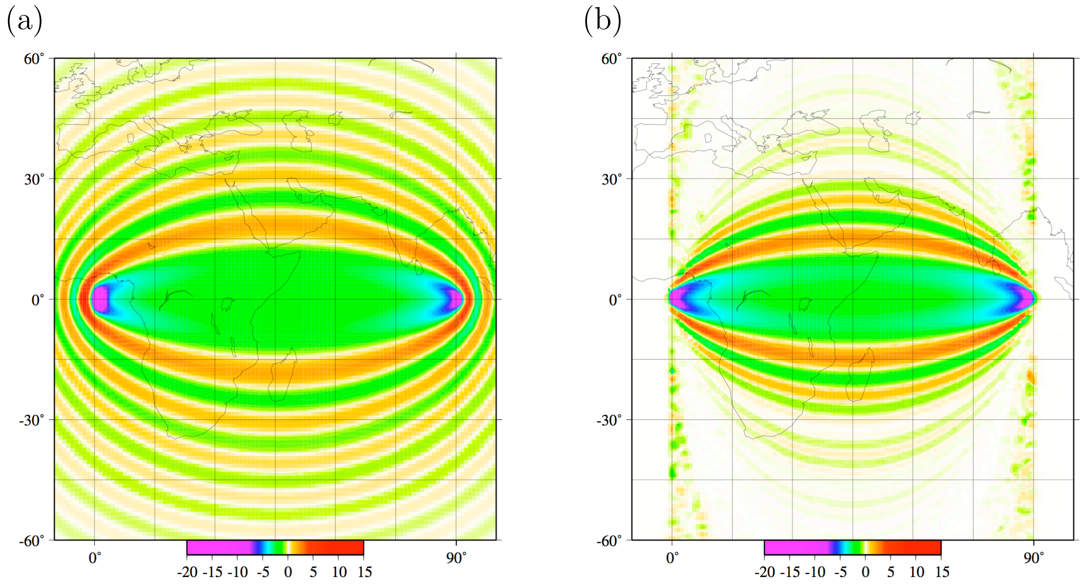

As pointed out by Favier *et al.* (2004) and Boschi (2006), Spetzler *et al.*'s (2002) and other Born-theory formulations (e.g., Zhou *et al.* 2004; Yoshizawa & Kennett

2005) involve a far-field approximation of the unperturbed solution; sensitivity kernels found in this approach are necessarily singular at source and receiver. This explains the unphysical behavior of analytical kernels evident from Fig. 2.5b at longitudes around 0° and 90°. Furthermore, analytical kernels in Fig. 2.5 are zero at longitudes larger than the epicentral distance, and at any location at a negative azimuth from the source; this is an effect of simplifications in Spetzler *et al.*'s (2002) procedure — a fictitious feature that we do not find in expressions for analytical kernels later derived by Zhou *et al.* (2004) and Yoshizawa & Kennett (2005).

Comparing sensitivity kernels found via the "direct" vs. adjoint approach

In Fig. 2.6 a comparison between cross-sections of numerical kernels for Love waves at 150 s period is shown. Numerical kernel values are either calculated with the "direct" approach or the adjoint method, both described in section 2.3. We employ in both cases the same numerical mesh and homogeneous background model. For the "direct" approach, we apply a relative perturbation γ of -0.2%. Source and station are at a fixed epicentral distance and placed as in Fig. 2.5. Cross-sections of both kernels are taken at distinct longitudes. The "direct" calculation takes about six minutes on 16 processors to produce a complete numerical-direct kernel over the whole sphere (using the reduction from section 2.3.1). With the adjoint method, the complete numerical-adjoint kernel is obtained in about two minutes on a single processor. As can be seen, the two kernels are practically identical. This is an important demonstration of the internal consistency of our approaches.

In Fig. 2.7 we explore how membrane sensitivity kernels vary as a function of source-station distance; the area of all Fresnel zones expands as already described by, e.g., Spetzler *et al.* (2002, figure 2b). For stations located closer to the epicenter, overall higher sensitivity is found.

Fig. 2.8 shows the dependence of sensitivity kernels on wave period at a fixed epicentral distance. The central lobes of the kernels increase with increasing period. This is qualitatively confirmed by analytical results (e.g., Spetzler *et al.* 2002, figure 2a).

Due to the memory-intensive storage of the numerical grid, our current computer hardware prevents us from running simulations with periods <75 s. The numerical scheme we apply requires about 10 nodes per wavelength for an accurate representation of the wave phenomena on the membrane (see section 2.2.3); thus, for shorter periods

Figure 2.6: Cross-sections of sensitivity kernels for Love waves at 150 s calculated via the “direct” approach (dashed lines) and adjoint method (solid lines), with source at (0°N, 0°E) and receiver at (0°N, 90°E). Sensitivity values are plotted as a function of latitude only, along three chosen meridians, namely (a) 10°, (b) 20° and (c) 45°.

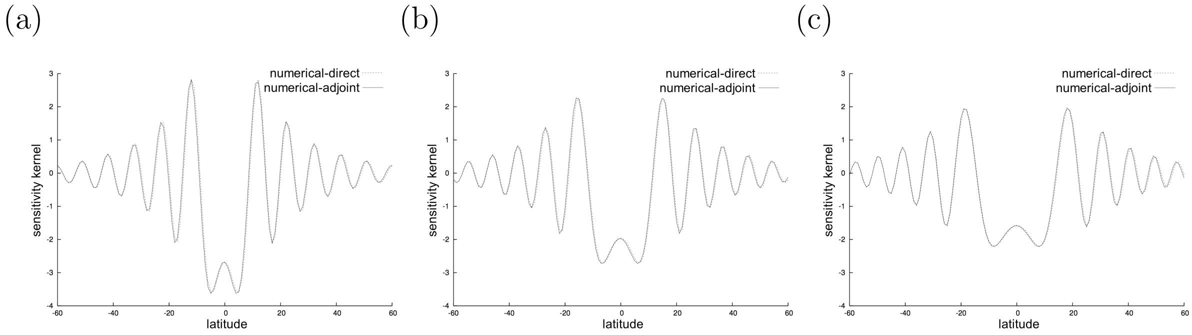

we would need a grid spacing with less than 17 km distance which leads to more than two million grid cells. With 2 GB RAM memory per cluster node we are bound by this limitation. A work-around could consist of accessing the mesh points through I/O with a corresponding file storage. This would considerably slow down the computation process.

2.4.2 Sensitivity kernels for a laterally heterogeneous starting model

Our method naturally allows us to calculate phase-velocity sensitivity kernels associated with a laterally heterogeneous starting model (background Earth). Computing a single numerical kernel in the adjoint approach takes exactly the same time (2 minutes on one of our processors) regardless whether the background Earth is homogeneous or heterogeneous. In the limit of our smooth-Earth assumption, we explore the impact of background heterogeneities on the properties of surface wave kernels.

Fig. 2.9 shows a starting model for 150 s Love wave phase velocity. We derived it based on local normal-mode theory (Boschi & Ekström 2002), from an Earth model consisting of the 3-D crustal model Crust-2.0 (Bassin *et al.* 2000), overlying a 1-D, radially isotropic profile of the mantle as in Boschi *et al.* (2004). The map in Fig. 2.9 represents a rough guess of crustal effects on long-period Love wave propagation, and is independent of

Figure 2.7: Numerical-adjoint kernels derived for 150 s Love waves in a homogeneous starting model. The source is located at (0°N, 0°E), the receiver at 0°N and (a) 60°E, (b) 90°E and (c) 120°E.

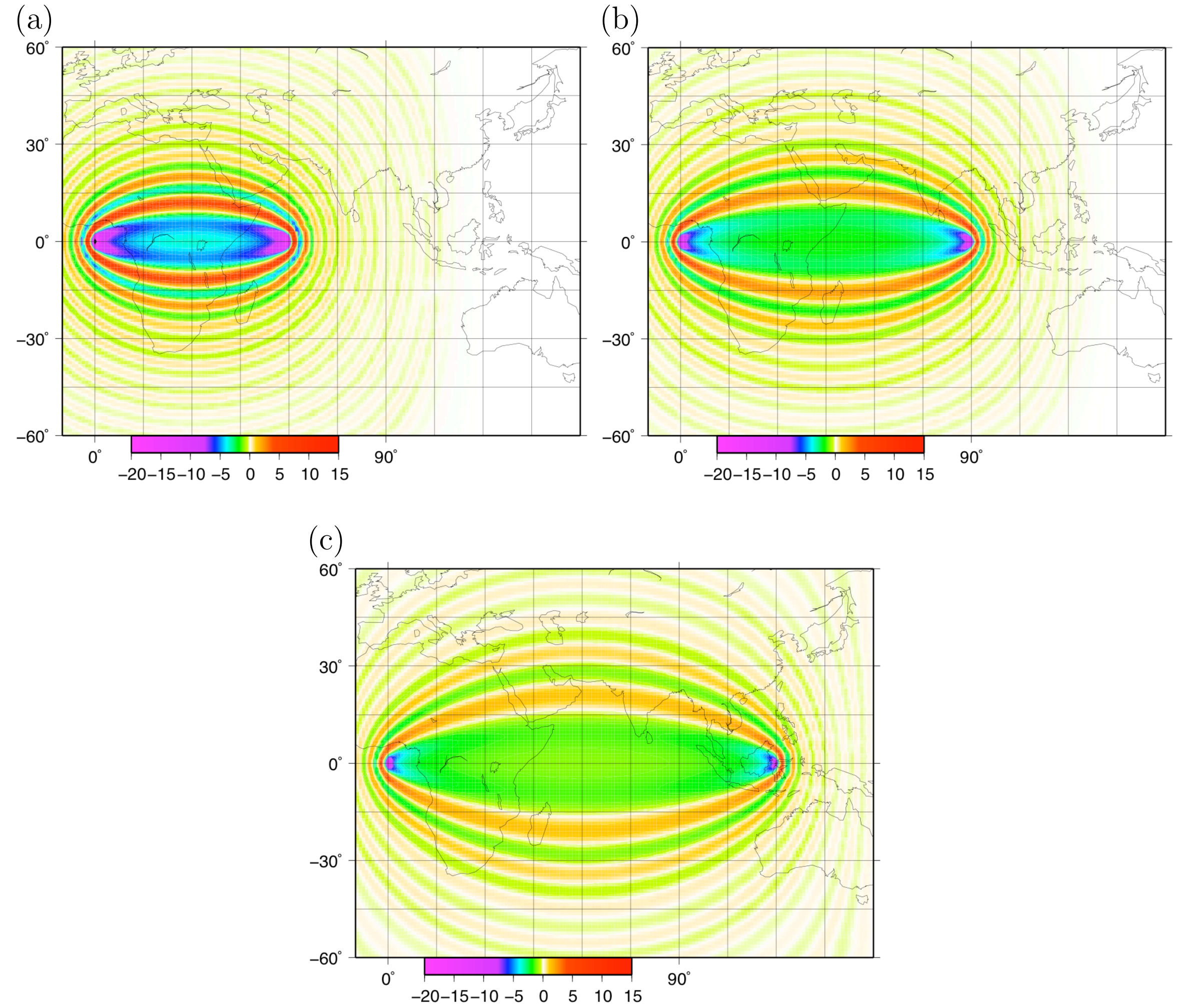
(a)
60°
30°
0°
−30°
−60°
0°
90°
−20 −15 −10 −5 0 5 10 15
(b)
60°
30°
0°
−30°
−60°
0°
90°
−20 −15 −10 −5 0 5 10 15
(c)
60°
30°
0°
−30°
−60°
0°
90°
−20 −15 −10 −5 0 5 10 15

Figure 2.8: Numerical-adjoint kernels for Love waves at (a) 150 s, (b) 100 s and (c) 75 s periods, in a homogeneous starting model. The source is located at (0°N, 0°E), the receiver at (0°N, 90°E).

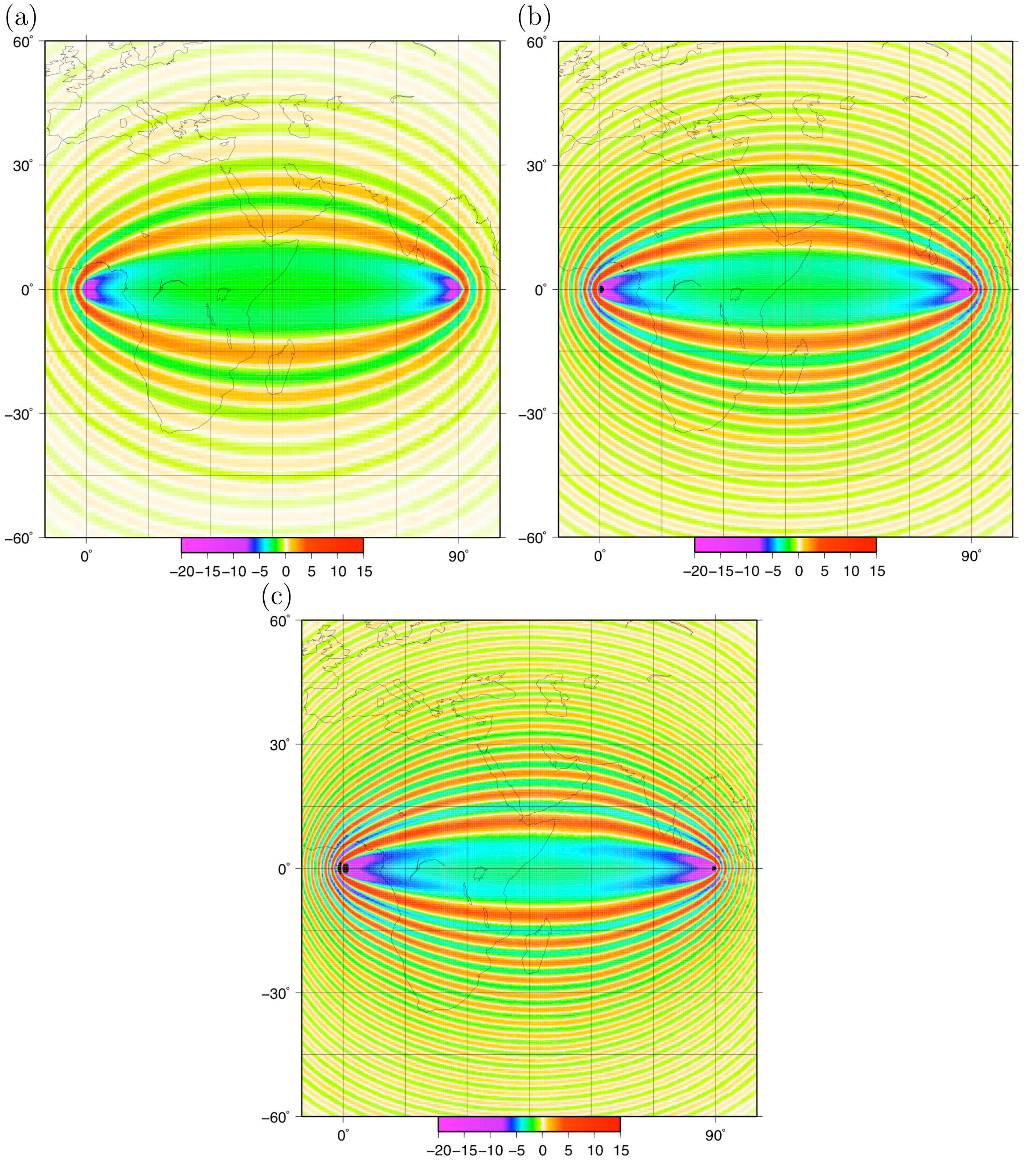
(a)
60°
30°
0°
−30°
−60°
0°
90°
−20 −15 −10 −5 0 5 10 15
(b)
60°
30°
0°
−30°
−60°
0°
90°
−20 −15 −10 −5 0 5 10 15
(c)
60°
30°
0°
−30°
−60°
0°
90°
−20 −15 −10 −5 0 5 10 15

surface wave observations like those we will invert in the following. In order to expect significant differences, it has been filtered to harmonic degrees ≤ 40 (thus allowing spatial wavelengths close to the ones of Love waves at 150 s). Our implementation is only physically meaningful in the smooth-Earth approximation (section 2.2.1); the algorithm remains stable in the presence of strong gradients, but the formulation of the membrane approach depends upon lateral smoothness.

Figure 2.9: 150 s Love-wave phase-velocity map based on Crust-2.0 (Bassin *et al.* 2000) and an isotropic upper-mantle model. The phase-velocity heterogeneities are represented by a spherical harmonic expansion with degrees $l \leq 40$, resulting in a low-pass filtered phase-velocity map (the membrane analogue has physical meaning in a smooth Earth regime). Phase-velocity values are projected onto our hexagonal grid, and plotted as colored dots at the centre of each of its cells (122,882 total cells). Source and receiver are denoted by the star and triangle connected by the source-receiver great circle, which crosses the Tibet anomaly. Phase-velocity anomalies are given in percent with respect to PREM.

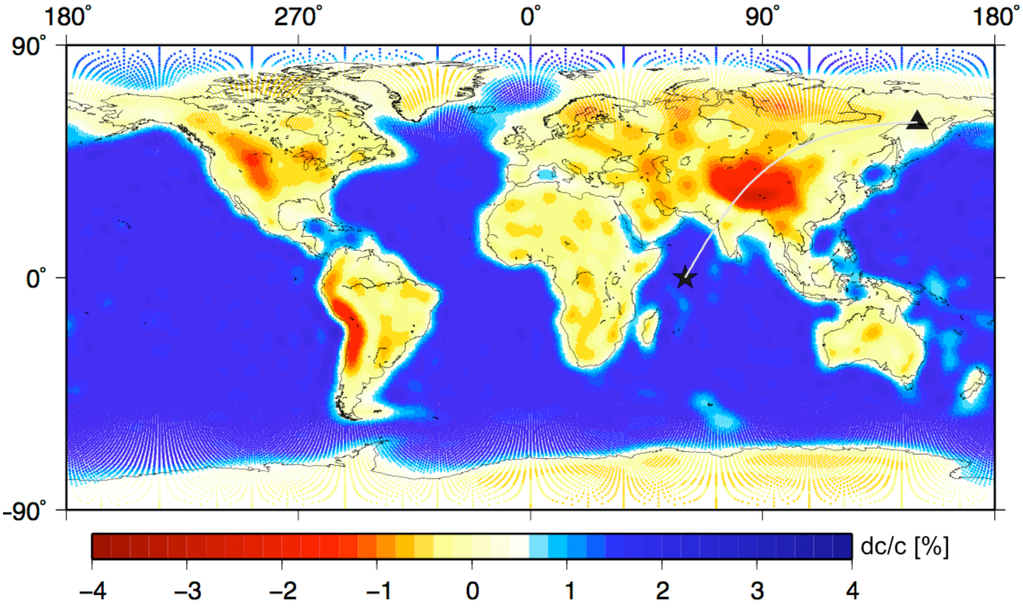

We show in Fig. 2.10a a 150 s Love wave kernel based on the model of Fig. 2.9, and a source-station geometry that should maximize the effect of the starting model's strongest phase-velocity heterogeneity, located in the Himalaya region with approximately −3% relative phase-velocity perturbation. The homogeneous-Earth kernel associated with the same source and receiver is shown in Fig. 2.10b, and the difference between the two in Fig. 2.10c. The two kernels coincide in the first Fresnel-zone (main lobe), while significant differences are apparent in the sidelobes. Strongest differences are found to the southeast of the great circle path, corresponding to higher gradients in phase velocity (transition from a continental to an oceanic region).

Figure 2.10: Sensitivity kernels derived with the adjoint method for 150 s Love waves in (a) homogeneous and (b) heterogeneous (Fig. 2.9) starting phase-velocity models. (c) Difference between (a) and (b).

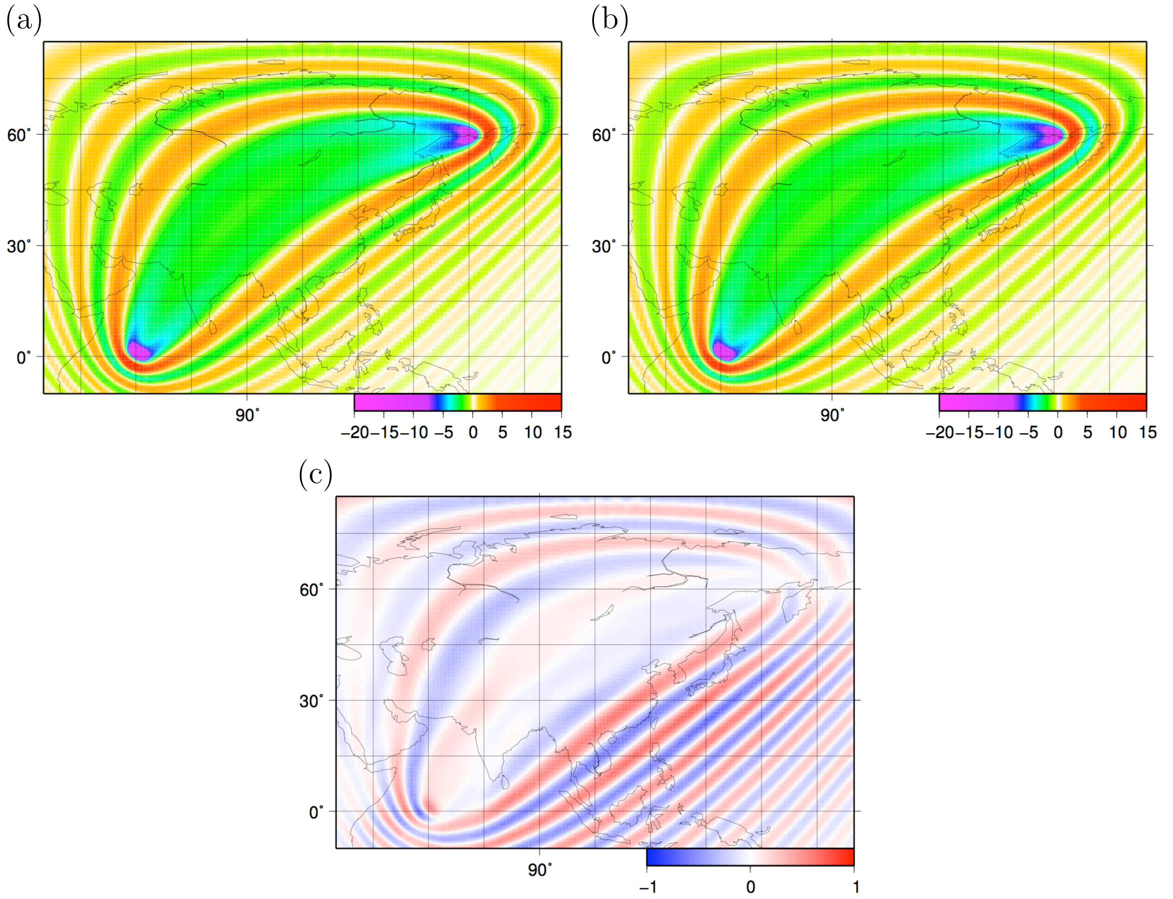

2.4.3 A test of the first-order scattering approximation

Born theory is a single-scattering theory, that is, it neglects the interaction of scattered wavefields with other heterogeneities. In practice, the linearized, Born-theoretical eq.

(2.14) implies that the effect of multiple heterogeneities be equal to the sum of the independently calculated effects of each heterogeneity. In forward calculations made on a smooth Earth model, our numerical algorithm naturally accounts for multiple scattering. Hence, while we do not attempt to formulate an inverse problem accounting for multiple scattering, we can perform a set of forward calculations to evaluate its relevance, and the associated inaccuracy of the linearized Born approximation.

Let us denote $\delta\Phi_{jk}$, the phase anomaly at the receiver due to the presence of two scatterers centered at (ϑ_j, φ_j) and (ϑ_k, φ_k) (i.e., extending over the whole cell of our hexagonal grid, centered at ϑ_j, φ_j or ϑ_k, φ_k), in an otherwise homogeneous background model. We compute this quantity in two ways: (i) by cross-correlation between the *numerical* solution found propagating membrane waves in the presence of two scatterers, and the one found on a homogeneous membrane; (ii) making use of previously calculated kernels $K(\vartheta, \varphi)$ to implement

$$\delta\Phi_{jk} = K(\vartheta_j, \varphi_j)\Phi\gamma A_j + K(\vartheta_k, \varphi_k)\Phi\gamma A_k, \tag{2.42}$$

based upon equation (2.14), where Φ is the homogeneous reference phase, A_j, A_k are the areas of the cells to which (ϑ_j, φ_j) and (ϑ_k, φ_k) respectively belong, γ is the phase-velocity perturbation, which for simplicity we choose to have the same value at both scatterers.

In the approach (i), multiple scattering is implicitly accounted for; in the approach (ii) it is neglected. The linearized Born approximation would suggest that both values of $\delta\Phi_{jk}$ are identical; differences between the resulting phase anomalies are the effect of multiple scattering. We perform a number of simulations with: source and receiver located at $(0°, 0°)$ and $(0°, 90°)$, respectively; one scatterer located at 45° longitude, and at latitudes varying between $-60°$ and $60°$; a second scatterer at the same latitude, and at a longitudinal distance of $+3°$, $+6°$ or $+9°$ to the first. For each considered couple of scatterers, we find phase anomaly both by "direct" numerical calculation (approach (i)) and by eq. (2.42) (approach (ii)); we plot in Fig. 2.11 the difference between the resulting values of $\delta\Phi$ as a function of scatterer-latitude.

As a general rule, we find that the effects of multiple scattering on seismic phase are small and the linearization in eq. (2.14) is valid. The largest discrepancy in $\delta\Phi$ amounts to $\sim$0.15% of the maximum $\delta\Phi$ predicted by eq. (2.42) and corresponds to the smallest distance (3°) between the two scatterers. These values are so small that the

Figure 2.11: Effects of multiple scattering. We use the membrane-wave method to calculate the phase anomaly $\delta\Phi_i^{\mathrm{num}}$ resulting from two scatterers, located at the same latitude and longitudinal distances 3°, 6° and 9°, and source and receiver at (0°N, 0°E) and (0°N, 90°E), respectively. After each simulation, we subtract $\delta\Phi_i^{\mathrm{num}}$ from the phase anomaly $\delta\Phi_i^{\mathrm{Born}}$ by simple Born theory (no multiple scattering, but the sum of the individual effects of each scatterer) and normalize the result to the maximum value of $\delta\Phi_i^{\mathrm{Born}}$ from all our multiple-scattering simulations. The resulting quantity $(\delta\Phi_i^{\mathrm{Born}} - \delta\Phi_i^{\mathrm{num}})/\max\{\delta\Phi_i^{\mathrm{Born}}\}$ is plotted in percent vs. scatterer latitude, with a separate curve for each value of longitudinal distance between scatterers (3°: solid line, 6°: long-dashed line, 9°: short-dashed line).

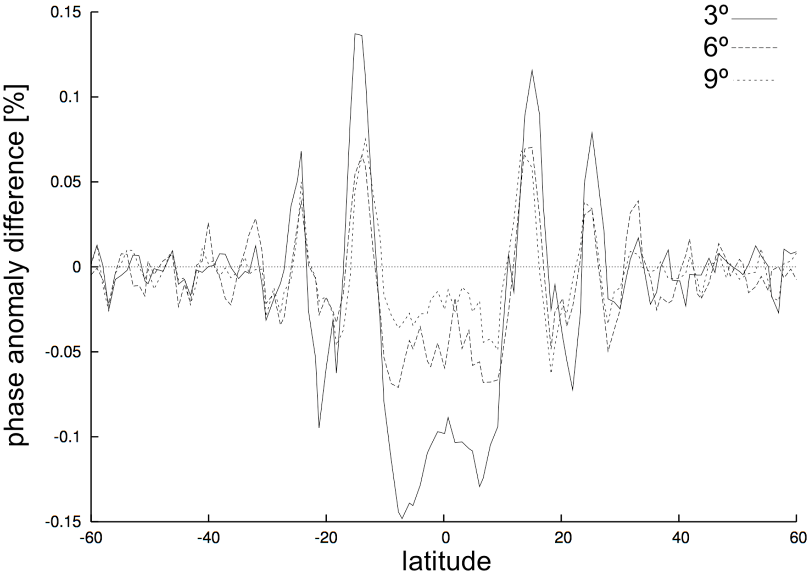

shape of the curves is significantly affected by the irregularity of the grid: gridpoints do not precisely align along parallels, but can be shifted up to ±0.5° in our mesh and the curves in Fig. 2.11 are jagged as a result. Multiple scattering becomes even less relevant for larger inter-scatterer distances (6° and 9° in our experiment). The latter result is to be expected, as the energy of the scattered wavefield at a given point decreases with increasing distance from the scatterer, by simple geometrical spreading. We infer that in a smooth-Earth regime the Born linearization is valid in the tomographic determination of phase-velocity anomalies. It would become less reliable at longer times/higher orbits.

2.4.4 Application to fundamental-mode surface wave tomography

The inverse problem of identifying a phase-velocity map from dispersion measurements compiled from a large set of source-receiver pairs is typically reduced to solving a linear system

$$\mathbf{A} \cdot \mathbf{x} = \mathbf{d} \tag{2.43}$$

(e.g., Boschi 2001), where the entries of **x** are the unknown coefficients of the phase-velocity map to be determined and those of **d** the measured relative phase anomalies $\delta\Phi/\Phi$. As a result of eq. (2.14), and employing a pixel parameterization (Boschi 2006),

$$A_{ij} = \int_{j^{\mathrm{th}}\,\mathrm{pixel}} K_{i^{\mathrm{th}}\,\mathrm{datum}}(\omega, \vartheta, \varphi)\,\mathrm{d}\Omega. \tag{2.44}$$

We invert the database of Ekström *et al.* (1997), updated as described by Boschi & Ekström (2002), implementing (2.44) and least-squares solving (2.43) with the algorithm of Boschi (2006), but calculating $K(\omega, \vartheta, \varphi)$ in different ways and different starting models, as described below. Our phase-velocity maps are linear combinations of equal-area pixel functions as in Boschi *et al.* (2006). The coverage (see Fig. 2.12 for 150 s Love-wave observations) and resolving power of the Harvard dispersion database have been evaluated in earlier publications (e.g., Ekström *et al.* 1997; Carannante & Boschi 2005).

Tomography with a homogeneous starting model

We follow the procedure described in sections 2.3.2 and 2.3.3 to calculate sensitivity kernels $K(\omega, \vartheta, \varphi)$ defined by eq. (2.14) (strictly speaking, what we find and use is their "discretized version" $K_m(\omega, \vartheta, \varphi)$ defined by (2.41)). So long as the starting model is homogeneous, the function $K(\omega, \vartheta, \varphi)$ changes if the source-receiver *distance* changes, but is not affected by changes in the locations of source and receiver: following Boschi (2006), we find $K(\omega, \vartheta, \varphi)$ at a discrete set of epicentral distances ranging from 20° to 179°, with 1° increments. We later spline-interpolate (Press *et al.* 1992) calculated $K(\omega, \vartheta, \varphi)$'s to find $K(\omega, \vartheta, \varphi)$ for any epicentral distance (Boschi 2006). In analogy with Spetzler *et al.* (2002) or Boschi (2006), we neglect source-mechanism variations for different events in the database, and use the source term (2.5), (2.6).

After implementing eq. (2.44) for the entire database at a chosen surface wave mode,

Figure 2.12: Ray-theoretical hitcount map (number of rays crossing each pixel) from the Harvard database, 150 s Love wave observations only. The equal-area pixel parameterization (3° × 3° at the equator) is the same used in our inversions.

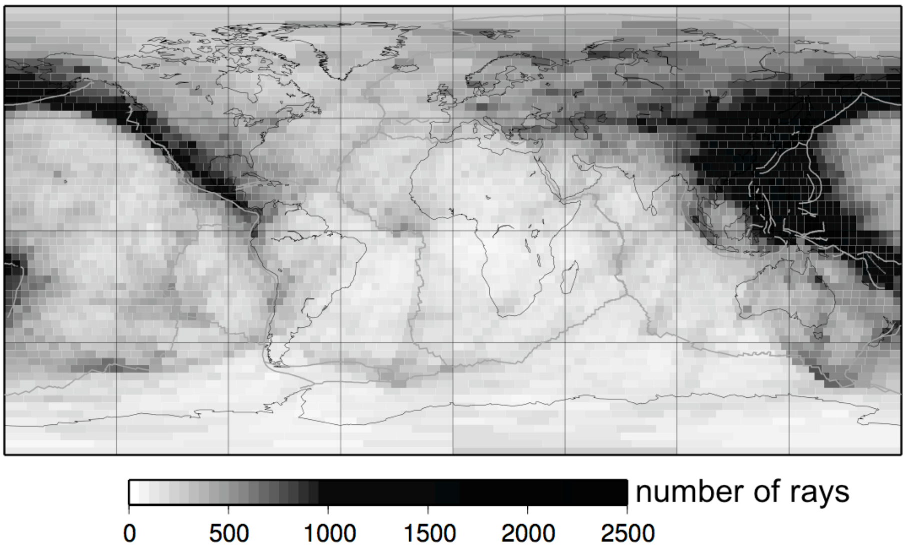

Figure 2.13: Trade-off analysis for the phase-velocity inversions of section 2.4.4 (homogeneous starting model). (a) L-curves for solutions derived from ray theory (dotted line, triangles), analytical Born theory (dashed line, pluses), and numerical-adjoint kernels (solid line, squares). (b) Curvature of the curves shown in (a). Image roughness is defined and normalized as in Boschi (2006).

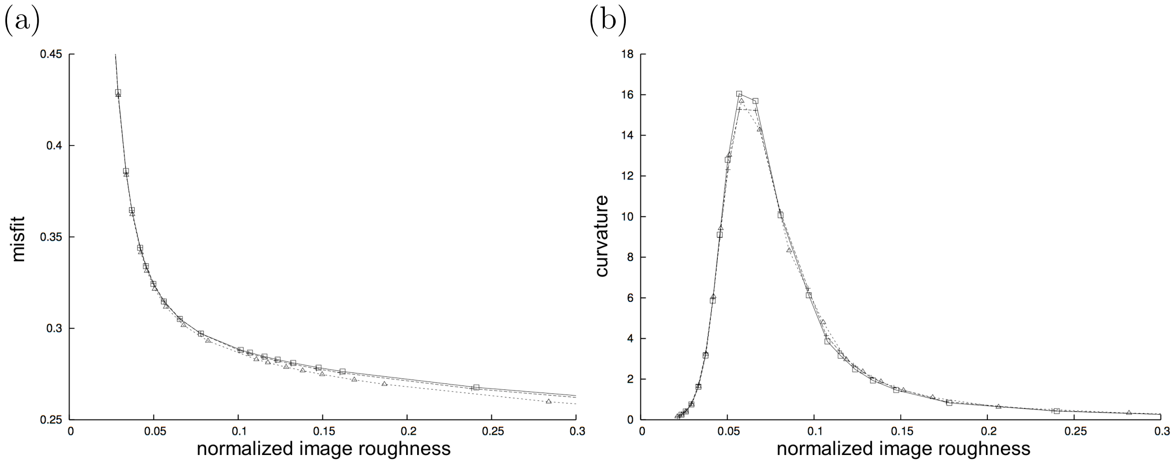

Figure 2.14: Phase-velocity maps from the inversions of section 2.4.4 (homogeneous starting model). We compare solutions found from (a) ray theory, (b) analytical Born theory, (c) numerical-adjoint kernels. Phase anomalies are in percent with respect to the value predicted by PREM.

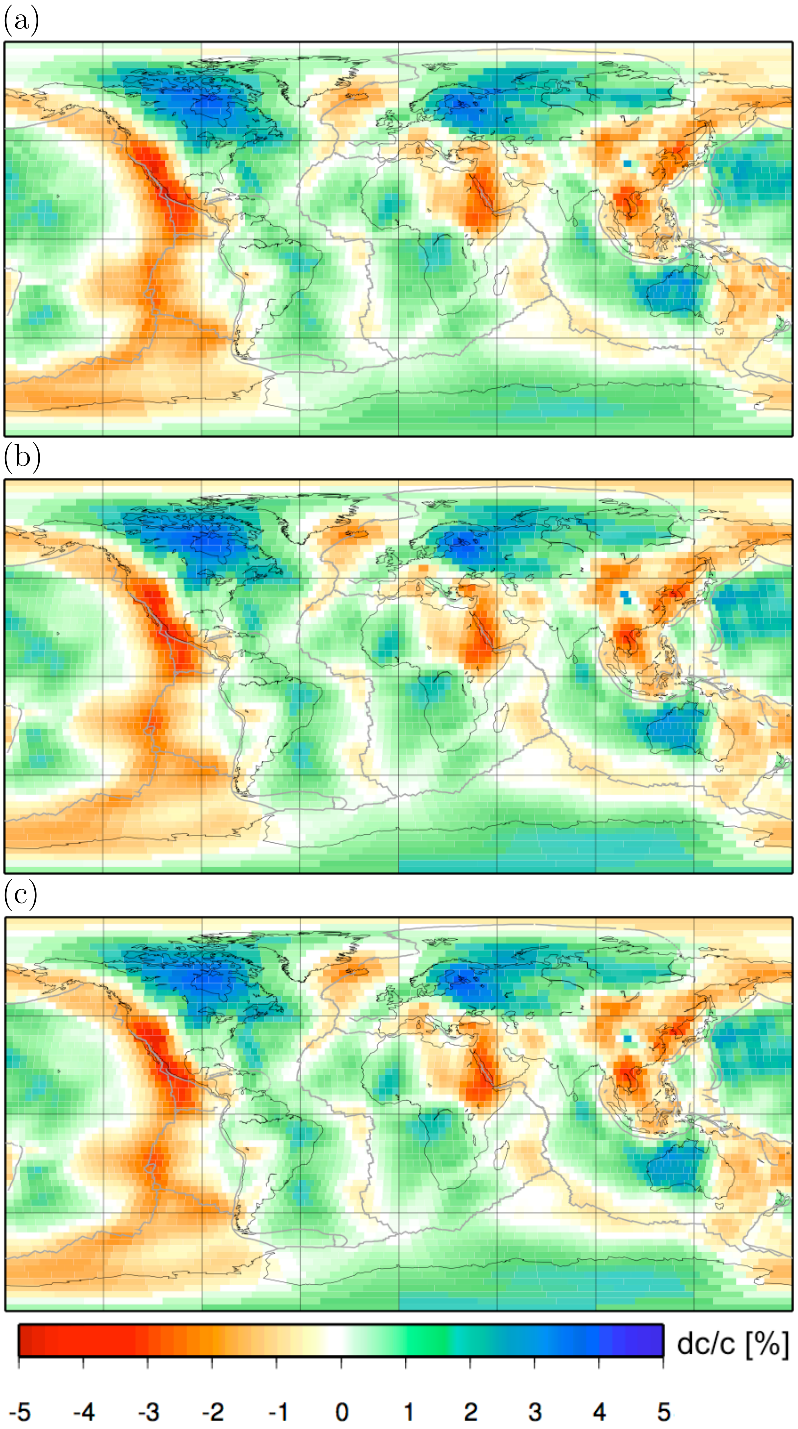

we least-squares invert (2.43) a number of times, varying the value of the roughness-damping parameter (Boschi 2006; Boschi *et al.* 2006); no other regularization constraint is applied. The resulting L-curve, or plot of misfit vs. normalized roughness of the solution, as defined by Boschi (2006), is shown in Fig. 2.13a. While we experimented with a variety of surface wave modes and tomographic parameterization, we shall limit our discussion to 150 s Love wave data inverted on a grid of equal area pixels with surface extent 3° × 3° at the equator.

We repeat this exercise, employing alternatively ray-theoretical sensitivity kernels, and analytical Born-theoretical ones based on Spetzler *et al.* (2002). We find that the L-curves resulting from the three approaches are qualitatively similar, as also noted by Boschi (2006). We identify from Fig. 2.13b solutions corresponding to equal curvature of the associated L-curves, and roughness comparable to that of, e.g., Ekström *et al.* (1997). Associated phase-velocity maps are shown in Fig. 2.14. The results of the three approaches are remarkably similar; the only discrepancies worth mentioning are perhaps two fast anomalies of small lateral extent, in the sourtheastern part of the Chinese Gansu province and in the Andes, present in the analytical-Born-theory solution, but not in the other two.

The most time-consuming part of our experiment was the calculation of sensitivity kernels at the mentioned set of 160 epicentral distances, for one surface wave mode (150 s Love waves). Applying the adjoint method on one processor, this would last about 5 hours. Computing A_{ij} for $16,624$ observations of $\delta\Phi/\Phi$ takes another 5 hours. Finally, least-squares solving the resulting linear inverse problem by means of LSQR, with $\mathbf{A}$ relatively dense, for a large set of roughness-damping parameter values takes a further 3 hours.

Tomography with laterally heterogeneous starting models

As discussed in section 2.4.2, in a laterally heterogeneous Earth the form of a sensitivity function $K(\omega, \vartheta, \varphi)$ depends not only on epicentral distance, but also on the specific locations of source and receiver. For this reason, $K(\omega, \vartheta, \varphi)$ has to be calculated for each source-receiver pair, that is, for each observation in the database. At the speed of currently available hardware, this would be practically impossible if the "direct" approach algorithm of section 2.3.1 were used. It becomes feasible when the procedure described in section 2.3.2 is applied, thanks to the gain in speed achieved with the adjoint approach.

We limit ourselves, again, to Love-wave phase-anomaly observations at 150 s, and use as a starting phase-velocity model the one of Fig. 2.9, based on the crustal model Crust-2.0 and an isotropic upper-mantle model (section 2.4.2). We next

1. multiply the matrix **A** found in the homogeneous-model case by the vector of starting-model coefficients, and subtract the resulting phase-anomaly vector from the data; let us denote $\mathbf{d}'$ the resulting, corrected phase-anomaly vector;

2. following the method described in section 2.4.2, compute a sensitivity kernel for each of the $16,624$ summary observations (150 s Love waves only) available in the Harvard database; let us denote $K'_{i^{\rm th}\,{\rm datum}}(\omega,\vartheta,\varphi)$ the kernel associated with the i-th observation;

3. after a kernel is calculated, augment the matrix $\mathbf{A}'$ accordingly; the ij entry of $\mathbf{A}'$ is naturally defined

$$A'_{ij} = \int_{j^{\rm th}\,{\rm pixel}} K'_{i^{\rm th}\,{\rm datum}}(\omega,\vartheta,\varphi)\,{\rm d}\Omega, \tag{2.45}$$

   with the same pixel grid used in previous inversions (approximately equal-area pixels, 3° × 3° at the equator);

4. iterate the two previous steps until $\mathbf{A}'$ accounts for all available data;

5. dubbed $\mathbf{x}'$ the coefficients of perturbations to the starting model of Fig. 2.9, least-squares solve the linear inverse problem

$$\mathbf{A}'\cdot\mathbf{x}' = \mathbf{d}' \tag{2.46}$$

   repeatedly, for a wide range of values of the roughness damping parameter (again, no other regularization constraint is applied);

6. conduct a trade-off analysis to identify a preferred solution model, whose regularization is compatible with that applied in earlier experiments, so that the results can be compared (Boschi 2006).

The L-curve and its curvature resulting from the trade-off analysis (vi) are shown in Fig. 2.15a and 2.15b, respectively, as functions of normalized image roughness. The

Figure 2.15: Trade-off analysis for the phase-velocity inversions of sections 2.4.4 and 2.4.4 (heterogeneous starting model). (a) L-curves for solutions derived using numerical-adjoint kernels based on three different starting models: a homogeneous starting model (solid line, squares) (curve repeated from Fig. 2.13); the heterogeneous starting model shown in Fig. 2.9, which itself was derived from Crust-2.0 and an isotropic upper-mantle model (dotted line, crosses); the heterogeneous starting model shown in Fig. 2.14c, which itself was derived using numerical-adjoint kernels (dashed line, circles). (b) Curvature of the curves shown in (a).

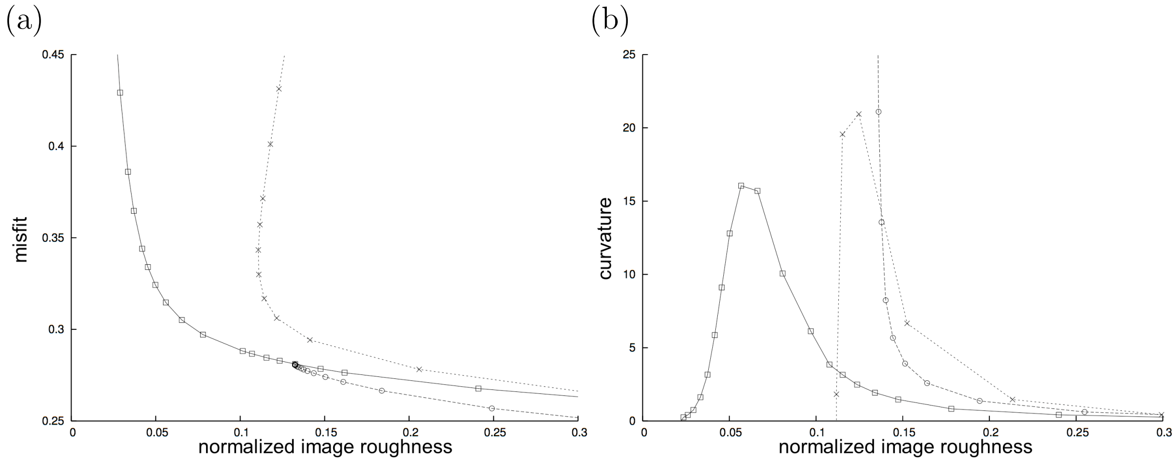

L-curve of Fig. 2.13 derived by numerical-adjoint kernels is also shown in Fig. 2.15 for comparison. Starting the inversion from a heterogeneous model, derived from Crust-2.0 and a spherically symmetric upper-mantle model (Fig. 2.9), leads to solutions with a worse datafit than the homogeneous-starting-model ones of equal roughness, suggesting that the chosen heterogeneous model does not describe sufficiently well the propagation of Love waves at 150 s period. As in this approach the starting model has nonzero roughness, the corresponding L-curve does not tend to zero for decreasing model complexity, but converges to the roughness value of the initial starting model.

We repeated this exercise, using as a starting model the one shown in Fig. 2.14c, derived from the inversions using numerical-adjoint kernels. This represents a first iteration step in a nonlinear inversion scheme where the zeroth iteration starts with a homogeneous phase-velocity model. Steps (ii), (iii), (iv) are the most time-consuming and took about 22 hours using 16 processors in our cluster. Step (v) takes about 3

Figure 2.16: Phase-velocity maps derived from inversions based on two different heterogeneous starting models. In each case the inversion employed sensitivity kernels calculated via the adjoint method for each respective heterogeneous model. In (a), the starting model is the phase-velocity map of Fig. 2.9, which was based upon Crust-2.0 and an isotropic upper-mantle model (see section 2.4.2). In (b), the starting model is the phase-velocity map of Fig. 2.14c, which was derived using numerical-adjoint kernels (see section 2.4.4).

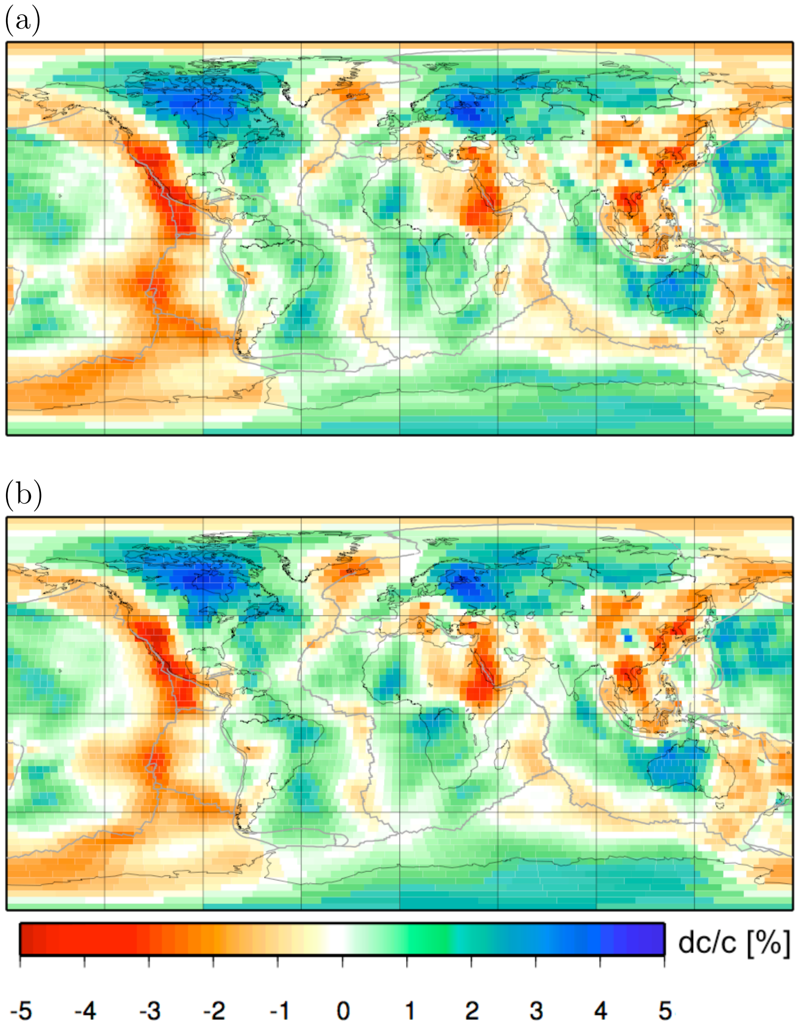

hours on a single processor, as in the homogeneous-model case: this is not surprising since $\mathbf{A}$ and $\mathbf{A}'$ are equally dense. The solutions obtained have a slightly better fit to the data than from the zeroth iteration. We iterated the process one more time, to find only insignificant changes in model and misfit.

The points of equal curvature in Fig. 2.15b (dotted line/crosses, dashed line/circles) identify our preferred solutions, which we show in Fig. 2.16. We first combine $\mathbf{x}'$ with the starting model (of Fig. 2.9 and Fig. 2.14c respectively), so that heterogeneities are again defined with respect to the value of 150 s Love-wave phase velocity predicted by PREM. Only few, small differences between the maps of Fig. 2.16 and those of Fig. 2.14 are apparent. Namely, in the top panel of Fig. 2.16 a fast, southeastern Atlantic anomaly can now be distinguished from the fast anomalies corresponding to cratons in western and southern Africa; the same happens in South America, where the fast anomaly in the southern Atlantic Ocean is more clearly separated from the Brazilian one. Using Crust-2.0 as a starting crustal model in a 3-D, ray-theoretical inversion, and then computing phase-velocity maps associated with the resulting 3-D shear velocity model, a similar effect is observed (unpublished result by L. Boschi, 2006, based on the method of Boschi & Ekström, 2002 and Boschi *et al.*, 2004).

We show in Fig. 2.17 the power spectrum up to degree 40 of the phase-velocity maps in Fig. 2.14 and Fig. 2.16. All spectra strongly resemble each other, particularly at lower harmonic degrees (longer spatial wavelengths). Notice that the phase-velocity maps obtained from laterally heterogeneous starting models (based on Crust-2.0 and an isotropic upper-mantle model; and based on an initial inversion from PREM) show slightly higher spectral values at degrees > 5.

2.5 Conclusions

We model surface wave propagation in a smoothly heterogeneous Earth, implementing the wave equation numerically on a spherical membrane (zero thickness). The numerical method utilizes a finite-differences scheme specifically designed for the spherical grids. In comparison with existing techniques, our approach has both advantages and disadvantages. It is less accurate than the fully 3-D, numerical solution of the Earth's equations of motion (e.g., Komatitsch *et al.* 2002; Capdeville *et al.* 2003) in that it requires the smooth-Earth/no-mode-coupling approximation to be made, but an order of magnitude faster. Unlike the analytical approaches like those of, e.g., Spetzler *et al.*

Figure 2.17: Harmonic spectra of models from Fig. 2.14 and Fig. 2.16. The power spectra are taken from the phase-velocity maps shown in Fig. 2.14, which were derived from a homogeneous starting model by ray theory (solid line, triangle), analytical Born theory (dashed line, pluses) and numerical-adjoint kernels (short-dashed line, squares), as well as the phase-velocity maps shown in Fig. 2.16, which were derived from the heterogeneous model shown in Fig. 2.9 (dashed-dotted line, crosses) and Fig. 2.14c (dotted line, circles) employing numerical-adjoint kernels.

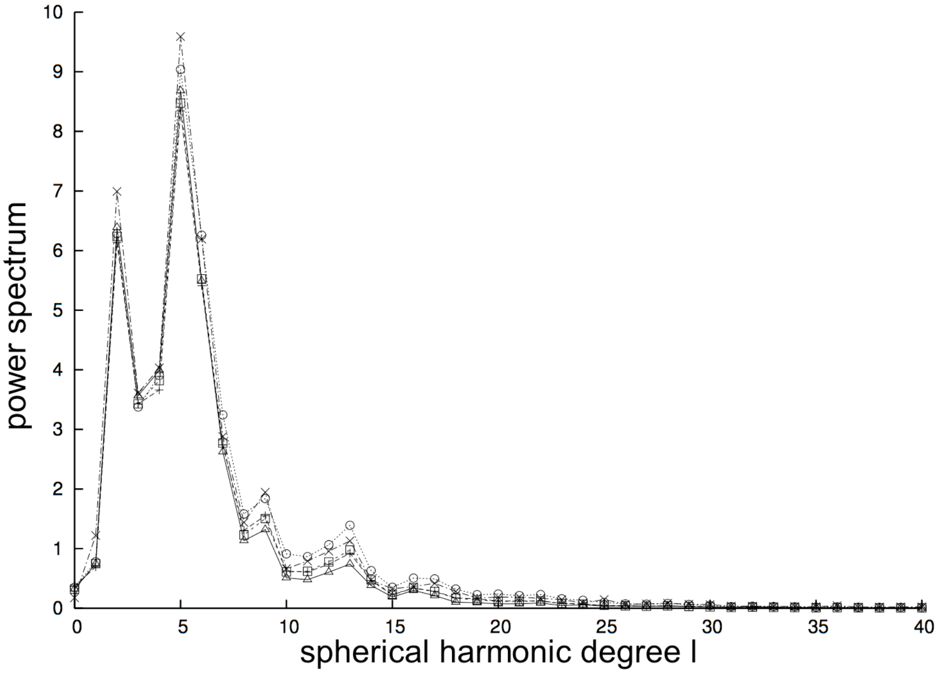

(2002); Zhou *et al.* (2004) and Yoshizawa & Kennett (2005), it does not involve any far-field approximation (Favier *et al.* 2004), and accounts for some of the nonlinearities of wave propagation in a realistic medium (Tanimoto 1990). Zhou *et al.*'s (2004) method, on the other hand, considers also mode coupling. Both Zhou *et al.*'s (2004) and Yoshizawa & Kennett's (2005) methods account for the effects of seismic source radiation, which our membrane analogue does not.

The high speed of our finite-difference membrane wave algorithm, combined with the application of the adjoint method (e.g., Tarantola 1984; Tromp *et al.* 2005), allowed us to use our membrane analogue to derive sensitivity kernels relating surface wave phase-anomaly data to phase-velocity heterogeneities. We computed sensitivity kernels using two different approaches — one employing adjoint methods, the other using a large set of direct calculations (no back-propagation) — and found coincident results (Fig. 2.6). We then calculated sensitivity kernels both in a homogeneous and a laterally heterogeneous starting model of phase velocity, and employed them in a set of global inversions of the Harvard dispersion database (e.g., Ekström *et al.* 1997). Kernels calculated in this way are free from the far-field approximation often used in analytical Born theory (e.g., Dahlen *et al.* 2000; Spetzler *et al.* 2002; Boschi 2006a). Fundamental-mode tomographic images and trade-off analyses (Figures 2.13 and 2.14) derived from different approaches (ray theory, analytical Born theory, numerical Born kernels) are approximately coincident (see also Fig. 2.17).

As explained in section 2.2, our membrane wave formulation of surface wave propagation relies on the assumption that lateral heterogeneities in upper-mantle structure are relatively smooth. In the near future, we shall extend our numerical-adjoint method approach to 3-D Earth models, where the only limit to possible Earth's complexity resides in the accuracy of its numerical discretization, and it will be easier to account for the specific geometry of seismic sources — neglected here — and definitions of phase anomaly more realistic than simple cross-correlation — employed here as a first approximation. Recently published applications of analytical finite-frequency methods to surface wave tomography (e.g., Zhou *et al.* 2004; 2005) suggest that the 3-D problem overcomes inherent ray theoretical assumptions made when inverting for 2-D phase-velocity maps as in this study; it will take account of depth-dependent radiation patterns for single scatterers. We therefore expect the 3-D experiment to bring an improvement in data fit and model quality, more significant than what was found here.

Acknowledgments

We thank Domenico Giardini for his support and encouragement, Yann Capdeville and Jeroen Tromp for their many insightful comments. We are grateful to Göran Ekström for making his dispersion database available to us. We would also like to thank T. Tanimoto, B. Romanowicz, G. Laske and an anonymous reviewer for critical and constructive comments. Funding for this project is provided by the European Commission's Human Resources and Mobility Program Marie Curie Research Training Network SPICE Contract No. MRTN-CT-2003-504267. Carl Tape's master thesis (Tape 2003) is available at http://www.gps.caltech.edu/∼carltape

Bibliography

[1] Aki, K. and P. G. Richards, 2002. *Quantitative Seismology*, 2nd ed., University Science Books, Sausalito, Calif., U.S.A.

[2] Baig, A. M., F. A. Dahlen and S. H. Hung, 2003. Traveltimes of waves in three-dimensional random media, *Geophys. J. Int.,* **153**(2), 467–482.

[3] Baig, A. M. and F. A. Dahlen, 2004. Statistics of traveltimes and amplitudes in random media, *Geophys. J. Int.,* **158**(1), 187–210.

[4] Bassin, C., G. Laske and G. Masters, 2000. The current limits of resolution for surface wave tomography in North America, *EOS, Trans. Am. geophys. Un.,* **81**(F897).

[5] Baumgardner, J. R. and P. O. Frederickson, 1985. Icosahedral Discretization of the Two-Sphere, *SIAM J. Num. Anal.,* **22**(6), 1107–1115.

[6] Boschi, L., 2001. Applications of linear inverse theory in modern global seismology, Ph.D. Thesis, Harvard University.

[7] Boschi, L. and G. Ekström, 2002. New images of the Earth's upper mantle from measurements of surface wave phase velocity anomalies, *J. geophys. Res.,* **107**(B4): 10.1029/2000JB000059.

[8] Boschi, L., G. Ekström and B. Kustowski, 2004. Multiple resolution surface wave tomography: the Mediterranean basin, *Geophys. J. Int.,* **157**, 293–304.

[9] Boschi, L., T. W. Becker, G. Soldati, and A. M. Dziewonski, 2006. On the relevance of Born theory in global seismic tomography, *Geophys. Res. Lett.,* **33**, L06302, doi:10.1029/2005GL025063.

[10] Boschi, L., 2006. Global Multi-Resolution Models of Surface Wave Propagation: Comparing Equivalently-Regularized Born- and Ray-Theoretical Solutions, *Geophys. J. Int.,* **167**(1), 238–252.

[11] Boschi, L., J.-P. Ampuero, D. Peter, P.M. Mai, G. Soldati, D. Giardini, 2007. Petascale computing and resolution in global seismic tomography, *Phys. Earth planet. Inter.,* doi:10.1016/j.pepi.2007.02.011.

[12] Bunge, H.-P. and Tromp, J., 2003. Supercomputing moves to universities and makes possible new ways to organize computational research, *EOS, Trans. Am. geophys. Un.,* **84**, 30—33.

[13] Capdeville, Y., E. Chaljub, J.-P. Vilotte and J.-P. Montagner, 2003. Coupling the spectral element method with a modal solution for elastic wave propagation in global Earth models, *Geophys. J. Int.,* **152**, 34–67.

[14] Capdeville, Y., 2005. An efficient Born normal mode method to compute sensitivity kernels and synthetic seismograms in the Earth, *Geophys. J. Int.,* **163**, 639–646.

[15] Carannante, S. and L. Boschi, 2005. Databases of surface wave dispersion, *Ann. Geophys.*, **48**, 945–955.

[16] Cui, J. and W. Freeden, 1997. Equidistribution on the sphere. *SIAM J. Sci. Comp.,* **18**(2), 595–609.

[17] Dahlen, F. A. and J. Tromp, 1998. *Theoretical Global Seismology*, Princeton University Press, Princeton, New Jers., USA

[18] Dahlen, F. A., S. H. Hung and G. Nolet, 2000. Fréchet kernels for finite-frequency traveltimes - I. Theory, *Geophys. J. Int.,* **141**(1), 157–174.

[19] de Hoop, M. V. and R. D. van der Hilst, 2005. On sensitivity kernels for 'wave-equation' transmission tomography, *Geophys. J. Int.,* **160**, 621–633.

[20] Dziewonski, A. M. and D. L. Anderson, 1981. Preliminary reference Earth model, *Phys. Earth planet. Inter.,* **25**, 297–356.

[21] Ekström, G., J. Tromp and E. W. F. Larson, 1997. Measurements and global models of surface wave propagation, *J. geophys. Res.,* **102**, 8137–8157.

[22] Favier, N., S. Chevrot and D. Komatitsch, 2004. Near-field influence on shear wave splitting and traveltime sensitivity kernels, *Geophys. J. Int.,* **156**, 467–482.

[23] Friederich, W., 1999. Propagation of seismic shear and surface waves in a laterally heterogeneous mantle by multiple forward scattering, *Geophys. J. Int.,* **136**, 180–204.

[24] Heikes, R. and D. A. Randall, 1995. Numerical integration of the shallow-water equations on a twisted icosahedral grid.1. Basic design and results of tests, *Mon. Weather Rev.*, **123**, 1862–1880.

[25] Heikes, R. and D. A. Randall, 1995. Numerical integration of the shallow-water equations on a twisted icosahedral grid.2. A detailed description of the grid and an analysis of numerical accuracy, *Mon. Weather Rev.*, **123**, 1881–1887.

[26] Hudson, J. A. and J. R. Heritage, 1981. The use of the Born approximation in seismic scattering problems, *Geophys. J. R. astr. Soc.,* **66**, 221–240.

[27] Hung, S. H., F. A. Dahlen and G. Nolet, 2000. Fréchet kernels for finite-frequency traveltimes - II. Examples, *Geophys. J. Int.,* **141**, 175–203.

[28] Hung, S. H., F. A. Dahlen and G. Nolet, 2001. Wavefront healing: a banana-doughnut perspective, *Geophys. J. Int.,* **146**, 289–312.

[29] Kennett, B. L. N., 1972. Seismic waves in laterally inhomogeneous media, *Geophys. J. R. astr. Soc.,* **27**, 301–325.

[30] Komatitsch, D., J. Ritsema and J. Tromp, 2002. The spectral-element method, Beowulf computing and global seismology, Science, **298**, 1737–1742.

[31] Li, X. D. and T. Tanimoto, 1993. Waveforms of long-period body waves in a slightly aspherical Earth model, *Geophys. J. Int.,* **112**(1), 92–102.

[32] Li, X. D. and B. Romanowicz, 1995. Comparison of global waveform inversions with and without considering cross-branch modal coupling, *Geophys. J. Int.,* **121**, 695–709.

[33] Marquering, H., F. A. Dahlen and G. Nolet, 1999. Three-dimensional sensitivity kernels for finite-frequency traveltimes: the banana-doughnut paradox, *Geophys. J. Int.,* **137**, 805–815.

[34] Moczo, P., J. Kristek and L. Halada, 2004. *The Finite-Difference Method for Seismologists. An Introduction.*, Comenius University, Bratislava.

[35] Nolet, G. and F. A. Dahlen, 2000. Wave front healing and the evolution of seismic delay times, *J. geophys. Res.,* **105**, 19043–19054.

[36] Press, W. H., S. A. Teukolsky, W. T. Vetterling and B. P. Flannery, 1992. *Numerical Recipes in FORTRAN: the Art of Scientific Computing*, 2nd ed. xxvi, 963, Cambridge University Press, Cambridge [England]; New York, N.Y., U.S.A.

[37] Randall, D. A., T. D. Ringler, R. P. Heikes, P. Jones and J. Baumgardner, 2002. Climate modeling with spherical geodesic grids, *Computing in Science & Engineering*, **4**, 32–41.

[38] Sadourny, R., A. Arakawa and Y. Mintz, 1968. Integration of nondivergent barotropic vorticity equation with an icosahedral-hexagonal grid for the sphere, *Mon. Weather Rev.*, **96**, 351–356.

[39] Saff, E. B. and A. B. J. Kuijlaars, 1997. Distributing many points on a sphere. *Math. Intelligencer,* **19**(1), 5–11.

[40] Smith, J. O. III, and X. Serra, 1987. PARSHL: An Analysis/Synthesis Program for Non-Harmonic Sounds Based on a Sinusoidal Representation, *Proceedings of the International Computer Music Conference (ICMC-87, Tokyo)*, Computer Music Association.

[41] Snieder, R., 1987. *Surface wave scattering theory, with applications to forward and inverse problems in seismology*, Ph.D. thesis, Utrecht University, the Netherlands.

[42] Snieder, R. and G. Nolet, 1987. Linearized scattering of surface waves on a spherical Earth, *J. Geophys.*, **61**, 55–63.

[43] Spetzler, J. and R. Snieder, 2001. The effect of small-scale heterogeneity on the arrival time of waves, *Geophys. J. Int.,* **145**, 786–796.

[44] Spetzler, J., J. Trampert and R. Snieder, 2002. The effect of scattering in surface wave tomography, *Geophys. J. Int.,* **149**, 755–767.

[45] Strohmaier, E., J. J. Dongarra, H. W. Meuer and H. D. Simon, 2005. Recent trends in the marketplace of high performance computing, *Parallel Computing*, **31**, 261–273.

[46] Stuhne, G. R. and W. R. Peltier, 1996. Vortex erosion and amalgamation in a new model of large scale flow on the sphere, *J. Comp. Phys.*, **128**, 58–81.

[47] Sword, C. H., J. F. Claerbout and N. H. Sleep, 1986. Finite-element propagation of acoustic waves on a spherical shell, *Stanford Exploration Project (SEP)*, **50**, 43–78.

[48] Talagrand, O., and P. Courtier, 1987. Variational assimilation of meteorological observations with the adjoint vorticity equation. I: Theory, *Q. J. R. Meteorol. Soc.*, **113**, 1311–1328.

[49] Tanimoto, T., 1990. Modelling curved surface wave paths: membrane surface wave synthetics, *Geophys. J. Int.,* **102**, 89–100.

[50] Tanimoto, T., 2003. Geometrical approach to surface wave finite frequency effects, *Geophys. Res. Lett.,* **30**, 1993, doi:10.1029/2003GL017475.

[51] Tape, C. H., 2003. *Waves on a Spherical Membrane*, M.Sc. thesis, University of Oxford, U.K.

[52] Tape, C., Liu, Q., and Tromp, J., 2007. Finite-frequency tomography using adjoint methods — Methodology and examples using membrane surface waves, *Geophys. J. Int.,* **168**(3), 1105 –1129.

[53] Tarantola, A., 1984. Inversion of seismic reflection data in the acoustic approximation, *Geophysics*, **49**, 1259–1266.

[54] Tong, J., F. A. Dahlen, G. Nolet and H. Marquering, 1998. Diffraction effects upon finite-frequency travel times: a simple 2-D example, *Geophys. Res. Lett.,* **25**, 1983–1986.

[55] Tromp, J. and F. A. Dahlen, 1993. Variational-principles for surface wave propagation on a laterally heterogeneous Earth.3. Potential representation, *Geophys. J. Int.,* **112**, 195–209.

[56] Tromp, J., C. Tape and Q. Liu, 2005. Seismic tomography, adjoint methods, time reversal and banana-doughnut kernels, *Geophys. J. Int.,* **160**, 195–216.

[57] Tsuboi, S., D. Komatitsch, C. Ji and J. Tromp, 2003. Broadband modeling of the 2002 Denali fault earthquake on the Earth Simulator, *Phys. Earth planet. Inter.,* **139**, 305–312.

[58] Wang, Z. and F. A. Dahlen, 1995. Spherical-spline parameterization of 3-dimensional Earth models, *Geophys. Res. Lett.,* **22**, 3099–3102.

[59] Wielandt, E., 1987. On the validity of the ray approximation for interpreting delay times, in *Seismic Tomography*, Nolet, G., editor, Reidel, Dordrecht.

[60] Williamson, D. L., 1968. Integration of barotropic vorticity equation on a spherical geodesic grid, *Tellus*, **20**, 642–653.

[61] Woodhouse, J. H. and T. P. Girnius, 1982. Surface waves and free oscillations in a regionalized Earth model, *Geophys. J. R. astr. Soc.,* **68**, 653–673.

[62] Wu, R. and K. Aki, 1985. Scattering characteristics of elastic waves by an elastic heterogeneity, *Geophysics*, **50**, 582–595.

[63] Yoshizawa, K. and B. L. N. Kennett, 2005. Sensitivity kernels for finite-frequency surface waves, *Geophys. J. Int.,* **162**, 910–926.

[64] Zhao, L., T. H. Jordan and C. H. Chapman, 2000. Three-dimensional Fréchet differential kernels for seismic delay times, *Geophys. J. Int.,* **141**, 558–576.

[65] Zhou, Y., F. A. Dahlen and G. Nolet, 2004. Three-dimensional sensitivity kernels for surface wave observables, *Geophys. J. Int.,* **158**, 142–168.

[66] Zhou, Y., F. A. Dahlen, G. Nolet and G. Laske, 2005. Finite-frequency effects in global surface-wave tomography, *Geophys. J. Int.,* **163**, 1087–1111.

3 Tomographic resolution of ray and finite-frequency theories: a membrane wave benchmark

3.1 Introduction

3.2 Asymptotic theory for membrane waves

3.2.1 Standing waves

3.2.2 Traveling waves on a homogeneous membrane

3.2.3 Ray theory on a heterogeneous membrane

3.3 Benchmark of different approaches to the forward problem

3.3.1 Benchmark of ray theory

3.3.2 Benchmark of finite-frequency theory

3.3.3 Multiple ray-path example

3.4 Benchmark of different approaches to the inverse problem

3.4.1 Data coverage

3.4.2 Scalelength test

3.4.3 Noise test

3.4.4 Amplitude test

3.4.5 Realistic input model test

3.5 Conclusions

This chapter will be submitted to *Geophys. J. Int.*, co-authors were Lapo Boschi and John Woodhouse.

Summary

The purpose of this study is to evaluate the resolution potential of current finite-frequency approaches to tomography, and to do that in a framework similar to that of global scale seismology. To our current knowledge and understanding, the only way to do this is by constructing a large set of "ground-truth" synthetic data computed numerically (spectral elements, finite differences, etc.), and then to invert them using the various available linearized techniques. The recent efforts of Qin *et al.* (2006) prove that this is extremely expensive to achieve when a fully realistic three-dimensional Earth model is used to compute the synthetics. We repeat Qin *et al.*'s (2006) study in a much simplified scenario, i.e. on a laterally heterogeneous membrane of zero thickness, as implemented by Peter *et al.* (2007). This amounts to drastically reducing the computational expense, with a certain loss of accuracy if the fine structure of a strongly heterogeneous Earth is to be modeled. Our benchmark is strictly valid for the propagation of elastic waves on a spherical, heterogeneous membrane, and, as shown by Peter *et al.* (2007), a good analogue for the propagation of surface waves within the outermost layers of the Earth. Our analysis suggests that a single-scattering, finite-frequency approach to tomography, with sensitivity kernels computed via the adjoint method, is significantly more powerful than ray-theory ones, as a tool to image the fine structure of the Earth.

3.1 Introduction

Surface waves propagate within the outermost shells of the Earth. While earthquakes and seismic stations are non-uniformly distributed all over the globe, surface waves travel through remote regions where no stations can be placed. They are thus sampling the Earth's upper mantle relatively uniformly. Depending upon their frequency, surface waves are sensitive to different depth ranges in the mantle. For these reasons, observations of surface waves are a precious source of information on the global structure of the Earth.

Many studies have been conducted to measure phase anomalies of surface waves with respect to an *a priori* reference Earth (Ekström *et al.* 1997; Trampert & Woodhouse 1995, 1996 and 2001; Laske 1995 and Laske & Masters 1996; van Heijst & Woodhouse 1999). They lead to excellent databases of phase anomalies for surface waves with periods down to about 35 seconds. The measurement techniques differ in the details (Trampert & Woodhouse 2001), but share the main principle, which consists of filtering the seismograms around a period of interest within a finite frequency-bandwidth. The signal is thus dissected into fundamental-mode and overtones as well as arrivals for multiple orbits. Synthetic seismograms are computed in a chosen, usually spherically symmetric, reference model. The phase anomalies are determined with respect to such synthetic seismograms by cross-correlation or some other fitting procedure (e.g., a downhill-simplex algorithm as in Ekström *et al.* 1997).

An inverse problem can then be formulated, to determine the structure through which the surfaces waves travelled. The immense database of phase-anomaly measurements are usually inverted for local phase velocities, thus leading to global phase-velocity distributions, which are, to first order, a linear combination of the underlying 3-D velocity structure. Before a seismic image is used for geodynamical interpretation or other applications, its resolution must be known. The resolution of tomography is influenced by many factors, e.g. by data coverage and measurement quality. It is often investigated by classical checkerboard tests (Lévêque *et al.* 1993), solving for resolution radii (e.g. Trampert & Woodhouse 1996) or, thanks to the continuous progress in computational power, solving for the full resolution matrices (e.g. Boschi, 2003; Boschi *et al.*, 2007).

All these studies are limited, in that the approximate theory used to formulate the inverse problem (ray theory) coincides with the theory used to compute synthetic data: inaccuracies in the solution models resulting from inaccuracies in the approximate formulations of wave propagation cannot be estimated (Lévêque *et al.* 1993). Like Qin *et al.* (2006), we overcome this problem by computing synthetic data with a numerical approach, capable, at least to some extent, of simulating nonlinear wave propagation effects in a laterally heterogeneous Earth. Because we limit ourselves to surface waves, we employ the membrane-wave method (Tanimoto 1990; Tape 2003; Tape *et al.* 2007; Peter *et al.* 2007).

In this study, we follow this approach to conduct a benchmark of tomographic algorithms based on ray theory versus single-scattering finite-frequency theory. Global tomographic inversions have mostly relied on ray theory due to its intuitive physical interpretation and computational efficiency. Ray theory is an infinite-frequency approximation. In practice, it is valid when the wavelength of the considered seismic wave is much smaller than the scalelength of the heterogeneities the wave is traveling through. When inverting for a phase-velocity model, ray theory assumes that any perturbation of phase is due to a perturbation of local phase velocities located on the ray of the considered phase. Especially for surface waves at larger periods, further away from the regime where ray theory is valid, this approximation might limit significantly tomographic resolution.

Single scattering of surface waves causes phase-anomaly measurements made over a finite-frequency bandwidth to be sensitive to phase-velocity perturbations distributed over large areas on the globe, and not only on the ray (Woodhouse & Girnius 1982; Li & Tanimoto 1993; Li & Romanowicz 1995; Dahlen *et al.* 2000; Hung *et al.* 2000; Spetzler *et al.* 2002; Zhou *et al.* 2004; Yoshizawa & Kennett 2005; Boschi 2006; Peter *et al.* 2007). These sensitivity areas, sometimes referred to as “banana-doughnut” kernels (Marquering *et al.* 1999; Dahlen *et al.* 2000; Hung *et al.* 2000), are unique for every single measurement. In the presence of adequate data coverage, finite-frequency theory is expected to reveal phase-velocity structures with spatial scalelengths even smaller than the wavelength under consideration.

In the past, comparisons made between ray and finite-frequency theory have not decisively determined whether current formulations of finite-frequency theory improve the resolution of tomographic images or not. For example, Spetzler *et al.* (2002), Boschi (2006) and Peter *et al.* (2007) found that phase-anomaly observations for Love waves at intermediate to long periods were equally well inverted by rays and banana-doughnuts. The same can be deduced from Sieminski *et al.* (2004) at the regional scale, where a test with synthetically computed fundamental Rayleigh-wave data and a realistic distribution of events and stations suggested no improvement when using banana-doughnuts. On the other hand, Ritzwoller *et al.* (2002) inverted surface-wave group-velocity measurements for group velocity models and found a clear difference at all periods between ray-theoretically and finite-frequency derived maps. Zhou *et al.* (2005) noted a slight improvement for finite-frequency theory as well, but limited to the case where three-dimensional sensitivity kernels were used to invert for seismic velocities directly, by-passing the derivation of phase-velocity maps. The statistical significance of such improvements remains to be determined.

In sections 3.2 and 3.3, we first benchmark the forward problem of predicting phase anomalies for a given phase-velocity model. In the first part of this study, we derive an asymptotic expression for membrane waves traveling on a sphere. It is worthwhile to find asymptotic solutions as they can provide further insights (Segel 1966) to complex problems. This analytical expression can further be used to calculate waveforms for heterogeneous background models, once the ray path between source and station is found. We validate phase-anomaly predictions made by exact ray theory and finite-frequency theory, comparing them with numerical "membrane-wave" results.

In the second part of this study we measure the accuracy of tomographic algorithms based on linearized ray-theory and finite-frequency tomography. The effects of scale-length, amplitude, noise and wavelength upon the imaging process are all specifically evaluated. We invert Love waves at intermediate to long periods with a realistic source-station distribution. The synthetic databases are comparable in size to existing ones. Additionally, we investigate the effects of realistic noise in the data upon the inversion solutions and show to which extent they complicate comparisons between ray and finite-frequency theory.

3.2 Asymptotic theory for membrane waves

To obtain the asymptotic, monochromatic waveforms of membrane waves (Tanimoto 1990; Tape 2003; Peter *et al.* 2007) for a laterally heterogeneous 1-D Earth, we first derive a traveling-wave expression of membrane waves for a homogeneous model. To then account for lateral heterogeneities, we calculate the phase and amplitude anomalies for a laterally heterogeneous phase-velocity distribution by a ray-tracing algorithm. We use them to correct the homogeneous waveforms.

3.2.1 Standing waves

The idea is to start from a standing-wave representation of membrane waves and derive an analytical, asymptotic formulation in terms of traveling waves. Dahlen & Tromp (1998) derived a traveling-wave decomposition of the standing-wave solution for the general three-dimensional case. We will conduct here a simplified treatment for waves propagating on a zero-thickness, spherical membrane.

An analytical solution $u(\theta, \phi, t)$ given at colatitude θ, longitude ϕ and time t for the wave equation on a spherical, zero-thickness membrane is available for a constant phase velocity c_0 (Tape 2003, eq. 3.34):

$$u(\theta, \phi, t) = c_0^2 \sum_{l=0}^{\infty} (l + \frac{1}{2})\, I_l(\mu)\, \cos(\omega_l t)\, e^{-\omega_l^2 \frac{\sigma^2}{2}} P_l(\cos\theta), \tag{3.1}$$

with P_l denoting the Legendre polynomials of degree l. The angular frequency ω_l at degrees $l = 0, 1, 2, ...$ is given by

$$\omega_l = \frac{c_0 \sqrt{l(l+1)}}{a} \tag{3.2}$$

for a given surface radius a. The integrals

$$I_l(\mu) = \int_0^{\pi} P_l(\cos(\alpha)) \frac{e^{-\frac{\alpha^2}{2\mu^2}}}{\mu^2} \sin(\alpha) d\alpha \tag{3.3}$$

can be evaluated numerically. The solution is valid for a prescribed forcing term

$$f(\theta, \phi, t) = \frac{e^{-\Delta^2/2\mu^2}}{\mu^2} \cdot \frac{-t}{\sigma^2} \frac{e^{-t^2/2\sigma^2}}{\sqrt{2\pi}\sigma}, \tag{3.4}$$

with arc-distance from the source $\Delta \in [0, \pi]$. The source parameters σ and μ govern the characteristic frequency content of the source. Note that the waveform $u(\theta, \phi, t)$ due to this initial source and given by eq. (3.1) is represented as a standing-wave summation.

Asymptotic approach

We rewrite eq. (3.1) with an asymptotic expression, valid for large degrees l, for the Legendre polynomials

$$P_l(\cos(\theta)) \approx \left\{ \frac{2}{\pi(l + \frac{1}{2}) \sin(\theta)} \right\}^{\frac{1}{2}} \cos\left[\left(l + \frac{1}{2} \right) \theta - \frac{\pi}{4} \right] \tag{3.5}$$

(Gilbert 1976, eq. 9) and substitute $\lambda = l + \frac{1}{2}$, so that the solution becomes

$$u(\theta, \phi, t) = \sum_{\lambda=\frac{1}{2},\frac{3}{2},\ldots}^{\infty} A_\lambda \cos(\omega_\lambda t) \cos\left(\lambda\theta - \frac{\pi}{4}\right), \tag{3.6}$$

where

$$\begin{aligned} \omega_\lambda &= \frac{c_0\sqrt{\lambda^2 - \frac{1}{4}}}{a}, && (3.7)\\ A_\lambda &= c_0^2 \lambda I_\lambda(\mu) \left\{\frac{2}{\pi\lambda\sin(\theta)}\right\}^{\frac{1}{2}} e^{-\omega_\lambda^2 \frac{\sigma^2}{2}}, && (3.8)\\ I_\lambda(\mu) &= \int_0^\pi P_{\lambda-\frac{1}{2}}\left(\cos(\alpha)\right) \frac{e^{-\frac{\alpha^2}{2\mu^2}}}{\mu^2} \sin(\alpha)\, d\alpha. && (3.9) \end{aligned}$$

Orbit separation

In the following, we separate even from odd orbits, following the derivation of Ferreira (2005, Appendix B.1). Hence, we substitute

$$\cos\left(\lambda\theta - \frac{\pi}{4}\right) = \frac{e^{i\lambda\theta}e^{-i\frac{\pi}{4}} + e^{-i\lambda\theta}e^{i\frac{\pi}{4}}}{2} \tag{3.10}$$

into eq. (3.6) and rewrite

$$u(\theta, \phi, t) = \sum_{\lambda=\frac{1}{2},\frac{3}{2},\ldots}^{\infty} \left[A_+(\lambda)e^{i\lambda\theta} + A_-(\lambda)e^{-i\lambda\theta})\right] \cos(\omega_\lambda t), \tag{3.11}$$

where

$$\begin{aligned} A_+(\lambda) &= \frac{1}{2} c_0^2 \lambda I_\lambda(\mu) \left\{\frac{2}{\pi\lambda\sin(\theta)}\right\}^{\frac{1}{2}} e^{-\omega_\lambda^2 \frac{\sigma^2}{2}} e^{-i\frac{\pi}{4}}, && (3.12)\\ A_-(\lambda) &= A_+^*(\lambda), && (3.13) \end{aligned}$$

with * denoting a complex conjugate. Note that the coefficients A_+ belong to waves for even orbits while the coefficients A_- to those for odd orbits.

Given the above solution by eq. (3.11), it is still necessary to find an expression for a single orbit. Applying the Poisson formula, the sum of a function $g(\lambda)$ can be written as

$$\sum_{\lambda=\frac{1}{2},\frac{3}{2},\dots} g(\lambda) = \int_0^\infty \sum_{s=-\infty}^{\infty} (-1)^s \, e^{-i\lambda 2\pi s} g(\lambda) \, d\lambda. \tag{3.14}$$

Thus, for eq. (3.11) we obtain

$$u(\theta,\phi,t) = \sum_{s=-\infty}^{\infty} (-1)^s \int_0^\infty \left[A_+(\lambda)e^{-i\lambda(2\pi s-\theta)} + A_-(\lambda)e^{-i\lambda(2\pi s+\theta)}\right] \cos(\omega_\lambda t) \, d\lambda. \tag{3.15}$$

It becomes useful to transform this expression into the frequency domain to find explicit solutions to the integrals. Using the Fourier transformation (non-unitary) of

$$f(t) = \begin{cases} 0 & \text{for } t < 0 \\ \cos(\omega_\lambda t) & \text{for } t \geq 0 \end{cases} \tag{3.16}$$

we can write in the frequency domain

$$\begin{aligned} \tilde{f}(\omega) &= \int_{-\infty}^0 0 \cdot e^{-i\omega t} dt + \int_0^\infty \cos(\omega_\lambda t) \cdot e^{-i\omega t} dt & (3.17) \\ &= \frac{1}{2} \int_0^\infty \left[e^{-it(\omega-\omega_\lambda)} + e^{-it(\omega+\omega_\lambda)}\right] dt & (3.18) \\ &= \frac{1}{2} \left[\frac{1}{i(\omega-\omega_\lambda)} + \frac{1}{i(\omega+\omega_\lambda)}\right] & (3.19) \\ &= \frac{\omega}{i(\omega^2-\omega_\lambda^2)}. & (3.20) \end{aligned}$$

It follows that eq. (3.15) in the frequency domain takes the form

$$u(\theta,\phi,\omega) = \sum_{s=-\infty}^{\infty} (-1)^s \int_0^\infty \left[A_+(\lambda)e^{-i\lambda(2\pi s-\theta)} + A_-(\lambda)e^{-i\lambda(2\pi s+\theta)}\right] \frac{\omega}{i(\omega^2-\omega_\lambda^2)} \, d\lambda, \tag{3.21}$$

which has single poles at $\omega = \pm\omega_\lambda$.

The residue theorem states

$$\oint f(z) dz = 2\pi i \sum \operatorname{Res}\left[f(z)\right] \tag{3.22}$$

where the residue for a single, simple pole of order 1 is obtained by

$$\mathrm{Res}_{z=z_0}\left[f(z)\right] = lim_{z\rightarrow z_0}(z-z_0)f(z). \tag{3.23}$$

Therefore, we can write as the relevant summation of residues for eq. (3.21)

$$\begin{aligned}\oint f(z)dz &= 2\pi i \sum \mathrm{Res}_{z=\pm\omega_\lambda}\left[\tilde{f}(\omega)\right] &(3.24)\\ &= 2\pi i \sum \mathrm{Res}_{z=\pm\omega_\lambda}\left[\frac{\omega}{i(\omega^2-\omega_\lambda^2)}\right] &(3.25)\\ &\approx 2\pi i\left(\frac{a}{2c_0 i}+\frac{a}{2c_0 i}\right) = \frac{2\pi a}{c_0}, &(3.26)\end{aligned}$$

using the approximation $\omega_\lambda \approx \frac{c_0\lambda}{a}$ for large degrees l.

Looking at eq. (3.21) and ignoring terms $A_\pm(-\lambda(\omega))$, we get

$$u(\theta,\phi,\omega) \approx \sum_{s=-\infty}^{\infty}(-1)^s\left[A_+(\lambda(\omega))e^{-i\lambda(\omega)(2\pi s-\theta)} + A_-(\lambda(\omega))e^{-i\lambda(\omega)(2\pi s+\theta)}\right]\frac{2\pi a}{c_0}. \tag{3.27}$$

3.2.2 Traveling waves on a homogeneous membrane

Finally, eq. (3.27) has to be Fourier-transformed back to time domain

$$u(\theta,\phi,t) \approx \frac{1}{2\pi}\int_{\infty}^{\infty}\sum_{s=-\infty}^{\infty}(-1)^s\left[A_+(\lambda(\omega))e^{-i\lambda(\omega)(2\pi s-\theta)} + A_-(\lambda(\omega))e^{-i\lambda(\omega)(2\pi s+\theta)}\right]\frac{2\pi a}{c_0}e^{i\omega t}\,d\omega. \tag{3.28}$$

The traveling-wave solutions for different orbits follow from this expression. For example, for odd orbits we set $A_+(\lambda(\omega)) \equiv 0$ and use $s = 0, 1, 2, ...$ for the first, third, fifth and so on orbit. The corresponding expressions for the first and third orbits are

$$\begin{aligned}\text{R1: }\ u(\theta,\phi,t) &\approx \frac{a}{c_0}\int_{-\infty}^{\infty}A_-(\lambda(\omega))e^{-i\lambda(\omega)\theta}e^{i\omega t}\,d\omega &(3.29)\\ \text{R3: }\ u(\theta,\phi,t) &\approx -\frac{a}{c_0}\int_{-\infty}^{\infty}A_-(\lambda(\omega))e^{-i\lambda(\omega)(2\pi+\theta)}e^{i\omega t}\,d\omega. &(3.30)\end{aligned}$$

For even orbits, we set $A_-(\lambda(\omega)) \equiv 0$ and use $s = 1, 2, 3, ...$ for the second, forth, sixth and so on orbit. The following expressions are for the second and forth orbits:

$$\text{R2: } u(\theta,\phi,t) \approx -\frac{a}{c_0}\int_{-\infty}^{\infty} A_+(\lambda(\omega))e^{-i\lambda(\omega)(2\pi-\theta)}e^{i\omega t}\,d\omega \tag{3.31}$$

$$\text{R4: } u(\theta,\phi,t) \approx \frac{a}{c_0}\int_{-\infty}^{\infty} A_+(\lambda(\omega))e^{-i\lambda(\omega)(4\pi-\theta)}e^{i\omega t}\,d\omega. \tag{3.32}$$

We calculate the integrands of eqs. (3.29) through (3.32) at each ω explicitly, and use a numerical integration to find $u(\theta,\phi,t)$. The Legendre polynomials for non-integer values of the angular degree

$$l(\omega) = \lambda(\omega) - \frac{1}{2}, \tag{3.33}$$

with

$$\lambda(\omega) = \sqrt{\frac{\omega^2 a^2}{c_0^2} + \frac{1}{4}}, \tag{3.34}$$

are found numerically by spline interpolation. The coefficients $A_+(\lambda(\omega))$ and $A_-(\lambda(\omega))$ are given by eq. (3.12) resp. (3.13). Similarly, the integrals $I_\lambda(\mu)$, given by eq. (3.9), were interpolated by splines for non-integer values of the angular degree $l(\omega)$.

Waveform example

We choose an initial source-station couple with epicentral distance of about 90 degrees. Figure 3.1 shows the waveform for the fourth orbit obtained by the asymptotic approach of eq. (3.32) against the numerical solution, calculated by finite-differences integration on a spherical membrane (Peter *et al.*, 2007). Note that the numerical solution provides all orbits up to the finishing time during the forward integration.

The asymptotic waveform exhibits a slightly smaller amplitude at maximum displacement as the numerical one. The phase offset between the two is negligible. The agreement in this homogeneous case is good enough to proceed and obtain an asymptotic trace for a laterally heterogeneous model.

3.2.3 Ray theory on a heterogeneous membrane

The asymptotic approach provides us with a waveform for a homogeneous membrane-wave model. To extend the treatment of section 3.2.2 to the heterogeneous case, we first use the laws of optics to determine the ray path travelled by a wave (Woodhouse &

Figure 3.1: Waveform solutions on a spherical membrane by the asymptotic approach for the fourth orbit (green), or calculated numerically (red) with the finite-differences membrane-wave model of Peter *et al.* (2007).

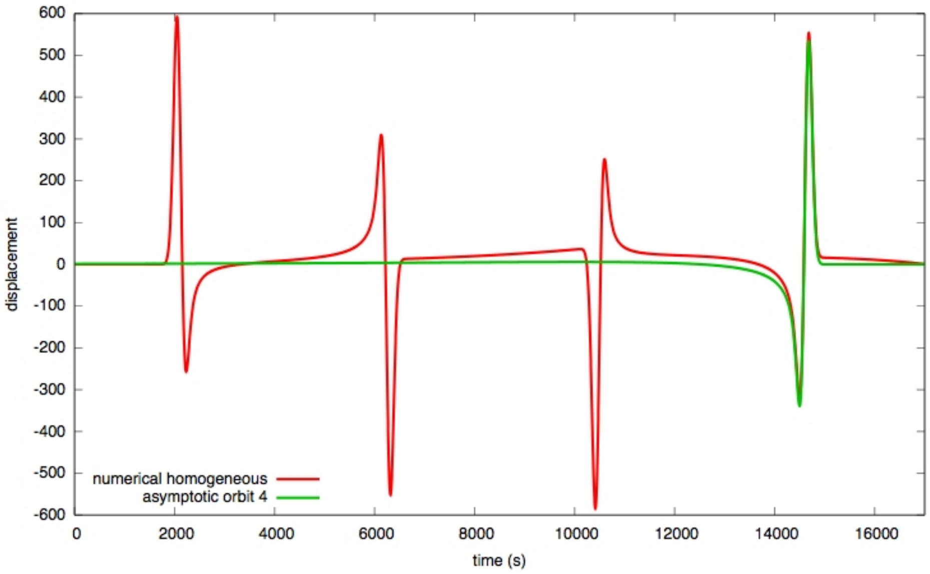

Wong 1986; Boschi & Woodhouse 2006), then compute the phase by integration along such a ray.

Ray-tracing

In order to calculate the phase ψ_{het} for a heterogeneous background model

$$\psi_{het} = \int_{ray} \frac{\omega}{c(\theta, \phi)} ds \tag{3.35}$$

with local phase velocities $c(\theta, \phi)$, we need to compute the corresponding ray between the seismic source and a receiver station, a problem treated by Woodhouse & Wong (1986) for the sphere. For brevity, we just give the two equations which relate to our case here. We simultaneously solve for $\gamma(\phi) \equiv cot\,\theta$ and $\gamma'(\phi) = \frac{d\gamma}{d\phi}(\phi)$ in equations (33) and (38) of Woodhouse & Wong (1986):

$$\frac{d^2\gamma}{d\phi^2}+\gamma = (\frac{\nu^2}{1+\gamma^2})(\partial_\theta-\nu\partial_\phi)\ln c(\theta,\phi) \tag{3.36}$$

$$\begin{aligned}\frac{d^2\gamma'}{d\phi^2}+\gamma' &= \frac{2\nu}{1+\gamma^2}(\nu'-\frac{\nu\gamma\gamma'}{1+\gamma^2})(\partial_\theta-\nu\partial_\phi)\ln c(\theta,\phi)\\ &-(\frac{\nu^2}{1+\gamma^2}+1)\frac{\gamma'}{1+\gamma^2}(\partial_\theta^2-\nu\partial_\theta\partial_\phi)\ln c(\theta,\phi)\\ &-(\frac{\nu^2}{1+\gamma^2}+1)\nu'\partial_\phi\ln c(\theta,\phi)\end{aligned} \tag{3.37}$$

where $\nu(\phi)\equiv-\gamma'(\phi)=-\frac{d\gamma}{d\phi}(\phi)$ and $'$ denotes differentiation with respect to the initial value of ν, at constant ϕ. The boundary conditions are $\gamma'(0)=0$ and $\nu'(0)=1$.

Ray-theoretical travel-time anomalies

Let us rotate the reference frame such that source and receiver are located on the equator. ϕ_k becomes the epicentral distance between source and receiver. For a homogeneous reference model, the phase $\psi_{hom}(\phi_k)$ can be written as

$$\psi_{hom}(\phi_k) = \int_{ray}\frac{\omega a}{c_0}d\phi=\frac{\omega a\phi_k}{c_0}, \tag{3.38}$$

where a is the Earth's radius and c_0 the constant phase velocity for the reference model. The phase anomaly $\delta\psi$ is defined as the difference in phase from that in the reference model, i.e. (Woodhouse & Wong 1986, eq. 42)

$$\delta\psi(\phi_k) \equiv \psi_{het}(\phi_k)-\psi_{hom}(\phi_k) \tag{3.39}$$

$$= \frac{\omega a}{c_0}\int_0^{\phi_k}\left[\frac{c_0}{c(\theta,\phi)}\left\{\frac{\nu(\phi)^2}{[1+\gamma^2(\phi)]^2}+\frac{1}{1+\gamma^2(\phi)}\right\}^{\frac{1}{2}}-1\right]d\phi. \tag{3.40}$$

Note that the phase anomaly $\delta\psi$ is calculated for a single frequency $\omega=\frac{2\pi}{\hat{T}}$ at a certain reference period $\hat{T}$.

We use local phase velocities $c(\theta,\phi)$ which are derived from maps of relative phase-velocity perturbations $\frac{\delta c(\theta,\phi)}{c_0}=\frac{c(\theta,\phi)-c_0}{c_0}$ at given $\hat{T}$ taken from Trampert & Woodhouse (1995).

We can define

$$y(\phi_k) = \int_0^{\phi_k} \left[\frac{c_0}{c(\theta, \phi)} \left\{ \frac{\nu(\phi)^2}{[1 + \gamma^2(\phi)]^2} + \frac{1}{1 + \gamma^2(\phi)} \right\}^{\frac{1}{2}} - 1 \right] d\phi, \tag{3.41}$$

so that

$$\frac{dy}{d\phi} = \frac{c_0}{c(\theta, \phi)} \left\{ \frac{\nu(\phi)^2}{[1 + \gamma^2(\phi)]^2} + \frac{1}{1 + \gamma^2(\phi)} \right\}^{\frac{1}{2}} - 1. \tag{3.42}$$

This can be solved simultaneously with the other equations (3.36) and (3.37) from above.

We prefer working with travel-time anomalies, thus we make use of the identity between relative phase anomalies and relative travel-time anomalies

$$\frac{\delta\psi}{\psi_{hom}} = \frac{\delta T}{T_0}, \tag{3.43}$$

where T_0 denotes the travel-time for the reference model. From eq. (3.38), we find

$$\delta\psi \;=\; \psi_{hom} \cdot \frac{\delta T}{T_0} = \frac{\omega a \phi_k}{c_0} \cdot \frac{\delta T \, c_0}{a \phi_k} = \omega \cdot \delta T. \tag{3.44}$$

Thus, we divide the phase anomaly $\delta\psi$ by the angular frequency ω to obtain travel-time anomalies δT (of units in seconds).

3.3 Benchmark of different approaches to the forward problem

In order to compare predictions of travel-time anomalies, we use a setup of 38 receiver stations located at about 90° epicentral distance from one source at 0° N, 0° E. The heterogeneous phase-velocity model for Love waves at about 150 s period is taken from Trampert & Woodhouse (1995). We conduct a series of independent experiments, where we expand the model up to degree 4, 8, 12 or 20 respectively. The setup is similar to the one used in Tape (2003). For each source-station couple we consider arrivals up to the fourth orbit, thus at least 152 prediction values are compared for each of the four different models. The numerically derived values, which are recalculated for each model with different degree of complexity, can be seen as the “ground-truth” values, which the predicted ones should match in an ideal case.

3.3.1 Benchmark of ray theory

We first compare the ray-theoretical predictions of travel-time anomalies against numerically calculated travel-time anomalies. A reference trace for the homogeneous model and a second trace for the heterogeneous model are computed numerically with the finite-differences approach of Peter *et al.* (2007). We bandpass-filter the two numerical traces around an angular frequency ω, for which we have also determined ray-theoretical travel-time anomalies δT according to eq. (3.44). The bandpass-filter uses a half-bandwidth of 2.5 mHz around the center frequency ω. Following Ekström *et al.* (1997), we then determine the corresponding numerical travel-time anomaly by a nonlinear downhill-simplex algorithm (Nelder & Mead 1965). We checked this algorithm against a cross-correlation measurement technique and found almost identical results for the phase anomalies.

Figure 3.2 compares the travel-time anomalies δT calculated by eq. (3.44) (RAY-exact) with the corresponding ground-truth data, computed numerically. Values on the diagonal correspond to perfect agreement. We see that exact ray theory predicts the first-orbit anomalies accurately; for higher orbits (shown with different symbols), the values are more scattered around the diagonal, particularly for models with energy at increasingly high harmonic degrees (compare Figure 3.2a with 3.2b, 3.2c and 3.2d). In general, the plots of Figure 3.2 are in agreement with the results of Tape (2003). Particularly large differences between the ray-theoretical prediction and the ground-truth value for higher orbits and expansions are observed when multiple ray paths between source and receiver location exist (in such cases, we plot in Figure 3.2 the phase-anomaly associated with the first ray found by our ray-tracing algorithm).

In general, Figure 3.2 confirms two aspects of ray theory: first, ray-theoretical predictions are closely related to the ratio between the scalelength Λ of heterogeneities and the wavelength λ under consideration. Predictions are valid when $\lambda \ll \Lambda$, and the fit systematically decreases as the maximum harmonic degree of heterogeneity grows, from Figure 3.2a to 3.2d. Secondly, we see that ray-theoretical predictions depend on the travelled epicentral distance between source and receiver location. The longer the travelled distance (the higher the orbit), the less accurate ray-theoretical predictions become.

Figure 3.2: Ray-theoretical predictions of travel-time anomalies (RAY-exact) are plotted versus the numerically calculated, ground-truth ones (numerical travel-time anomaly) for 38 source-station couples with about 90° epicentral distance. The source is located at 0° N / 0° E. The phase-velocity map is taken from Trampert & Woodhouse (1995) filtered to maximum harmonic degree (a) 4, (b) 8, (c) 12 and (d) 20. Predictions for the first orbit are plotted as dots (filled), second orbit as squares, third orbit as triangles and fourth orbit as circles.

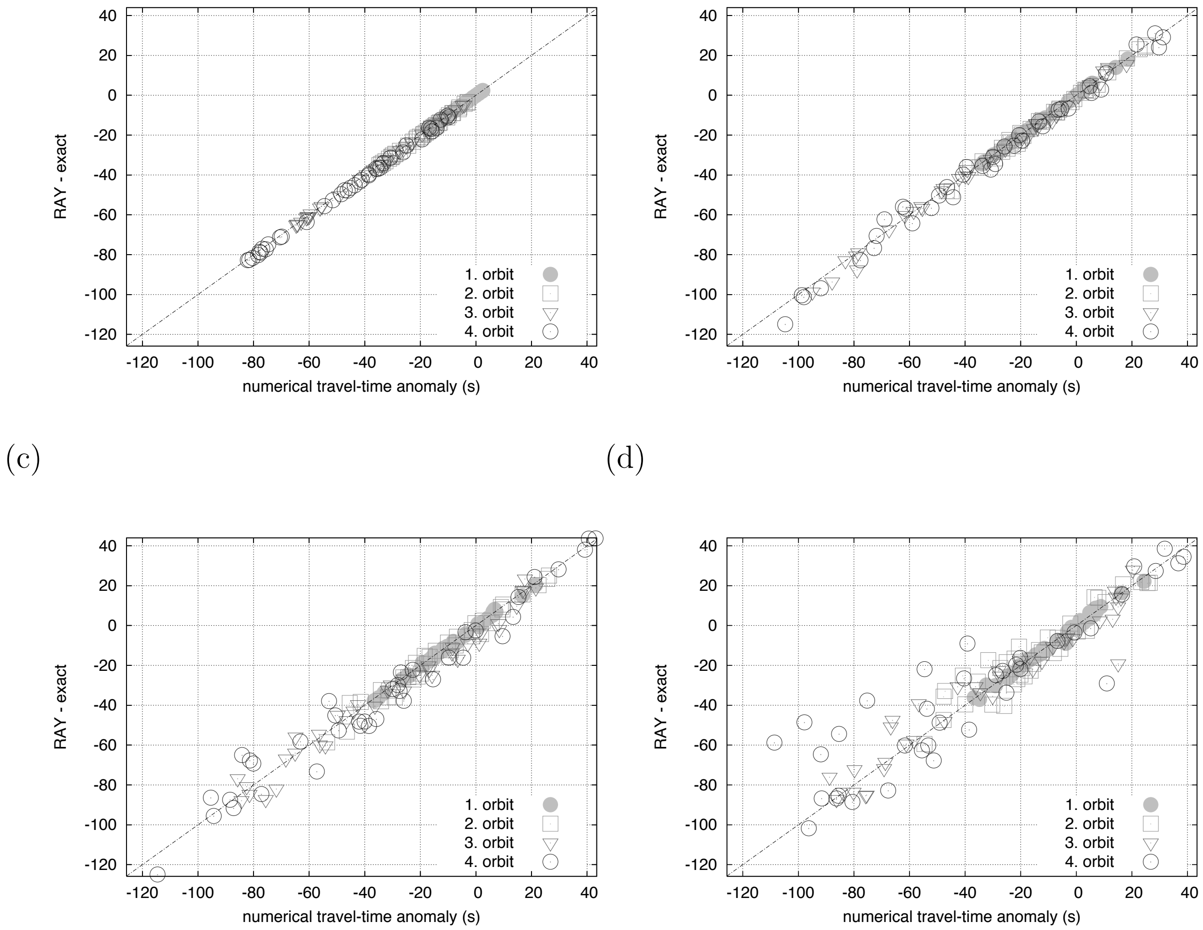

(a) (b) (c) (d)

3.3.2 Benchmark of finite-frequency theory

We also consider the travel-time anomalies δT predicted on the basis of the finite-frequency kernels derived by the single scattering approximation, specifically the numerical kernels $K_{num}(\theta, \phi)$ from Peter *et al.* (2007). These kernels were derived by the adjoint method (Tromp *et al.* 2005 and references therein) and computed for the homogeneous background model. We calculate the corresponding travel-time anomaly δT by integrating

$$\frac{\delta T}{T_0} = \int_\Omega K_{num}(\theta, \phi) \, \frac{\delta v}{v_0} \, d\Omega \tag{3.45}$$

over the whole surface Ω of the membrane, and multiplying with the reference travel time T_0 of the homogeneous case. $\frac{\delta v}{v_0}$ denotes relative phase-velocity perturbations in the model of Trampert & Woodhouse (1995) expanded up to degree 4, 8, 12 or 20. Figure 3.3 compares the travel-time anomalies δT calculated this way, with the corresponding ground-truth ones. The kernels $K_{num}(\theta, \phi)$ are computed for every orbit separately. An example of the numerical kernels for a particular source-station couple for all four orbits is given in Figure 3.4. Note that the shape of the kernels is strongly affected by the filtering (corresponding to the measurement technique) with a half-bandwidth of 2.5 mHz.

Analyzing the scatter in Figures 3.2 and 3.3, we find that finite-frequency predictions for the first orbit are more accurate than the ray-theoretical ones of Figure 3.2. As a quantitative measure of scatter, we used a linear regression to calculate the RMS of the residuals, which for ray-theoretical predictions of first orbit arrivals range between $0.06 - 1.36$ s for the background phase-velocity map filtered to degree 4, 8, 12 and 20 (Figures 3.2a to 3.2d). The corresponding RMS range for residuals of the finite-frequency predictions of first orbit arrivals shown in Figure 3.3a to 3.3d are between $0.05 - 0.57$ s. At higher orbits, the situation is reversed, with ray theory predicting ground-truth travel-time anomalies more accurately than the finite-frequency kernels. We tested these numerical kernel predictions also against predictions from analytical kernels for the first and second orbit, calculated as in Spetzler *et al.* (2002). The scatterplot results shown in Figure 3.5a to 3.5d are analogous to those found from numerical kernels. The RMS of the residuals of the (analytical) finite-frequency predictions range for the first orbit between $0.08 - 0.68$ s. For second orbit arrivals, they range between $0.79 - 8.83$ s, compared to $0.92 - 8.40$ s for the predictions based on numerical sensitivity kernels and

Figure 3.3: Finite-frequency predictions of travel-time anomalies (Finite-Frequency) calculated via eq. (3.45) are plotted versus the numerically calculated ones (numerical travel-time anomaly). Source, stations and Earth model are the same as in Figure 3.2. The phase-velocity map from Trampert & Woodhouse (1995) is filtered to maximum harmonic degree (a) 4, (b) 8, (c) 12 and (d) 20. Predictions for the first orbit are plotted as dots (filled), second orbit as squares, third orbit as triangles and fourth orbit as circles.

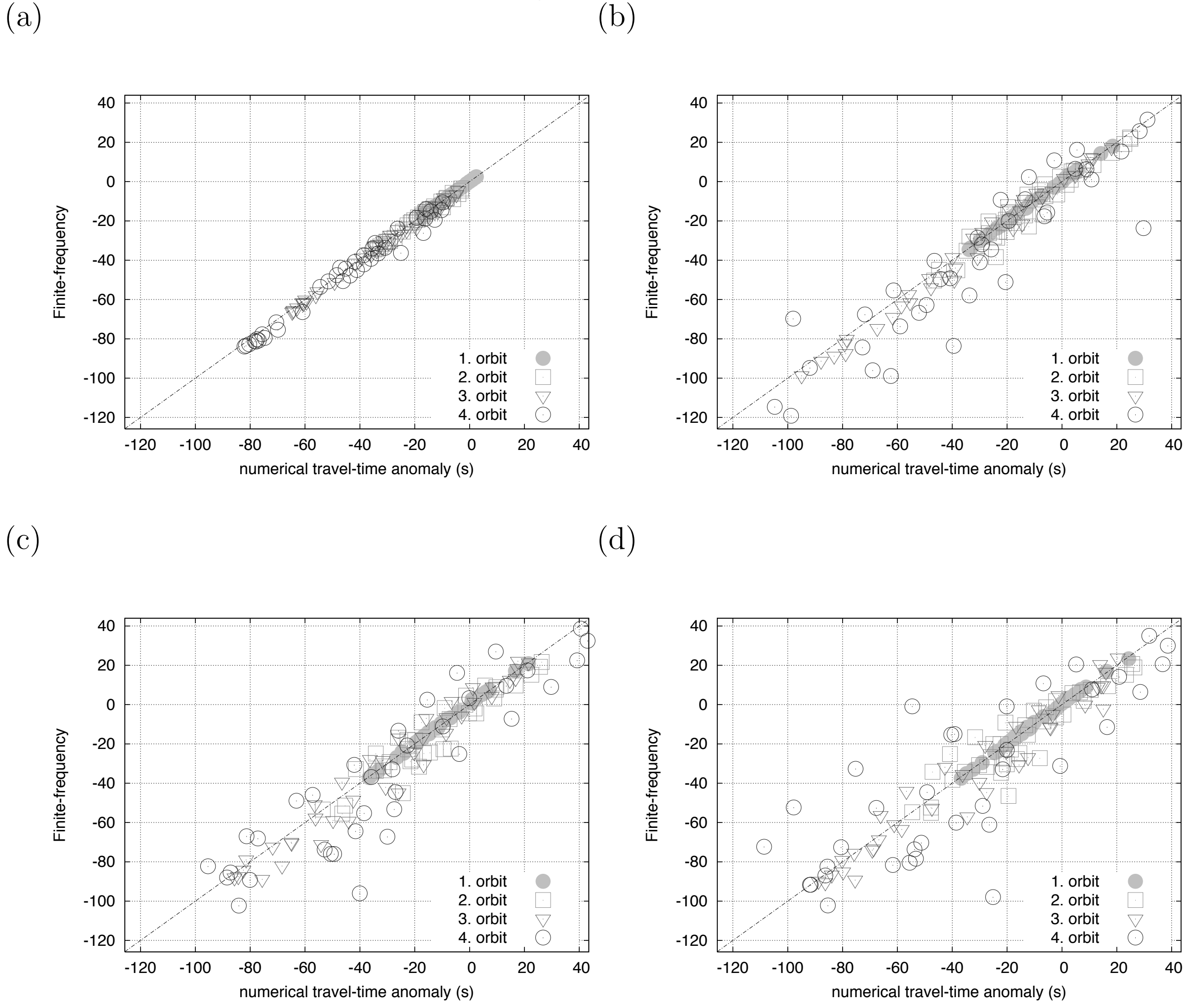

Figure 3.4: Example of numerical sensitivity kernels (Peter *et al.* 2007), based on the adjoint method, used for the predictions of travel-time anomalies (Finite-frequency) in Figure 3.3 for the source located at 0° N / 0° E and a receiver at 0° N / 90° E. Plotted are the relative travel-time kernels for the (a) first, (b) second, (c) third and (d) fourth orbit.

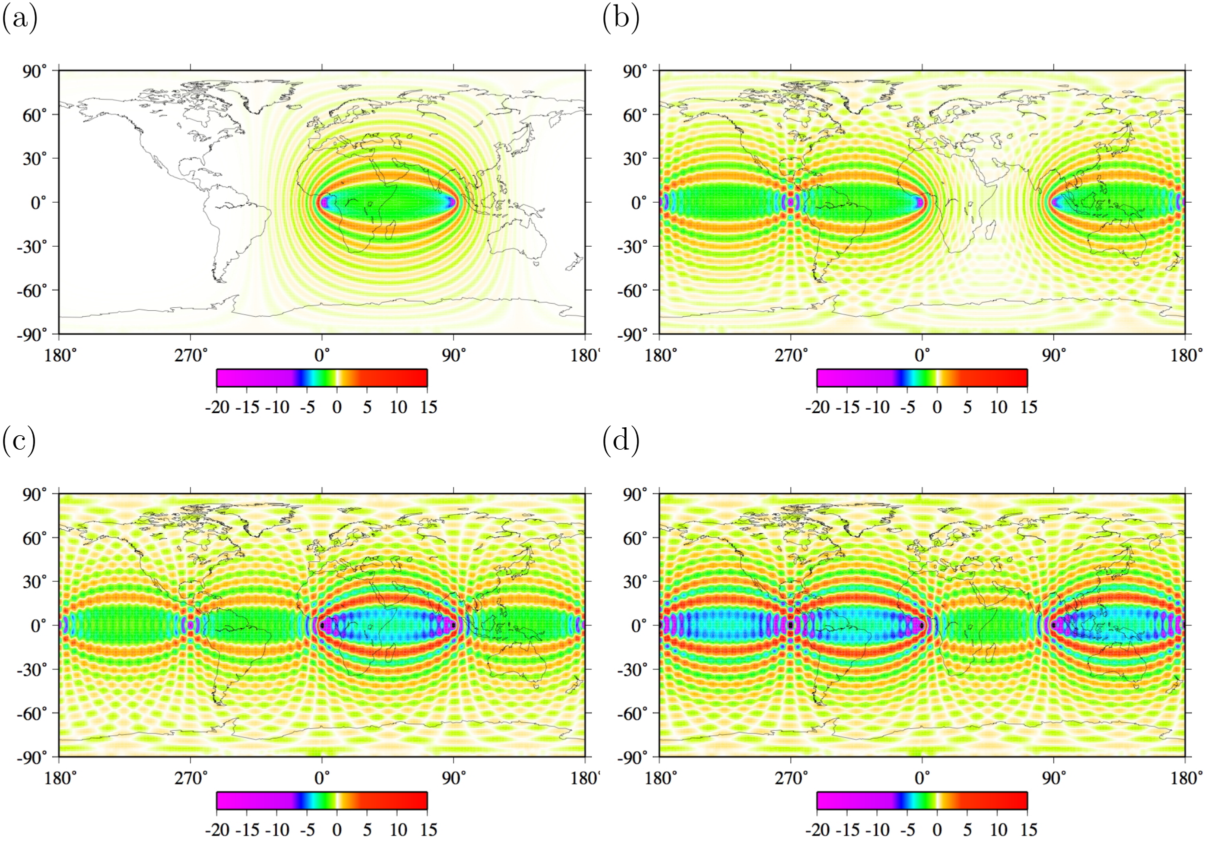
(a)
(b)
(c)
(d)
90°
60°
30°
0°
-30°
-60°
-90°
180°
270°
0°
90°
180°
-20 -15 -10 -5 0 5 10 15

0.19 – 6.99 s for the ray-theoretical ones. A similar effect had been noted in attempts to compute higher-orbit travel times by the integration of fully 3-D surface wave kernels (personal communication with Y. Capdeville).

The accuracy of prediction depends upon the ratio of the scalelength Λ of heterogeneities to the width W of the first Fresnel zone. Baig *et al.* (2003) and Dahlen (2004) define a dimensionless "doughnut-hole" parameter D valid for their 3-D banana-doughnut kernels in a cartesian box model

$$D^{3D} = \frac{\Lambda}{W} = \frac{\Lambda}{\sqrt{\lambda \cdot L}} \text{ (3-D cartesian)}, \tag{3.46}$$

where L denotes the travelled distance and λ the wavelength. Spetzler & Snieder (2001) adapted the width $W = \sqrt{\frac{3}{2}\lambda \tan(\frac{L}{2})}$ to spherical geometry, limited to the 2-D (surface-wave phase velocity) case, thus

$$D^{2D} = \frac{\Lambda}{W} = \frac{\Lambda}{\sqrt{\frac{3}{2}\lambda \tan(\frac{L}{2})}} \text{ (sphere)}. \tag{3.47}$$

In general, it is assumed that for $D \rightarrow \infty$, ray-theoretical predictions would become perfectly accurate.

For wave propagation in a weakly heterogeneous, 3-D cartesian box, Baig *et al.* (2003) found that banana-doughnut predictions are accurate for $D^{3D} \geq 0.1$, and ray-theoretical ones only for $D^{3D} \geq 0.5$. Yang & Hung (2005) found that for analytical banana-doughnut kernels, in a similar 3-D case, travel-time predictions are only accurate for weakly heterogeneous media with perturbations $\leq 3\%$. Their fig. 2 shows that "Born" theory predictions are less accurate than those of exact (general) ray theory for $1.1 \leq D^{3D} \leq 1.5$. In our heterogeneous models, phase-velocity perturbations can amount to about ±6%, and depending upon the maximum degree of harmonic expansion, Λ varies between $1'953 - 8'896\,km$, with corresponding doughnut-hole parameters $0.7 \leq D^{2D} \leq 3.4$ (for our first orbit kernels with 90° epicentral distances). In this scenario, we find finite-frequency kernels to perform better than ray theory as a solution to the forward problem.

Figure 3.5: Finite-frequency predictions of travel-time anomalies using analytical sensitivity kernels for minor- and major-arcs as described by Spetzler *et al.* (2002). Source, stations and Earth model are the same as in Figure 3.3. The phase-velocity map from Trampert & Woodhouse (1995) is filtered to maximum harmonic degree (a) 4, (b) 8, (c) 12 and (d) 20. Predictions are shown for the first (dots, filled) and second orbit (squares). An example, similar to Figure 3.4, of the analytical sensitivity kernels for the source located at 0° N / 0° E and a receiver at 0° N / 90° E is given for the (e) first and (f) second orbit.

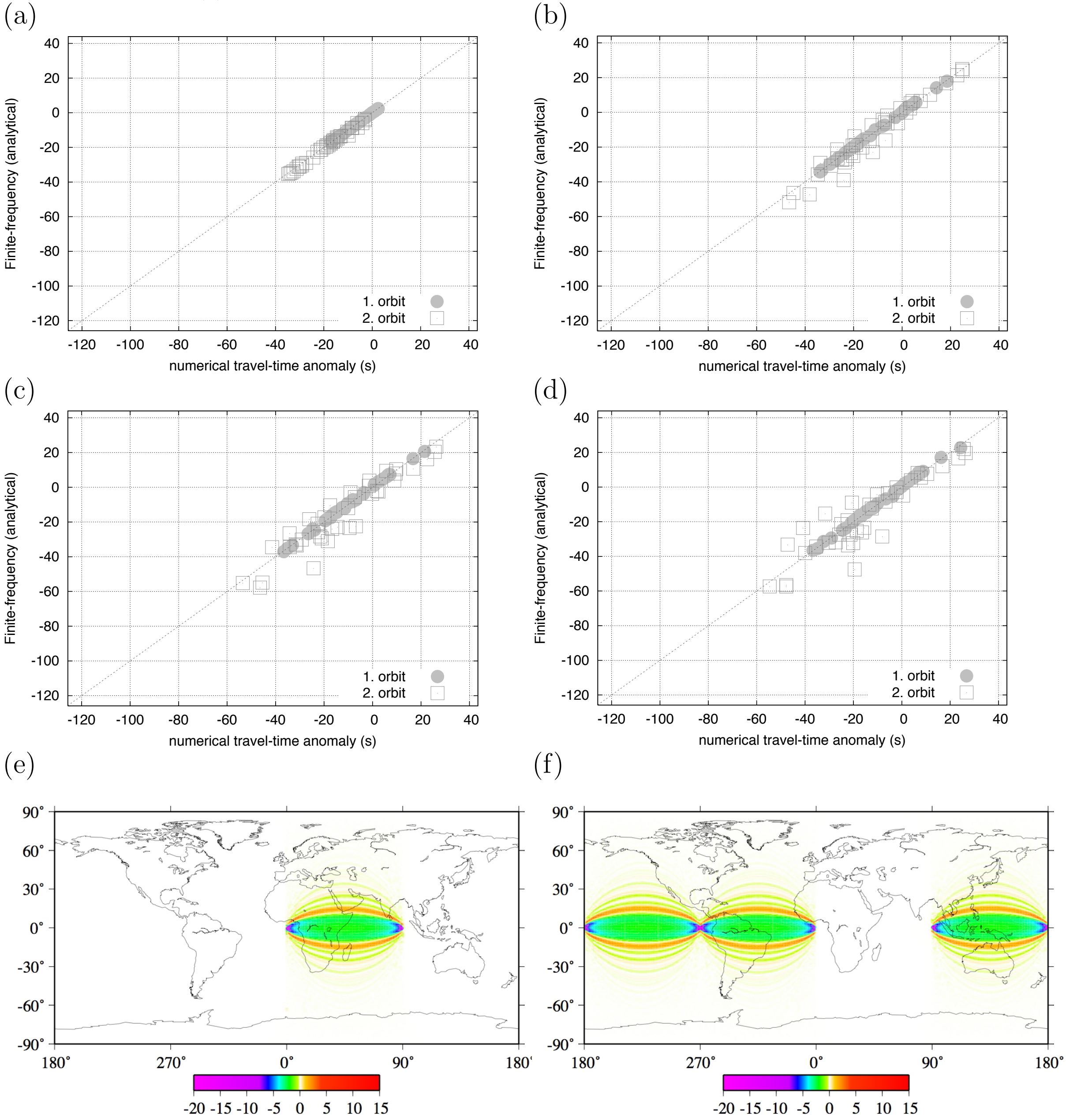

3.3.3 Multiple ray-path example

Ray-theoretical predictions are especially inaccurate in cases where multiple rays are found (Tape 2003). A reference case is chosen here for a source-station couple such that we obtain three ray paths, for the fourth orbit, which arrive at the same station location (source at equator 0° N / 0° W, station at about 25° N / 90° W). Rays are traced, and phase calculated in the 150 s Love wave phase-velocity map of Trampert & Woodhouse (1995), with a spherical harmonics expansion up to degree 10. The considered case is the only multi-pathing occurrence found for this phase-velocity map and maximum harmonic degree, among 38 investigated source-station couples with about 90° epicentral distance. If the model is filtered to lower harmonic degree, no multiple ray paths are found for the same source-station couples; at higher harmonic degrees, multi-pathing becomes increasingly frequent.

The ray-tracing algorithm calculates for each ray, denoted by $i = 1, 2, 3$, the corresponding phase anomaly $\delta\psi_i$, which is further divided by the angular frequency to obtain the corresponding travel-time anomaly δT_i for monochromatic waves with a period of about 150 seconds. To obtain the waveform, the amplitude anomaly for each ray is considered as well. The cumulative travelled epicentral distance from source to receiver is 630°. The ray-theoretical predicted values are applied to the monochromatic trace $\tilde{u}(\theta, \phi, t)$ obtained by filtering first the asymptotic waveform for the fourth orbit (see section 3.2.2). We further corrected the travel-time and amplitude of the monochromatic waveform for all three rays separately by the predicted travel-time anomaly δT_i and amplitude anomaly A_i to obtain three single waveforms

$$\tilde{u}_i(\theta, \phi, t) = A_i \cdot \tilde{u}(\theta, \phi, t + \delta T_i). \tag{3.48}$$

Finally, all three waveforms are summed up to obtain the resulting one

$$\tilde{u}_{\text{res}}(\theta, \phi, t) = \sum_i \tilde{u}_i(\theta, \phi, t). \tag{3.49}$$

Note that $\tilde{u}_{\text{res}}(\theta, \phi, t)$ is now valid for the heterogeneous model.

Eq. (3.49) is also implemented via the harmonic addition theorem, expressing the

Table 3.1: Example of multi-pathing, with three fourth-orbit rays joining source and receiver. The ground-truth value of travel-time anomaly, based on the traces computed numerically with the membrane-wave model, is compared with the ray-theoretical predictions and the resulting values by the harmonic addition theorem. Travel-times and amplitudes are based on the 150 s Love wave phase-velocity model of Trampert & Woodhouse (1995), filtered to include only harmonic degrees 10 and lower.

	travel-time anomaly	$[s]$
numerical	-97.1	▬
ray 1	-123.6	▬
ray 2	-134.4	▬
ray 3	- 90.2	▬
harmonic	-113.0	▬

	amplitude anomaly	
numerical	1.90	▬
ray 1	0.71	▬
ray 2	0.81	▬
ray 3	1.17	▬
harmonic	1.85	▬

sum of n harmonic waves as

$$\sum_{i=1}^{n} A_i \cos(\omega t + \delta\psi_i) = A \cos(\omega t + \delta\psi), \tag{3.50}$$

where

$$A^2 \equiv \sum_{i=1}^{n}\sum_{j=1}^{n} A_i A_j \cos(\delta\psi_i - \delta\psi_j), \tag{3.51}$$

$$\tan(\delta\psi) = \frac{\sum_{i=1}^{n} A_i \sin(\delta\psi_i)}{\sum_{i=1}^{n} A_i \cos(\delta\psi_i)}. \tag{3.52}$$

Hence, the resulting phase anomaly $\delta\psi$, resp. travel-time anomaly δT, and amplitude anomaly A of $\tilde{u}_{\mathrm{res}}(\theta,\phi,t)$ as defined by eq. (3.49) can be calculated directly from the single predictions $\delta\psi_i$ and A_i. We compare all values with the travel-time and amplitude anomaly obtained by the numerical algorithm in Table 3.1.

We observed that the resulting, asymptotic waveform, given by eq. (3.49), was shifted by about 17 seconds and exhibited a slightly bigger amplitude of about 5% with respect to the numerical, ground-truth trace. Note that the discrepancy of these observed anomalies to the analytical, harmonic values from Table 3.1 might be found in the finite bandwidth of the single traces $\tilde{u}_i(\theta,\phi,t)$ used for the summed waveforms of eq. (3.49),

Figure 3.6: Multiple ray paths for a reference case with the fourth orbit arrival in a heterogeneous background phase-velocity distribution (Trampert & Woodhouse 1995). All three rays solve the same ray-tracing equations from Woodhouse & Wong (1986) leading to different phase- and amplitude-anomaly predictions shown in Table 3.1.

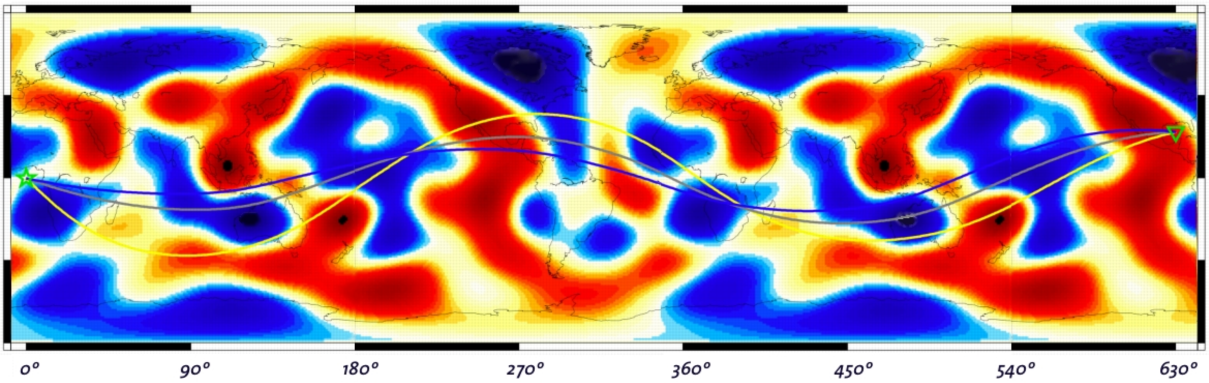

while the analytical values are valid only for monochromatic waves. Still, the travel-time anomaly of the resulting trace $\tilde{u}_{\mathrm{res}}(\theta, \phi, t)$ is closer to the numerical, ground-truth prediction than the single predictions for the second and third ray, but worse than the prediction of the first ray. It is therefore crucial to find all rays in order to properly account for the predicted anomalies.

Our study differs with respect to the work on synthetic seismograms of a more realistic case by Wang & Dahlen (1994, see fig. 21). We only consider the monochromatic (or very narrowly filtered) waveform for an analytical source, instead of an integration over a complete frequency range. Such an integration becomes more expensive as for each frequency the corresponding, ray-theoretical phase and amplitude anomalies must be found first. Additionally, we investigated especially a multiple ray-path example where Wang & Dahlen (1994) only consider single ray examples. A more systematic investigation of multi-pathing effects as done here could in principle be conducted with the membrane-wave model (Tanimoto 1990; Tape 2003; Peter *et al.* 2007).

3.4 Benchmark of different approaches to the inverse problem

To compare the performance of different tomographic methods in different scenarios, we construct a number of independent databases of ground-truth, numerically computed phase anomalies of 150 s Love waves. Some databases are derived from three "checkerboard" phase-velocity maps of different spatial frequency, another from the model of Trampert & Woodhouse (1996). We experiment with the amplitude of "input" anomalies, and with the realistic random noise added to the synthetics.

We invert each ground-truth dataset on a grid of approximately equal-area $3^\circ \times 3^\circ$-sized pixels. Linearized ray-theory and numerical sensitivity kernels (Peter *et al.*, 2007) are used independently to construct the corresponding matrices relating the phase-velocity perturbations to the data. In both cases, an iterative least-squares algorithm (Paige & Saunders 1982; implemented as in Boschi 2006) finds the phase-velocity solution to the inverse problem, where only roughness-damping is applied; no norm-damping is involved. We repeat the inversions with different roughness-damping coefficients (Boschi 2006; Boschi *et al.* 2006; Peter *et al.* 2007) and identify one preferred solution by analyzing the L-curve, where the misfit to the data is plotted versus the normalized model roughness (as defined by Boschi 2006). Collocating the resulting inversion maps for different damping values, we can visualize the animated solutions for each inversion scheme (http://www.seg2.ethz.ch/ dpeter/inversions.html). As explained by Boschi (2006) in his section 4 and fig. 3, if different formulations of the inverse problem are applied, equal numerical values of the damping parameter do not lead to equally regularized solutions from the different approaches. To identify equivalently regularized solutions from ray-theory and finite-frequency inversions, we use here the criterion of equal curvature on the respective L-curves (Peter *et al.* 2007).

In the following, we compare the preferred inversion solutions found from ray theory versus finite-frequency theory. If one accepts our definition of equivalently regularized solutions, differences in the solution maps can be ascribed solely to the effects of different theoretical descriptions of seismic wave propagation.

3.4.1 Data coverage

We employ the same source-station couples as in the database of Ekström *et al.* (1997), updated as described by Boschi & Ekström (2002), for minor-arc Love waves at 150 s period. For each source-station couple, we construct a synthetic measurement by cross-correlation between the trace obtained for a homogeneous background model, and the trace calculated for a corresponding laterally heterogeneous input model. The number of synthetic measurements ($\sim 10^4$) is therefore equal to the number of observations in the real dataset at this period. Figure 3.7 shows the great-circle rays for all measurements with the chosen source-station distribution. The data coverage defined by the number of rays passing through each single pixel of the inversion grid coincides with that of Peter *et al.* (2007, fig. 12). Regions with the highest number of ray-counts are distributed over Asia and North America. The Southern Hemisphere in general has a relatively poor data coverage.

Figure 3.7: The synthetic datasets use the global distribution of sources (red stars) and stations (green triangles) taken from Ekström *et al.* (1997) for Love waves at 150 second periods. They include 16′624 measurements. For each measurement, the great-circle ray is plotted between the corresponding source and station.

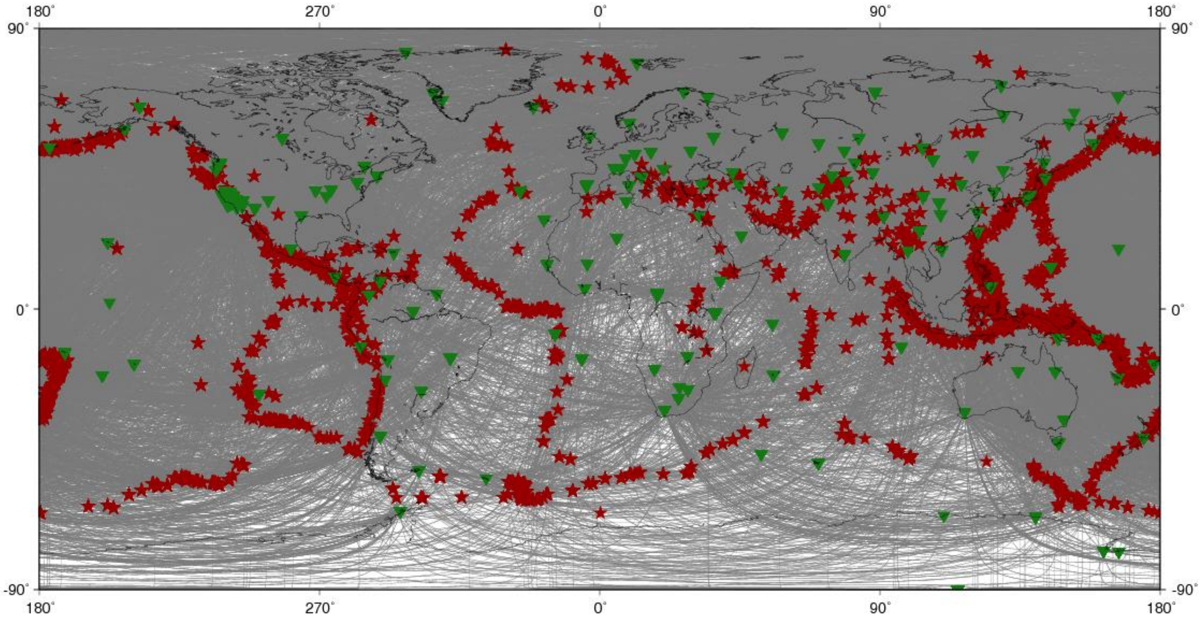

3.4.2 Scalelength test

Ray theory is a high-frequency approximation. In practice, this leads to the condition that the wavelength under consideration should be small compared to the scalelength of heterogeneities it travels through. In order to illustrate the effect of this assumption upon the performance of the inverse method, we can either (i) change the size of the perturbations in the input models or (ii) consider smaller wavelengths/wave periods.

Figure 3.8 shows the results of experiment (i), comparing the inversions of synthetic data computed in single-harmonic "checkerboard" models of different spatial frequency (degrees). The synthetic datasets for each input model used Love waves at 150 seconds period to obtain the waveform for the homogeneous and heterogeneous case. Ray-theoretically derived solutions start differing from finite-frequency solutions for the higher degree input models. The lengthscale of the perturbations for the chosen input models vary in a range of $\sim 2'000 - 4'000$ km, i.e. about three to six times the wavelength under consideration. Figure 3.9 follows the idea (ii) and changes the wave period down to 100 seconds in order to derive the synthetic datasets for the two higher degree checkerboards of the previous example. In this case, at the highest degree model, the lengthscale of perturbations is about four times the wavelength. Especially for regions with good data coverage, the inversions can retrieve the input model fairly accurately.

From a comparison of Figure 3.8a with 3.8b or 3.8c, or of Figure 3.9a with 3.9b, we infer that finite-frequency methods, applied to minor-arc phase-velocity data at the periods under consideration, perform significantly better at smaller scalelengths of heterogeneity than ray-theoretical methods. Differences between ray-theoretical and finite-frequency solutions are small for low-degree "input" models (< 10: Figure 3.8a), but start to become significant for higher degrees (≥ 13: Figure 3.8b, 3.8c, 3.9b). Considering shorter wavelengths, this effect shifts to higher spherical harmonic degrees (compare Figure 3.8b with 3.9a). The finite-frequency solutions clearly retrieve the input structures with higher accuracy. Differences are most prominent in regions with lower data coverage (oceans, Southern Hemisphere), where ray theory is systematically less accurate. As a general rule, in this ideal case without any noise in the data, finite-frequency solutions achieve a much better datafit than ray-theoretical ones.

Figure 3.8: Inversions for Love waves at 150 s period and input models of 2% perturbations and different scalelengths of heterogeneities: (a) checkerboard defined as a single spherical harmonic of degree $l = 9$ and order $m = 5$, (b) checkerboard with $l = 13$ and $m = 7$ and (c) checkerboard with $l = 20$ and $m = 10$. The input models are shown in the left column, solutions of the ray-theoretical inversions in the middle and finite-frequency inversions on the right column.

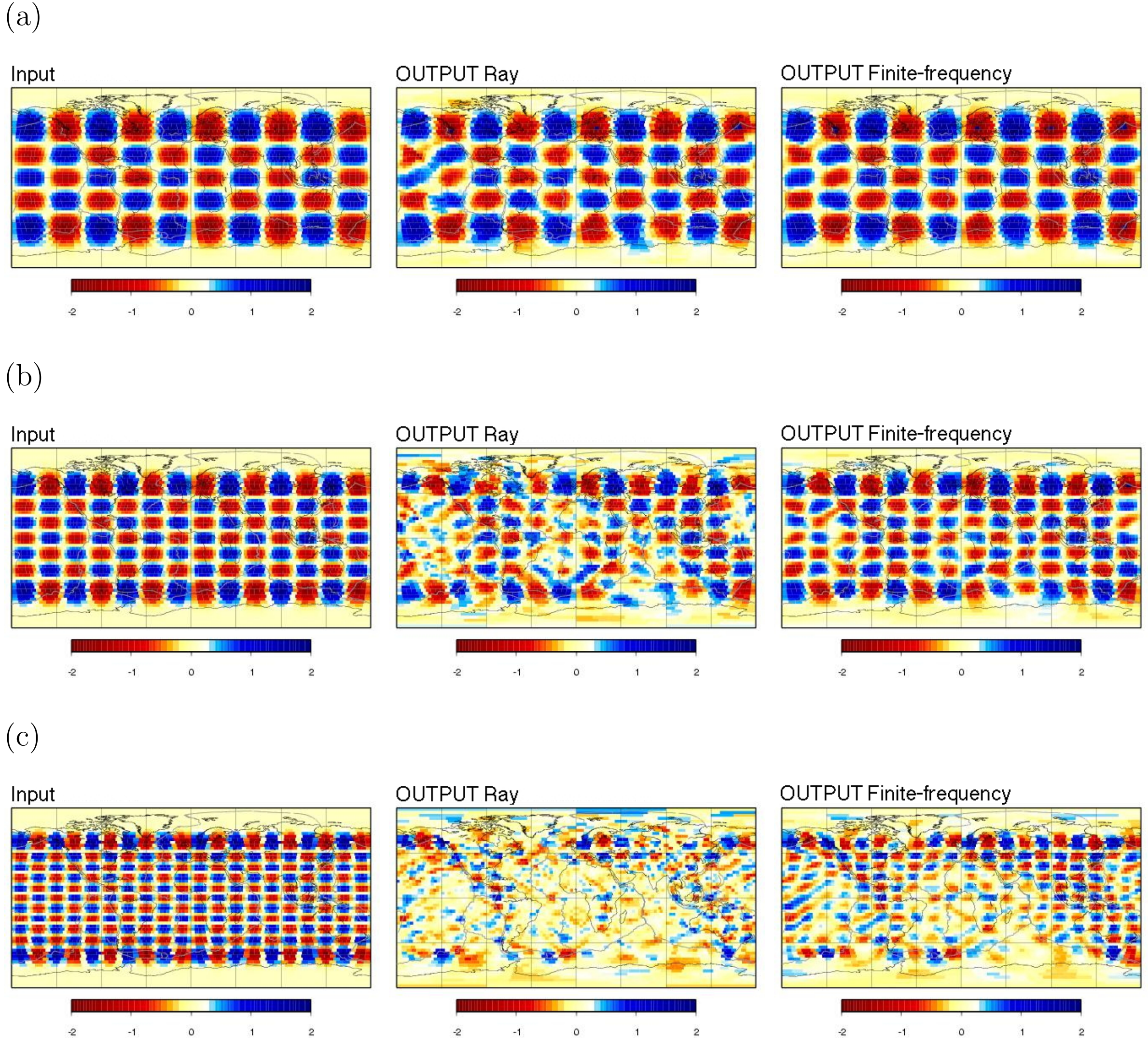
(a)
Input
OUTPUT Ray
OUTPUT Finite-frequency
-2
-1
0
1
2
(b)
Input
OUTPUT Ray
OUTPUT Finite-frequency
-2
-1
0
1
2
(c)
Input
OUTPUT Ray
OUTPUT Finite-frequency
-2
-1
0
1
2

Figure 3.9: Inversions for Love waves at 100 s period and input models of 2% perturbations and different scalelengths of heterogeneities: (a) checkerboard with spherical harmonic degree $l = 13$ and $m = 7$ and (b) checkerboard with $l = 20$ and $m = 10$. The input models are shown in the left column, solutions of the ray-theoretical inversions in the middle and finite-frequency inversions on the right column.

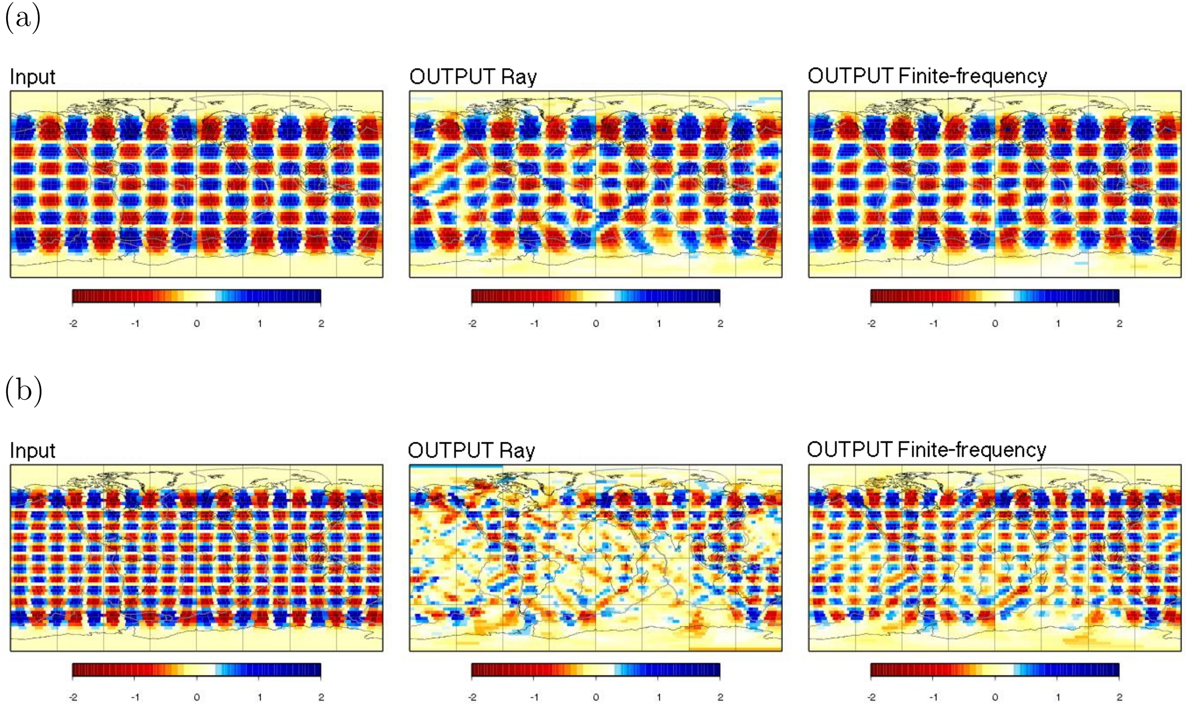
(a)
Input
OUTPUT Ray
OUTPUT Finite-frequency
-2
-1
0
1
2
(b)
Input
OUTPUT Ray
OUTPUT Finite-frequency
-2
-1
0
1
2

3.4.3 Noise test

The goal here is to investigate the effect of measurement errors on the tomographic images. Adding realistic noise to a synthetic database is difficult, because there can be sources of systematic errors, which are not known *a priori*, in the real databases. Ekström *et al.* (1997) estimate the quality of their observations by comparing measurements from pairs of nearby source-station couples. This way, they are able to derive a Gaussian distribution of possible errors of the dataset. The standard deviation of this Gaussian distribution is then an estimate of the accuracy of the measurement technique. We add Gaussian random noise to the synthetic database. The standard deviation has the same size as that found by Ekström *et al.* (1997) as described above, for the same wave period. This is about 5.7 seconds in terms of travel-time shift. The error in the synthetic dataset is also checked by the same searching algorithm of pairs of source-station couples that are within a 3° radius from source and receiver location.

We show in Figure 3.10 the results of inverting the ground-truth database constructed from the degree 13 (Figure3.10a) and degree 20 (Figure 3.10b) checkerboards (left panels), using the ray-theory (middle panels) and finite-frequency-theory based (right panels) inverse algorithms. All solutions employ a slightly higher roughness damping. In contrast to Figures 3.8b and 3.8c, the statistical noise degrades the solutions and diminishes the differences between the two approaches in question. This is in agreement with what suggested Sieminski *et al.* (2004).

Still, even in the presence of noise, our solutions from finite-frequency inversions are somewhat closer to input models than those found from ray-theory ones. These results are somewhat different to the ones obtained for global-scale inversions by Zhou *et al.* (2005, see fig. 19). There are, however, a few important differences between their study and ours: (i) Unlike Zhou *et al.* (2005), we construct the synthetic database by means of a non-linearized numerical method, so that the accuracy of the synthetics is not hindered by the same approximations used in the inversion, as is the case in classical checkerboard tests conducted by Zhou *et al.* (2005). (ii) While Zhou *et al.* (2005) adds Gaussian-distributed, random noise with an RMS-error of about 50% of the ‘structural signal’, we apply the same kind of statistical noise but with the same standard deviation as found in the real dataset of Ekström *et al.* (1997). The amplitude of noise is therefore different. Additionally, the effects of noise strongly depend on the data coverage of the dataset, which is different as well between the two studies. (iii) Zhou *et al.* (2005) calculates

Figure 3.10: Using statistical noise in the synthetic dataset, solutions for Love waves at 150 s period and an input model of 2% perturbations are shown: (a) with a checkerboard with $l = 13$ and $m = 7$ and (b) with a checkerboard with $l = 20$ and $m = 10$. The input models are shown in the left column, solutions of the ray-theoretical inversions in the middle and finite-frequency inversions on the right column.

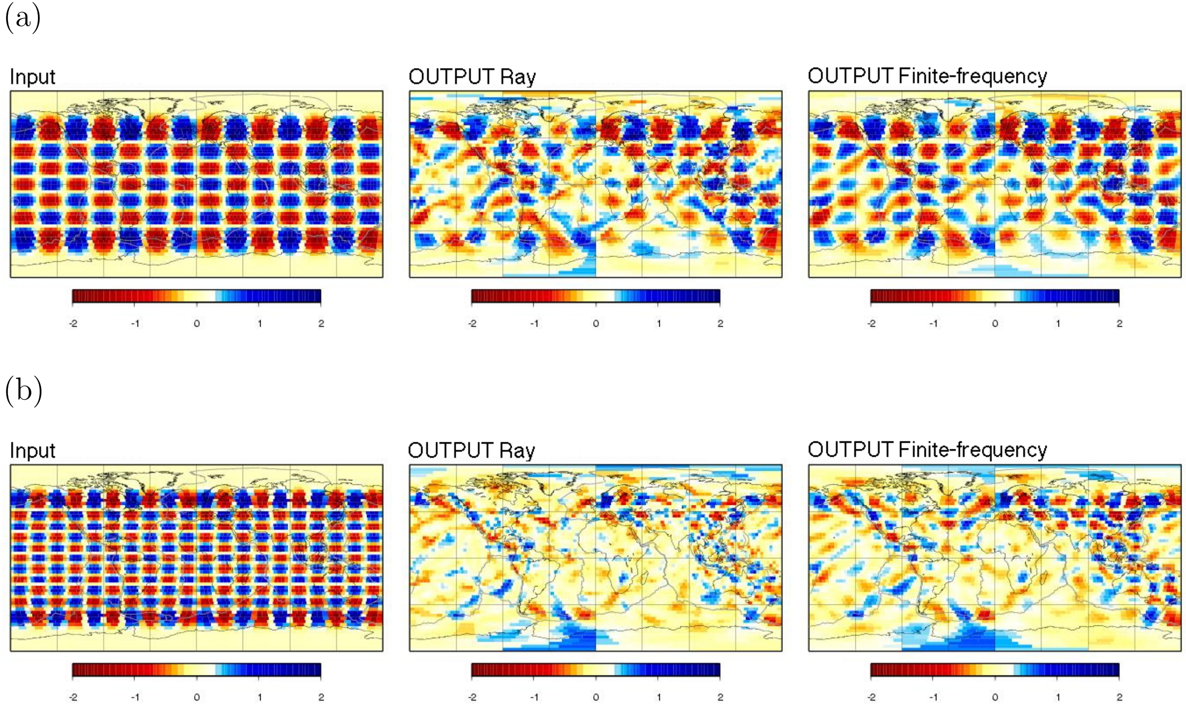
(a)
Input
OUTPUT Ray
OUTPUT Finite-frequency
-2
-1
0
1
2
-2
-1
0
1
2
-2
-1
0
1
2
(b)
Input
OUTPUT Ray
OUTPUT Finite-frequency
-2
-1
0
1
2
-2
-1
0
1
2
-2
-1
0
1
2

analytical sensitivity kernels based upon a far-field approximation, while our kernels are computed strictly numerically. We also use a different coarseness of the inverse grid, which leads to different resolution of the kernels actually used by the inverse algorithm. As we use a slightly finer parameterization, our kernels will be represented in more detail thus exhibiting a bigger difference to rays, which itself can be assumed to lead to bigger differences in the inverse solutions found between the two theories.

3.4.4 Amplitude test

Both ray theory and single-scattering finite-frequency theory are linearized theories, whose performance is contingent on the extent and amplitude of perturbations with respect to a reference model, i.e. they fail when applied to (very) rough media. We next explore the specific nonlinear effects of the amplitude of Earth structure heterogeneities in an example case with amplitude perturbations as high as ±10%. The input model pattern is a checkerboard, coinciding with the spherical harmonic function of degree 9 and order 5 as in the previous section 3.4.2. The synthetic database is then constructed for Love waves at 150 seconds period without any statistical noise.

The solution images of the inversion of the corresponding synthetic dataset are shown in Figure 3.11a. Comparing them with the solutions plotted in Figure 3.8a, we see that both theories suffer from their inherent linearization. The power spectra of the ray-theoretical solution in Figure 3.11b and of the finite-frequency solution in 3.11c reveal both the initial the power spectrum of the 10% checkerboard input model with a strong peak at spherical harmonic degree 9, the finite-frequency solution achieving a slightly higher peak. Both power spectra show further aliasing of energy towards surrounding harmonic degrees. Nonlinear effects are not only degrading the performance of both inverse methods, they also tend to affect the stability of the solutions, so that the inversions have to be damped more strongly than in the experiments described above. In order to overcome these limitations, a nonlinear solution could be found iteratively, using the solution of a previous inversion as a new starting model to reconstruct the matrices for a new inversion. We tested this approach in the finite-frequency case, computing all sensitivity kernels again in the new starting model (Peter *et al.* 2007). Even after three iterations, the solution (not shown here) did not improve significantly. Starting each iteration with a highly damped model (and, consequently, a relatively poor datafit) increases the total number of iterations needed to find a sufficiently good result. On the other hand, starting with a rougher model like the output models of Figure 3.11, the solution is perturbed very little at each iteration. This suggests that the inverse scheme might be trapped at a local minimum of the misfit function.

Figure 3.11: Influence of large amplitude of heterogeneities. Solutions are shown for Love waves at 150 s period and an input model of (a) 10% perturbations with a checkerboard with $l = 9$ and $m = 5$. On the left, the input model is shown, while in the middle and on the right side the ray-theoretical and finite-frequency solutions, respectively, are plotted. The power spectrum up to spherical harmonic degree 25 is shown of the ray-theoretical solution image in (b) as red bars, the corresponding one of the finite-frequency solution image in (c), both plotted against the initial power spectrum of the input model (black box).

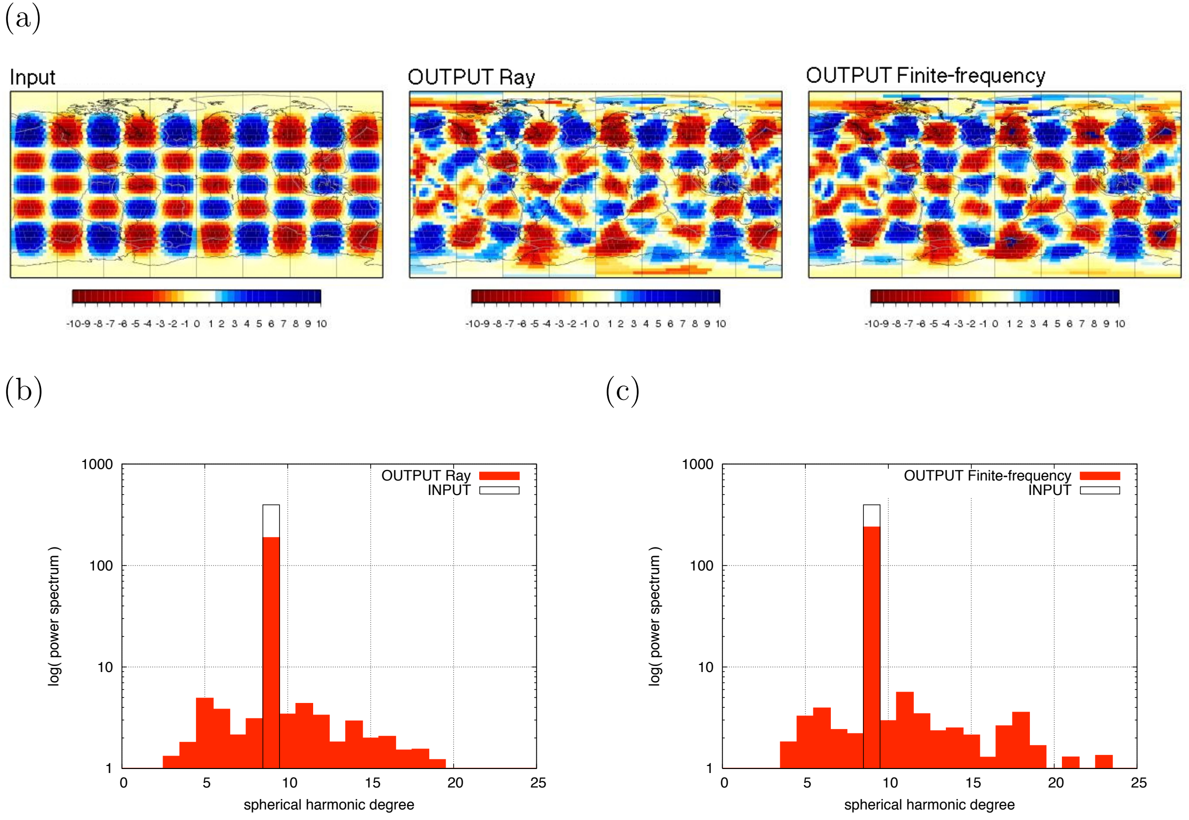

3.4.5 Realistic input model test

While checkerboard maps like those of Figures 3.8 through 3.11 have an impulsive power spectrum, with all energy at only one degree, realistic phase-velocity distributions for surface waves at intermediate to long periods exhibit in general a red spectrum, i.e. with most energy at lower spherical degrees (< 8). Either because tomography cannot resolve it, or because the Earth's upper mantle is, indeed, a smoothly heterogeneous medium, the high-degree portion of the spectrum is usually much weaker. We choose as starting model the phase-velocity map originally derived from Trampert & Woodhouse (1996) for Love waves at 150 s period. Note that this phase-velocity distribution model represents a solution to a different number of observations with a different source-station setup and a different parameterization of the inverse algorithm. We construct $\sim 10^4$ synthetic measurements with the same source-station distribution from Ekström *et al.* (1997) as in the previous tests to obtain the synthetic database for the benchmark exercise conducted here. No statistical noise is added to this synthetic database.

In Figure 3.12a, the preferred solutions of the ray-theoretical and finite-frequency inversion methods are shown. The power spectra of both solutions are plotted against the power spectrum of the input model in Figure 3.12b and 3.12c; the power spectrum of the ray-theoretical inversion result is slightly overpredicting the lowest harmonic degrees while losing energy at higher degrees (> 8). The power spectrum of the finite-frequency solution is clearly more consistent with the input one, both at lower and at higher degrees, while the loss of resolution with increasing harmonic degree is slower than in the ray-theory case.

Note that both power spectra are strongly affected by the damping value chosen for the corresponding inversion solution. Less damping favors more energy content in the power spectrum. The strength of damping in these comparisons is therefore crucial. As ray and finite-frequency theory lead to a different sparseness and matrix representation in the inverse scheme, solution maps need different damping values that account for this fact. We compare solutions based on a L-curve analysis with the criterion of equal curvature values (Boschi 2006; Peter *et al.* 2007). As a result, Figure 3.12 shows a ray-theoretical solution with a slightly larger damping coefficient than the compared finite-frequency solution. In general, we see that the finite-frequency solutions retrieve the initial power spectrum better than ray-theoretical solutions.

In summary, the results of our benchmark indicate that finite-frequency inverse methods should recover the phase-velocity distribution and power spectrum of the real Earth better than ray-theory ones, particularly at high harmonic degrees. Peter *et al.* (2007) inverted the phase-anomaly observations from the dataset of Ekström *et al.* (1997) for Love waves at 150 s period. Ray-theoretical and finite-frequency solutions were almost

Figure 3.12: Realistic input model TW96 solved for Love waves at 150 s period. (a) The input model is shown on the left, the ray-theoretical inversion in the middle and the finite-frequency inversion solution on the right. The corresponding power spectrum up to spherical harmonic degree 25 of (b) the ray-theoretical solution image (red bars) and (c) the finite-frequency solution image (red bars) are plotted against the initial power spectrum of the input model (black boxes).

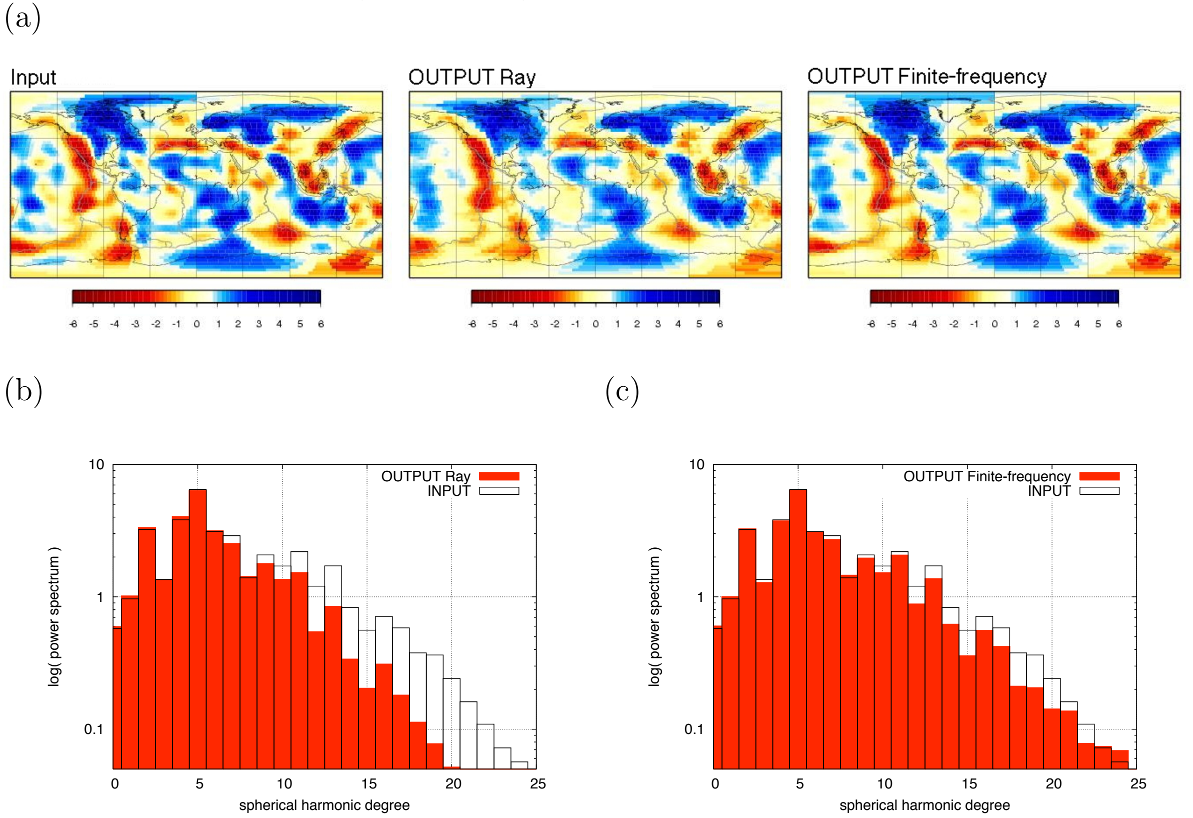

identical. In their fig. 17, the power spectrum for the finite-frequency solution reveals a slightly higher amplitude at degrees > 8 as for the ray-theoretical solution. Our current results imply that this difference, although small in amplitude, reflects an improvement in the tomographic resolution of small-scale heterogeneity present in the Earth.

3.5 Conclusions

Using the asymptotic approach, we derived an analytical description of the propagation of elastic waves on a zero-thickness membrane in terms of traveling waves, consistent with the more general treatments of Gilbert (1976), Dahlen & Tromp (1998), and Ferreira (2005). We used this formulation of ray theory on a membrane in a benchmark against the forward predictions of finite-frequency kernels (analytical and numerical: see Peter *et al.* 2007), and a ground-truth database of numerical, membrane-wave synthetics. Our work extends the investigations made for 3-D sensitivity kernels within 3-D cartesian boxes (Baig *et al.* 2003; Baig & Dahlen 2004; Dahlen 2004; Yang & Hung 2005) to a 2-D spherical geometry. We further employed finite-frequency sensitivity kernels for higher orbits. While predictions made by finite-frequency theory for first orbit arrivals are more precise than those of exact ray theory, we found that finite-frequency sensitivity kernels can not predict phase anomalies accurately enough for higher orbits and even weakly heterogeneous phase-velocity models (spherical degree expansions > 4).

We also benchmarked the tomographic inverse method based on ray theory, against the finite-frequency tomographic algorithm of Peter *et al.* (2007), based on the adjoint method. Both approaches were applied independently to invert the same synthetic database of phase-anomaly measurements based on a realistic source/receiver distribution (Ekström *et al.* 1997) for global phase-velocity perturbations. The results of the latter experiment, limited to first orbit data, indicate that finite-frequency theory performs significantly better than linearized ray theory. In regions with poor data coverage, noise in the data can strongly affect the tomographic solution. This complicates comparisons between ray and finite-frequency theory based on real (noisy) phase-anomaly measurements. Nevertheless, one can expect that, in a regime of very good data coverage and quality, accounting for single scattering of intermediate- to long-period surface waves will improve significantly the resolution of tomographic imaging.

Acknowledgments

We thank Domenico Giardini for his constant support and Jeannot Trampert for making his phase-velocity models available to us. Thanks also to Göran Ekström for providing his dispersion database to us and Carl Tape for helpful comments. We gratefully acknowledge support from the European Commission's Human Resources and Mobility Programme Marie Curie Research Training Network SPICE Contract No. MRTN-CT-2003-504267. Some figures were generated using the generic mapping tools (GMT) (Wessel & Smith 1991).

Bibliography

[1] Baig, A.M., F.A. Dahlen and S. H. Hung, 2003. Traveltimes of waves in three-dimensional random media, *Geophysical Journal International*, *153*: p. 467-482.

[2] Baig, A.M. and F.A. Dahlen, 2004. Statistics of traveltimes and amplitudes in random media, *Geophysical Journal International*, *158*: p. 187-210.

[3] Boschi, L., 2003. Measures of resolution in global body wave tomography, *Geophysical Research Letters*, *30*: p. 1978, doi:10.1029/2003GL018222.

[4] Boschi, L., 2006. Global multiresolution models of surface wave propagation: comparing equivalently regularized Born and ray theoretical solutions, *Geophysical Journal International*, *167*: p. 238-252.

[5] Boschi, L. and G. Ekström, 2002. New images of the Earth's upper mantle from measurements of surface wave phase velocity anomalies, *Journal of Geophysical Research-Solid Earth*, *107*: p. 10.1029/2000JB000059.

[6] Boschi, L., T. W. Becker, G. Soldati and A. M. Dziewonski, 2006. On the relevance of Born theory in global seismic tomography, *Geophysical Research Letters*, *33*: p. L06302, doi:10.1029/2005GL025063.

[7] Boschi, L. and J.H. Woodhouse, 2006. Surface wave ray tracing and azimuthal anisotropy: a generalized spherical harmonic approach, *Geophys. J. Int., , 164*: p. 569-578.

[8] Boschi, L., Ampuero, J.-P., Peter, D., Mai, P.M., Soldati, G. and D. Giardini, 2007. Petascale computing and resolution in global seismic tomography, *Physics of the Earth and Planetary Interiors*, *163*: p. 245-250.

[9] Dahlen, F.A. and J. Tromp, 1998. Theoretical global seismology, *Princeton University Press.*

[10] Dahlen, F.A., S. H. Hung and G. Nolet, 2000. Frechet kernels for finite-frequency traveltimes - I. Theory, *Geophysical Journal International*, *141*: p. 157-174.

[11] Dahlen, F.A., 2004. Resolution limit of traveltime tomography, *Geophys. J. Int.,* , *157*: p. 315-331.

[12] Ekström, G., J. Tromp and E. W. F. Larson, 1997. Measurements and global models of surface wave propagation, *J. geophys. Res.,* **102**, 8137–8157.

[13] Ferreira, A.M.G., 2005. *Seismic Surface Waves in the Laterally Heterogeneous Earth*, DPhil thesis, University of Oxford, U.K.

[14] Gilbert, F., 1976. The representation of seismic displacements in terms of travelling waves, *Geophys. J. R. astr. Soc.,* , *44*: p. 275-280.

[15] Laske, G., 1995. Global observation of off-great-circle propagation of long-period surface waves *Geophys. J. Int.,* , *123*: p. 245-259.

[16] Laske, G. and G. Masters, 1996. Constraints on global phase velocity maps from long-period polarization data, *Journal of Geophysical Research*, *101*: p. 16059-16075.

[17] Lévêque, J. J., L. Rivera and G. Wittlinger, 1993. On the Use of the Checkerboard Test to Assess the Resolution of Tomographic Inversions, *Geophysical Journal International*, *115*: p. 313-318.

[18] Li, X. D. and T. Tanimoto, 1993. Wave-Forms of Long-Period Body Waves in a Slightly Aspherical Earth Model, *Geophysical Journal International*, *112*: p. 92-102.

[19] Li, X. D. and B. Romanowicz, 1995. Comparison of Global Wave-Form Inversions with and without Considering Cross-Branch Modal Coupling, *Geophysical Journal International*, *121*: p. 695-709.

[20] Nelder, J. A. and R. Mead, 1965. A simplex-method for function minimization, *Computer Journal*, *7*: p. 308-313.

[21] Paige, C.C. and M. A. Saunders, 1982. LSQR - an Algorithm for Sparse Linear-Equations and Sparse Least-Squares, *Acm Transactions on Mathematical Software*, *1*: p. 43-71.

[22] Peter, D., C. Tape, L. Boschi and J. H. Woodhouse, 2007. Surface wave tomography: global membrane waves and adjoint methods, *Geophys. J. Int.,* , *171*: p. 1098-1117.

[23] Press, W. H., S. A. Teukolsky, W. T. Vetterling and B. P. Flannery, 1992. *Numerical Recipes in FORTRAN: the Art of Scientific Computing*, 2nd ed. xxvi, 963, Cambridge University Press, Cambridge [England]; New York, N.Y., U.S.A.

[24] Qin, Y., Y. Capdeville, V. Maupin and J.-P. Montagner, 2006. Synthetic data set to benchmark global tomographic methods, *EOS Trans AGU*, *87*: p. 512.

[25] Ritzwoller, M. H., N.M. Shapiro, M.P. Barmin and A.L. Levshin, 2002. Global surface wave diffraction tomography, *Journal of Geophysical Research*, *107*: p. 2335, doi:10.1029/2002JB001777

[26] Segel, L. A., 1966. Importance of Asymptotic Analysis in Applied Mathematics, *American Mathematical Monthly*, *73*(1): p. 7-14.

[27] Sieminski, A., J.J. Lévêque and E. Debayle, 2004. Can finite-frequency effects be accounted for in ray theory surface wave tomography?, *Geophys. Res. Lett.,* , *31*, L24614.

[28] Spetzler, J. and R. Snieder, 2001. The effect of small-scale heterogeneity on the arrival time of waves, *Geophysical Journal International*, *145*: p. 786-796.

[29] Spetzler, J., J. Trampert and R. Snieder, 2002. The effect of scattering in surface wave tomography, *Geophysical Journal International*, *149*: p. 755-767.

[30] Tanimoto, T., 1990. Modeling Curved Surface-Wave Paths - Membrane-Surface Wave Synthetics, *Geophysical Journal International*, *102*: p. 89-100.

[31] Tape, C. H., 2003. *Waves on a Spherical Membrane*, M.Sc. thesis, University of Oxford, U.K.

[32] Tape, C., Q. Liu and J. Tromp, 2007. Finite-frequency tomography using adjoint methods. Methodology and examples using membrane surface waves, *Geophysical Journal International*, *168*: p. 1105-1129.

[33] Trampert, J. and J. H. Woodhouse,1995. Global phase velocity maps of Love and Rayleigh waves between 40 and 150 seconds, *Geophys. J. Int.,* , *122*: p. 675-690.

[34] Trampert, J. and J. H. Woodhouse, 1996. High resolution global phase velocity distribution, *Geophys. Res. Lett., , 23*: p. 21-24.

[35] Trampert, J. and J. H. Woodhouse, 2001. Assessment of global phase velocity models, *Geophys. J. Int., , 144*: p. 165-174.

[36] Tromp, J., C. Tape and Q. Y. Liu, 2005. Seismic tomography, adjoint methods, time reversal and banana-doughnut kernels, *Geophysical Journal International*, *160*: p. 195-216.

[37] van Heijst, H. J. and J. H. Woodhouse, 1999. Global high-resolution phase velocity distributions of overtone and fundamental-mode surface waves determined by mode branch stripping, *Geophys. J. Int.*, *137*: p. 601-620.

[38] Wang, Z. and F. A. Dahlen, 1994. JWKB surface-wave seismograms on a laterally heterogeneous Earth, *Geophys. J. Int.*, *119*: p. 381-401.

[39] Wessel, P. and W. H. F. Smith, 1991. Free software helps map and display data, *EOS, Transactions American Geophysical Union*, *72*(41): p. 441.

[40] Woodhouse, J. H. and T. P. Girnius, 1982. Surface-Waves and Free Oscillations in a Regionalized Earth Model, *Geophysical Journal of the Royal Astronomical Society*, *68*: p. 653-673.

[41] Woodhouse, J. H. and Y. K. Wong, 1986. Amplitude, phase and path anomalies of mantle waves, *Geophys. J. R. astr. Soc., , 87*: p. 753-773.

[42] Yang, H. Y. and S. H. Hung, 2005. Validation of ray and wave theoretical travel times in heterogeneous random media, *Geophysical Research Letters*, *32*: p. L20302.

[43] Yoshizawa, K. and B. L. N. Kennett, 2005. Sensitivity kernels for finite-frequency surface waves, *submitted to Geophys. J. Int.*, *162*: p. 910-926.

[44] Zhou, Y., F. A. Dahlen and G. Nolet, 2004. Three-dimensional sensitivity kernels for surface wave observables, *Geophysical Journal International*, *158*: p. 142-168.

[45] Zhou, Y., F. A. Dahlen, G. Nolet and G. Laske, 2005. Finite-frequency effects in global surface-wave tomography, *Geophysical Journal International*, *163*: p. 1087-1111.

4 Surface-wave tomography: finite-frequency shear-velocity inversions for the European-Mediterranean region

---

4.1 Introduction

4.2 Data

4.3 Method

4.4 Results

4.5 Discussion

4.6 Conclusions

This chapter will be submitted to *Geophys. Res. Lett.,* co-authors were Lapo Boschi, Frédéric Deschamps, Bill Fry, Göran Ekström and Domenico Giardini. Footnote comments are provided only for this thesis version.

Summary

Multiple-resolution inversions of combined global and regional seismic data can improve regional tomographic models. We invert a high-quality, global phase-anomaly database of intermediate- to long-period Rayleigh waves, with increased coverage in the European-Mediterranean region, on a global scale with a higher resolution parameterization in the region of interest. We first compare phase-velocity inversions based on ray and finite-frequency theory and derive for each a corresponding set of local phase-velocity dispersion curves (one per model pixel) between 35 s to 300 s period. In order to investigate the effects of those two different theoretical approaches on the three-dimensional problem of imaging upper-mantle structure, we next invert each dispersion curve for radial shear-velocity profiles. The combination of a gradient-descent method and a random-Monte-Carlo model search provides an estimated shear-velocity model with associated uncertainties for depths between 40 km to 400 km. Comparisons with independent studies suggest that finite-frequency tomography reveals seismic structures in more detail than ray theory, but differences between the two models are small, compared to model uncertainty.

4.1 Introduction

In view of current plans to build a European seismological reference model (Ritzwoller *et al.* 2006), a new enriched high-quality surface-wave dataset was assembled, achieving unprecedentedly dense coverage of the region (Fry *et al.* 2008). The dataset combines global and regional observations, which helps to further constrain regional seismic models (see e.g. Shapiro & Ritzwoller 2002). Tectonics in Europe and in the Mediterranean region are governed by a complex interaction of the African, Eurasian and Arabian plates, comprehensively investigated in several tomographic studies (Spakman *et al.* 1993; Wortel & Spakman 2001; Piromallo & Morelli 2003; Boschi *et al.* 2004; Marone *et al.* 2004; Fry 2007; Schmid *et al.* 2008). Recent phase-velocity models of Europe and the Mediterranean region, found using analytical finite-frequency sensitivity kernels, show some main discrepancies to ray-theoretical ones, especially between the Southern Apennines and the Hellenic Arc (Fry *et al.* 2008).

It is unclear how such differences in phase-velocity distributions reflect differences in the underlying seismic structures[1]. Inversions for one-dimensional seismic depth profiles are highly nonlinear, and their solutions are not unique (Knopoff 1972). An exploration of the solution space more thorough than those afforded by linearized inversions becomes therefore necessary, to identify a most likely seismic profile and estimate its uniqueness. Focusing on the well sampled European-Mediterranean region (Fry *et al.* 2008), we will use Rayleigh-wave phase-velocity maps derived either by ray or numerical finite-frequency theory (Peter *et al.* 2007) to build a new set of dispersion curves which, in a second step, are inverted for radial V_s profiles. We will then compare the corresponding three-dimensional shear-velocity models, and draw conclusions on the different methods' performance, based on our understanding of the region's tectonics.

4.2 Data

The global Harvard database from Ekström *et al.* (1997), updated by Boschi & Ekström (2002), was further expanded by Fry (2007) to include also regional surface-wave data. This new high-quality dataset has a particularly good data coverage[2] over Europe and the Mediterranean region (Fry *et al.* 2008), providing measurements of both Love and Rayleigh wave phase-anomalies at periods between 35 s and 300 s. In this study, we invert measurements of Rayleigh waves[3] at all given periods and epicentral distances, and for both minor and major arcs.

---

[1] Differences in dispersion curves could map directly into the three-dimensional models as the dispersion curves are to first-order a linear combination of the underlying three-dimensional velocity structure (Trampert & Woodhouse 2001).

[2] It was collected using additional data from permanent stations of the SDSNet (Baer *et al.* 2000) and GRSN (Stammler & Hanka 2002), as well as temporary data stations from recent projects, like MIDSEA (van der Lee *et al.* 2001) and TomoCH (Fry 2007). Epicentral distances range between 15° and 165° for minor-arc measurements. For the longest periods at 150 - 300 s, additional major-arc measurements are also available.

[3] Rayleigh waves are mostly sensitive to vertically polarized shear-velocity (Boschi & Ekström 2002). Through the neglect of anisotropy, this will limit the number of solution parameters, confining the model-space search, and making the approach of inverting densely sampled dispersion curves for shear-velocity profiles in the European-Mediterranean region computationally feasible.

4.3 Method

We invert for local phase velocities with a global multiple-resolution parameterization, where Europe and the Mediterranean region are parameterized with blocks of approximately equal size of 1° x 1°, everywhere else by 3° x 3° blocks[4] (Boschi 2006). At each period from 35 s to 300 s, we use a least-squares algorithm (Paige & Saunders 1982) to find a phase-velocity map derived by either ray- or finite-frequency theory. For the later, we computed sensitivity kernels entirely numerically as described by Peter *et al.* (2007). Our choice of solution is based on an analysis of the L-curves, comparing for each theory the inversion solutions corresponding to the same curvature on the L-curve (Peter *et al.* 2007).

Dispersion curves derived from these phase-velocity maps are assembled for each inversion pixel within Europe and the Mediterranean region (900 locations total). We find for each the corresponding shear-velocities in six distinct layers (40 - 60 km, 60 - 100 km, 100 - 150 km, 150 - 220 km, 220 - 310 km and 310 - 400 km). We use Knopoff's method[5] (Knopoff 1964; Schwab & Knopoff 1970) to calculate a synthetic dispersion curve for each seismic profile generated by our search algorithm, starting with a seismic profile combining PREM (Dziewonski & Anderson 1981) upper mantle and crustal seismic velocities from Crust-2.0 (Bassin *et al.* 2000) together with the more accurate estimates of ocean and Moho depths of the European crustal model EuCrust-07 (Tesauro *et al.* 2008) (averaged over each 1° x 1° pixel). We iteratively improve each starting model by a gradient-descent inversion (Tarantola 2005) for V_s averaged over the six distinct layers. In a Monte-Carlo approach, we next generate $\sim 10^5$ radial profiles by randomly perturbing at each layer the values of V_s up to 10%, while keeping density and P-velocity fixed (Deschamps *et al.* 2008).

Our cost function χ^2, accounting for the observational error σ_j (estimated by Ekström *et al.* 1997) at each period T_j and for the difference between "observed" $c_{obs}(T_j)$ and computed $c(T_j)$ phase-velocity, is defined as:

---

[4] This reflects a trade-off choice between the number of free parameters and the desired high-resolution for the study region. The global inversion avoids artificial mapping of perturbations into our focus area.

[5] Knopoff's method is computationally very efficient and supplies the phase-velocities at each considered period, making our approach of using a combination of a gradient-descent method and a random-Monte-Carlo search (Deschamps *et al.* 2008) feasible. We were thus capable to find three-dimensional shear-velocity models together with estimated standard deviations of the whole study region for both ray- and finite-frequency-theory-derived dispersion curves.

$$\chi^2 = \sum_j \frac{\left[c_{obs}\left(T_j\right) - c\left(T_j\right)\right]^2}{\sigma_j^2} + \eta \sum_j \frac{\left[c'_{obs}\left(T_j\right) - c'\left(T_j\right)\right]^2}{\sigma_j^2},$$

where $'$ denotes derivation with respect to period and η acts as a weighting parameter for the second term (similar to fitting group velocities). We attribute to all solution profiles, for which the phase-velocities lie within one standard deviation of the observational error, a probability p that depends on the corresponding χ^2 value:

$$p = k\ e^{-\frac{\chi^2}{2}}$$

where k is a normalization constant. Our final, preferred profile[6] coincides with the weighted (with weight p) average of all those profiles, accompanied by the corresponding standard deviations (Deschamps *et al.* 2008).

4.4 Results

Figure 4.1 shows examples of our phase-velocity maps at four different periods (40 s, 75 s, 150 s and 250 s) with a possibly important difference between ray- and finite-frequency-theory-derived maps visible at 150 s. A distinct fast anomaly is mapped by finite-frequency between the Southern Apennines and the Hellenic Arc, while from ray-theory it appears to follow the Dinarides. We also see that the differences between the two theoretical approaches become stronger for maps derived at longer surface-wave periods[7].

Although the sensitivity of Rayleigh waves at the shortest period we consider (35 s) has highest sensitivity mostly below the Moho (Boschi & Ekström 2002), their sensitivity to the crust is still considerable. We constructed an artificial V_s profile with crustal

---

[6] We also experimented with other approaches to find a best depth profile: (i) using genetic algorithms (like e.g. Zivcic *et al.* 2000) and (ii) combining genetic algorithms with gradient-descent methods. After several synthetic tests, we found that approach (i) suffers from the strong non-uniqueness of the problem, i.e. a vast number of best models found by the algorithm explained the data equally well, while gradients for each layer computed in approach (ii) were penalized by the strong non-linearity of the problem, i.e. the model parameters depend strongly on each other (Panza *et al.* 2007).

[7] This is a coherent result, as for shorter periods the numerical sensitivity kernels are increasingly close to the corresponding, simple ray-theory paths (Boschi 2006).

Figure 4.1: Phase-velocity maps obtained from inversions based on numerical finite-frequency and ray theory of Rayleigh-wave phase-anomaly measurements at 40 s, 75 s, 150 s and 250 s of the new composite dataset of Fry *et al.* (2008).

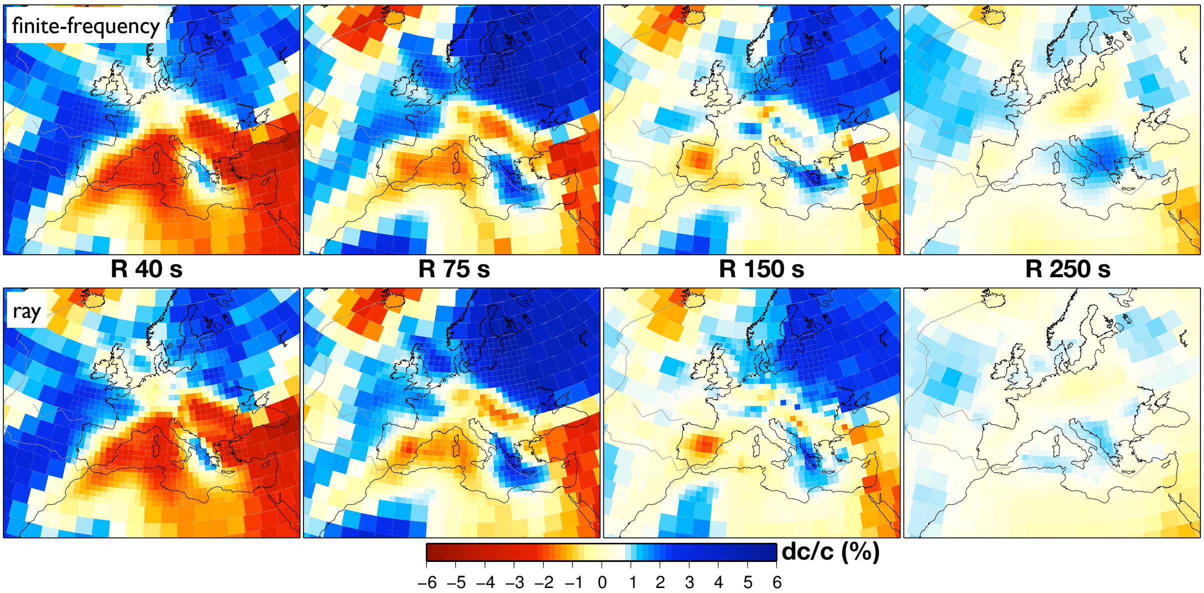

layers from Crust-2.0 and EuCrust-07 but some artificial upper mantle, and computed a corresponding "synthetic" dispersion curve by Knopoff's method. We then inverted this synthetic dispersion curve with starting profiles different from the "input" model. Figure 4.2a illustrates results of two such tests, with crustal structure fixed in the inversion, either to PREM crust or to our crustal model based on Crust-2.0 and EuCrust-07, used to generate the synthetics. It is clear that (i) even if the starting model for the inversion is very wrong (gray dashed line) the input model can be retrieved properly, but (ii) only if the crustal model is reliable. In the absence of a "good" crustal model, retrieved upper-mantle structure is wrong down to $\sim$ 200 km depth.

The three-dimensional models derived by ray and finite-frequency theory exhibit differences under Southern Italy and the Hellenic arc at depths between 150 - 400 km. Figure 4.2b shows one of the V_s profiles from the "observed" dispersion curves derived by finite-frequency or ray theory for a location in Southern Italy (41.5°N, 16.5°E). In both cases, crustal structure is everywhere fixed to our crustal model, based on Crust-2.0 and EuCrust-07. Between 60 km and 100 km, both models show a positive anomaly,

Figure 4.2: Local shear-velocity profiles and their standard deviations (shaded areas). (a) “Synthetic” inversions of a dispersion curve computed from an “input” profile (black line), which is far from the starting upper-mantle profile (gray dashed). Output profiles are obtained fixing crustal structure of the starting profile to either PREM (red) or the crustal model used as input (blue). (b) Inverted dispersion curves obtained from finite-frequency (green) and ray-theory (blue) maps (Figure 4.1) for a location in Southern Italy, starting from PREM and crustal structure fixed to a Crust-2.0- and EuCrust-07-based model.

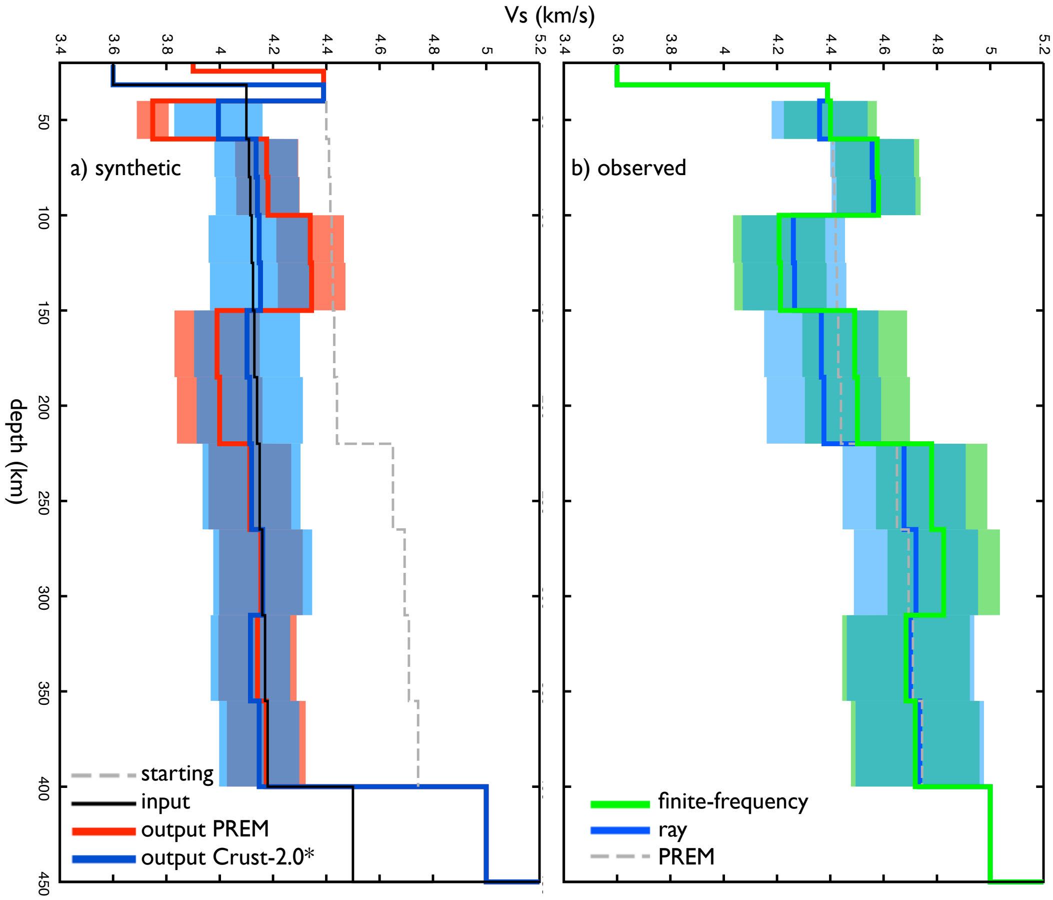

Figure 4.3: V_s perturbations (dVs) with respect to PREM at 40-60 km, 60-100 km, 100-150 km, 150-220 km, 220-310 km and 310-400 km depths based either on finite-frequency (left) or ray-theoretically (right) derived dispersion curves. The standard deviations (STD) of the corresponding shear-velocity anomalies are given to the left of the models.

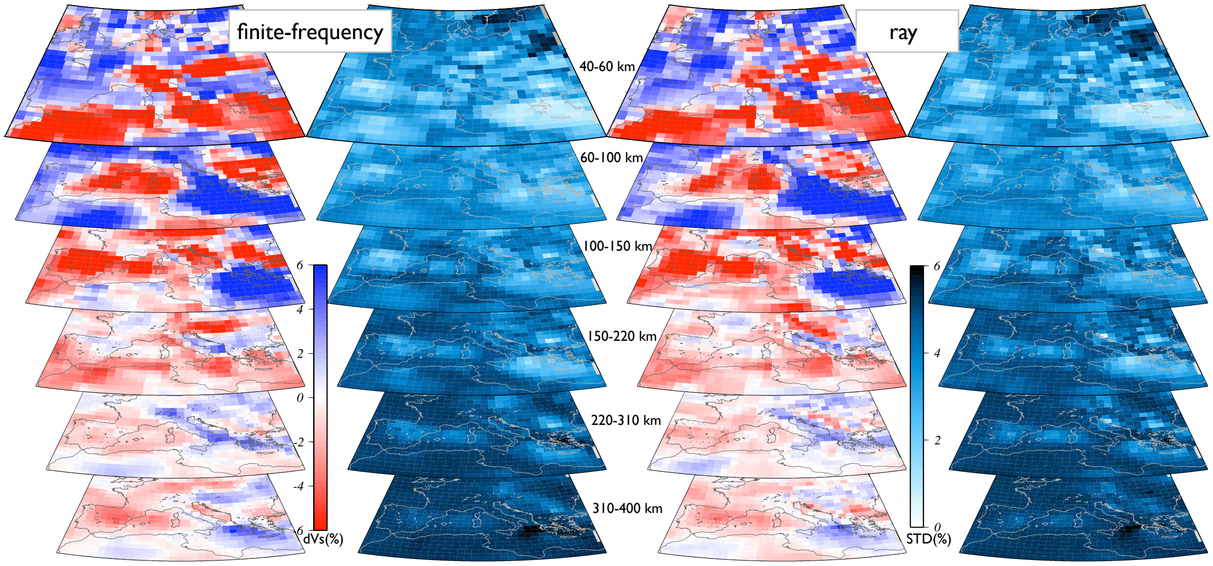

which at 100 - 150 km changes to a low-velocity layer. The inversion of the finite-frequency dispersion curve shows higher anomalies at depths between 150 - 310 km. Figure 4.3 and Figure 4.4 combine all the V_s perturbations (and their standard deviations) found as described. Standard deviations grow with depth and can range up to 6%, which indicates a decrease of the resolving power in the dispersion curves[8].

4.5 Discussion

Our Rayleigh-wave phase-velocity maps, derived either ray-theoretically or using numerical finite-frequency sensitivity kernels, confirm the same important differences[9] as

---

[8] The improvement in resolution possibly achieved by finite-frequency theory in the first step (phase-velocity maps) might be partly lost, when we attempt to constrain a higher number of free parameters to derive a three-dimensional map.

[9] Especially the fast phase-velocity anomaly related to the subduction zone in Southern Greece, is shifted in the finite-frequency inversions towards the Apennines while in ray-theoretically derived

Figure 4.4: Perspective view of four different cross-sections through the finite-frequency shear-velocity model of Figure 4.3.

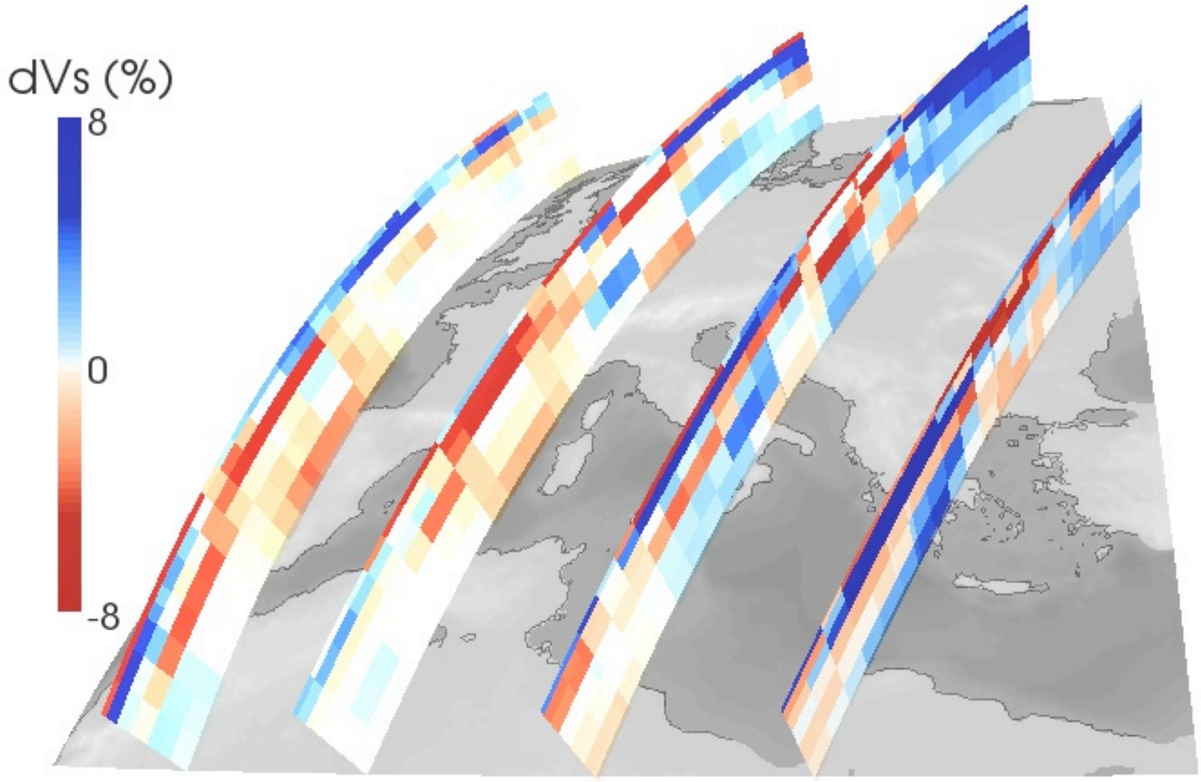

pointed out by Fry *et al.* (2008). We additionally find that the crustal structure plays an important role in the correct determination of the uppermost ∼ 200 km of the radial V_s profiles[10]. Including shorter surface-wave periods from noise correlations could allow to extend our model search and invert simultaneously for crustal layer parameters (Yao *et al.* 2007; Panza *et al.* 2007). In both V_s-models (Figure 4.3) we see the slow anomaly

---

solutions, this anomaly follows the Balkan coastline. In both cases, the extend of this fast anomaly is smaller and more focussed than in the inversions of Fry *et al.* (2008), which might result from our numerical finite-frequency approach and the include of major-arc measurements at longer periods (150 s to 300 s).

[10] The inversions of synthetic dispersion curves reveal the difficulty of constraining the velocity layers of the upper mantle by such a method. As already pointed out by Pontevivo & Thybo (2006) and van Heijst *et al.* (1994), it becomes important to find additional constraints.

The crustal description applied in these inversions should be as accurate as possible in order to correctly identify the seismic velocity profile in the uppermost mantle. This seems to confirm the general importance of crustal corrections in the determination of upper mantle structures (Tesauro *et al.* 2008; Bozdag & Trampert 2008).

in the western Mediterranean, associated with the tectonic extension of this area, the fast anomaly associated with subduction at the Hellenic Arc, and the slow anomaly under the Aegean sea and the Carpathian mountains, also found by Boschi *et al.* (2004) and Marone *et al.* (2004). At shallower depths, our models show a strong, high-velocity anomaly under the Hellenic Arc at 60 - 150 km depths. Although this general feature is related to the Dinarides-Hellenides subduction (Panza *et al.* 2007), the dipping angle can only be poorly resolved in our inversions[11]. At 220 - 310 km depth, a high V_s-anomaly stretching along the Southern Apennines up to Northern Italy is identified in the finite-frequency inversion, while in the ray-theoretical model this anomaly seems to be shifted eastwards under the Adriatic sea.

With respect to the ray-theory solution, the finite-frequency one is more coherent with V_p structure found in a tectonic reconstruction of the temperature field (de Jonge *et al.* 1994). For example, compare Figure 4.3 (layer at 220 - 310 km) with fig. 6 of Boschi *et al.* (2004). Additionally, in the same depth range, a fast anomaly under the Central Alps, also found by Schmid *et al.* (2008), is reproduced more clearly in our finite-frequency model than in the ray-theoretical one. Compare, in particular, our Tunisia-Central Europe cross-section of Figure 4.4 with fig. 8 of Boschi *et al.* (2004). These are indications that our finite-frequency method achieves higher resolution than ray theory. Still, standard deviations in these depth ranges are between 2% and 5%, obscuring model differences[12].

4.6 Conclusions

We inverted a new, high-quality phase-anomaly database of intermediate to long-period Rayleigh waves, confirming (at 150 s period) the presence of a distinct low-phase-velocity zone between Southern Italy and the Hellenic Trench in finite-frequency inversions, which is shifted to the Balkan coastline for ray-theoretical inversions (Fry *et al.* 2008). We constructed three-dimensional shear-velocity models by inverting dispersion curves, found at each location in the European-Mediterranean region, from the previously obtained phase-velocity maps derived by ray- and finite-frequency theory. Despite differences in these maps, the inverted depth profiles (assembled to form a three-dimensional model in Figure 4.3 and Figure 4.4) show only little variation between the results of the two approaches. An improved coherence between tectonic reconstructions (de Jonge *et al.* 1994) and our finite-frequency model suggests that finite-frequency tomography can reveal Earth structure in more detail than ray-theory, but standard deviations, i.e. error bars on tomographic results, are large enough that differences between the two models cannot be considered statistically significant. Better constrained dispersion curves and refined models of the crust should allow to reduce the error bar, and eventually quantify the improvement achieved via a finite-frequency approach.

---

[11] Boschi *et al.* (2004) find a sharp vertical feature (see their cross-section in fig. 7), although their model is much smoother.

[12] In general, we confirm that uncertainties in finite-frequency and ray-theoretical models make it difficult to discriminate between them (Boschi *et al.* 2006; Trampert & Spetzler 2006).

Acknowledgments

We thank John Woodhouse for giving us access to the large computational facility at the Department of Earth Sciences, Oxford University. We also gratefully acknowledge support from the European Commission's Human Resources and Mobility Programme, Marie Curie Research Training Networks.

Bibliography

[1] Baer, M., P. Zweifel and D. Giardini, 2000. The Swiss digital seismic network (SDSNet), Orfeus Newsl., 2(2), 1-5.

[2] Bassin, C., G. Laske and G. Masters, 2000. The current limits of resolution for surface wave tomography in North America, *EOS, Trans. Am. geophys. Un.,* **81**(F897).

[3] Boschi, L. and G. Ekström, 2002. New images of the Earth's upper mantle from measurements of surface wave phase velocity anomalies, *Journal of Geophysical Research-Solid Earth*, *107*: p. 10.1029/2000JB000059.

[4] Boschi, L., G. Ekström and B. Kustowski, 2004. Multiple resolution surface wave tomography: the Mediterranean basin, *Geophysical Journal International*, *157*: p. 293-304.

[5] Boschi, L., T. W. Becker, G. Soldati and A. M. Dziewonski, 2006. On the relevance of Born theory in global seismic tomography, *Geophysical Research Letters*, *33*: p. L06302, doi:10.1029/2005GL025063.

[6] Boschi, L., 2006. Global multiresolution models of surface wave propagation: comparing equivalently regularized Born and ray theoretical solutions, *Geophysical Journal International*, *167*: p. 238-252.

[7] Bozdag, E. and J. Trampert, 2008. On crustal corrections in surface wave tomography, *Geophysical Journal International*, *172*: p. 1066-1082.

[8] de Jonge, M. R., M. J. R. Wortel and W. Spakman, 1994. Regional-Scale Tectonic Evolution and the Seismic Velocity Structure of the Lithosphere and Upper-Mantle - the Mediterranean Region, *Journal of Geophysical Research-Solid Earth*, *99*: p. 12091-12108.

[9] Deschamps, F., S. Lebedev, T. Meier and J. Trampert, 2008. Stratified seismic anisotropy reveals past and present deformation beneath the East-central United States, *Earth and Planetary Science Letters*, in prep.

[10] Dziewonski, A. M. and D. L. Anderson, 1981. Preliminary Reference Earth Model, *Physics of the Earth and Planetary Interiors*, *25*: p. 297-356.

[11] Ekström, G., J. Tromp and E. W. F. Larson, 1997. Measurements and global models of surface wave propagation, *J. geophys. Res.,* **102**, 8137–8157.

[12] Fry, B., 2007. *Surface wave tomography of the Mediterranean and central Europe: a new shear wave velocity model*, Ph.D. thesis, ETH Zurich, Switzerland.

[13] Fry, B., L. Boschi, G. Ekström and D. Giardini, 2008. Europe-Mediterranean tomography: High correlation between new seismic data and independent geophysical observables, *Geophysical Research Letters*, *35*: p. L04301.

[14] Knopoff, L., 1964. A matrix method for elastic wave problems, *Bull. Seism. Soc. Am.* , *54*: p. 431-438.

[15] Knopoff, L., 1972. Observation and inversion of surface-wave dispersion, Tectonophysics, 13(1-4), p. 497–519.

[16] Marone, F., S. van der Lee and D. Giardini, 2004. Three-dimensional upper-mantle S-velocity model for the Eurasia-Africa plate boundary region, *Geophysical Journal International*, *158*: p. 109-130.

[17] Paige, C. C. and M. A. Saunders, 1982. Lsqr - an Algorithm for Sparse Linear-Equations and Sparse Least-Squares, *Acm Transactions on Mathematical Software*, *8*: p. 43-71.

[18] Panza, G. F., A. Peccerillo, A. Aoudia and B. Farina, 2007. Geophysical and petrological modelling of the structure and composition of the crust and upper mantle in complex geodynamic settings: The Tyrrhenian Sea and surroundings, *Earth-Science Reviews*, *80*: p. 1-46.

[19] Peter, D., C. Tape, L. Boschi and J. H. Woodhouse, 2007. Surface wave tomography: global membrane waves and adjoint methods, *Geophys. J. Int.,* , *171*: p. 1098-1117.

[20] Piromallo, C. and A. Morelli, 2003. P wave tomography of the mantle under the Alpine-Mediterranean area, *Journal of Geophysical Research-Solid Earth*, *108*: p. 2065.

[21] Pontevivo, A. and H. Thybo, 2006. Test of the upper mantle low velocity layer in Siberia with surface waves, *Tectonophysics*, *416*: p. 113-131.

[22] Ritzwoller, M. H., Y. Yang, A.L. Levshin, E.R Engdahl and N.M. Shapiro, 2006. Thoughts on a European Seismic Reference Model: The role of surface waves from earthquakes and ambient noise, *Geophysical Research Abstracts*, *8*: EGU06-A-05281.

[23] Schmid, C., S. van der Lee, J. C. VanDecar, E. R. Engdahl and D. Giardini, 2008. Three-dimensional S velocity of the mantle in the Africa-Eurasia plate boundary region from phase arrival times and regional waveforms, *Journal of Geophysical Research-Solid Earth*, *113*: p. B03306.

[24] Schwab, F. and L. Knopoff, 1970. Surface-Wave Dispersion Computations, *Bulletin of the Seismological Society of America*, *60*: p. 321-344.

[25] Shapiro, N. M. and M. H. Ritzwoller, 2002. Monte-Carlo inversion for a global shear-velocity model of the crust and upper mantle, *Geophysical Journal International*, *151*: p. 88-105.

[26] Spakman, W., S. van der Lee and R. van der Hilst, 1993. Travel-Time Tomography of the European Mediterranean Mantle down to 1400 Km, *Physics of the Earth and Planetary Interiors*, *79*: p. 3-74.

[27] Stammler, K. and W. Hanka, 2002. Technical aspects of the GRSN, in Ten Years of German Regional Seismic Network (GRSN), Dtsch. Forschungsgem. Senatskomm. Geowiss. Gemeinschaftsforsch., vol. 25, edited by M. Korn, pp. 21–39, John Wiley, Weinheim, Germany.

[28] Tarantola, A., 2005. Inverse problem theory and methods for model parameter estimation, *Philadelphia, PA: Society for Industrial and Applied Mathematics.*

[29] Tesauro, M., M. K. Kaban and S. A. P. L. Cloetingh, 2008. Eucrust-07: A New Reference Model for the European Crust, *Geophysical Research Letters*, *35*: p. L05313.

[30] Trampert, J. and J. H. Woodhouse, 2001. Assessment of global phase velocity models, *Geophys. J. Int., , 144*: p. 165-174.

[31] Trampert, J. and J. Spetzler, 2006. Surface wave tomography: finite-frequency effects lost in the null space, *Geophysical Journal International*, *164*: p. 394-400.

[32] van Heijst, H. J., R. Snieder and R. Nowack, 1994. Resolving a Low-Velocity Zone with Surface-Wave Data, *Geophysical Journal International*, *118*: p. 333-343.

[33] Wortel, M. J. R., and W. Spakman, 2001. Subduction and slab detachment in the mediterranean-carpathian region, *Science*, 291(5503), 437–437.

[34] Yao, H. J., C. Beghein and R. D. van der Hilst, 2008. Surface wave array tomography in SE Tibet from ambient seismic noise and two-station analysis - II. Crustal and upper-mantle structure, *Geophysical Journal International*, *173*: p. 205-219.

[35] Zivcic, M., I. Bondar and G. F. Panza, 2000. Upper crustal velocity structure in Slovenia from Rayleigh wave dispersion, *Pure and Applied Geophysics*, *157*: p. 131-146.

5 Conclusions

This thesis first describes a simplified model of surface wave propagation, that I designed for the purpose of determining the sensitivity of phase-anomaly measurements to perturbations in phase velocity. The "membrane wave model" turns out to be very effective in terms of computational costs. The adjoint method additionally allows to calculate sensitivities for a heterogeneous reference Earth, an effort too expensive for analytical descriptions. By employing the combination of this membrane wave model and the adjoint method, it has been feasible for the first time in global seismology to iteratively invert for phase-velocity distributions using a finite-frequency approach on a completely numerical basis. I have also been able to validate the adjoint method by comparison with the result of a very large, "brute force" set of forward simulations.

The second part of this thesis shows the complex implications of different theoretical descriptions of seismic wave propagation upon the inverse problem of determining an a priori Earth's structure. I quantify the resolution limits of ray theory versus finite-frequency theory for both the forward and the inverse problem, finding tomographic resolution to be improved in the finite-frequency with respect to the ray-theory approach. Utilizing the membrane wave model to construct a large synthetic phase-anomaly dataset for a given "input" Earth model, I have verified the better performance of the finite-frequency checkerboard tests. Such synthetic benchmarks are in general very expensive to conduct in a three-dimensional case, and too expensive for a comparable size of measurements as are available in current global tomographic databases, but the membrane wave approach makes them computationally feasible. For very heterogeneous input models, I verified that the input model can still be retrieved, provided that the inversion procedure is iterated a few times. This requires that sensitivity kernels be recalculated and the high performance of the adjoint method employed here is, again, essential.

The last part of this thesis shows an application of the numerical finite-frequency approach to determine a new, three-dimensional shear-velocity model for Europe and the Mediterranean region. By employing the membrane wave model, it has been possible to calculate a sensitivity kernel for each measurement at every available period of an unprecedentedly rich, high-quality surface-wave phase-anomaly dataset. A completely numerical, finite-frequency procedure led to a high-resolution dataset of Rayleigh-wave dispersion curves, densely covering the focus area. In a second step, a Monte-Carlo search algorithm exhaustively explored the complete model space of upper-mantle profiles down to 400 km. The associated model uncertainty was also determined to supply reliability limits of the found shear-velocity structures. Comparisons with independent studies suggest that the finite-frequency approach achieves an improvement with respect to the ray-theoretical one, but uncertainties in the dispersion curves make both approaches statistically equivalent.

As computational power increases, the work done here indicates strategies that will allow to solve the Earth's equations of motion in unprecedented detail. An outlook of such future computational developments is given in the appendix. A promising approach for global seismology seems to be an exploration of the adjoint method in order to derive three-dimensional models based on finite-frequency theory, making it possible to derive higher-resolution images by completely numerical approaches. Through constant efforts, the size of databases in global seismology will continuously be increased. Parallel efforts to augment the number of seismic stations, and the density of station coverage at the local, regional and global scale will allow to reveal more and more details in Earth's structure. Future tomographic methods should not only rely on data coverage improvements, but also try to extract from new databases as much information as possible, to more robustly constrain the inverse problem in global seismology. A more accurate, albeit computationally challenging, description of seismic wave propagation will help to solve this inverse problem. The work done here motivates to go into such a computational direction, showing that numerical finite-frequency tomography is a rewarding application to global seismology.

A Petascale Computing for Future Breakthroughs in Global Seismology

---

A.1 Introduction

A.2 Limiting factors of tomographic resolution

A.3 Statistically sound, linearized ray-theory tomography

A.4 Numerical finite-frequency tomography

A.4.1 Implementation and computational cost

A.5 Summary

Abstract

Will the advent of "petascale" computers be relevant to research in global seismic tomography? We illustrate here in detail two possible consequences of the expected leap in computing capability. First, being able to identify larger sets of differently regularized/parameterized solutions in shorter times will allow to evaluate their relative quality by more accurate statistical criteria than in the past. Second, it will become possible to compile large databases of sensitivity kernels, and update them efficiently in a non-linear inversion while iterating towards an optimal solution. We quantify the expected computational cost of the above endeavors, as a function of model resolution, and of the highest considered seismic-wave frequency.

As a co-author, I provide this appendix published in *Phys. Earth planet. Inter.,* 2007, and written by Lapo Boschi, for completeness. Further co-authors were Jean-Paul Ampuero, Martin Mai, Gaia Soldati and Domenico Giardini.

A.1 Introduction

In the past decade there have been a number of claims by tomographers that lead to a re-consideration of certain aspects of the theory of the Earth. Those claims have been justified by improvements in tomographic resolution. van der Hilst *et al.* (1997), for example, inverted a very large database on an unprecedentedly dense voxel grid, making use of an inversion algorithm that exploited the inherent sparsity of the linear inverse problem. They found very sharp images of fast, deep heterogeneities, that, because of their geographic distribution, were explained in terms of subducted material, sinking into the lower mantle. This finding, while subject of debate (is "resolution" really as high as claimed?), has been a strong argument in favour of whole-mantle vs. layered convection. More recent examples are the work of Ishii & Dziewonski (2003), who mapped an "innermost inner core" of only 300 km in radius, suggesting that it be "the oldest fossil left from the formation of Earth", and the controversial article of Montelli *et al.* (2004), who improved global resolution by means of a more accurate approach to the calculation of sensitivity functions, and found "clear evidence that a limited number of hotspots are fed by plumes originating in the lower mantle"; this claim is clearly relevant to the current debate on the nature of mantle plumes (e.g., Sleep 2006), involving all disciplines in the Earth sciences, and stirred a very animated debate.

The controversy originated by these publications, and, in general, the lack of correlation at short spatial wavelengths between tomographic images derived in different approaches (e.g., Becker & Boschi, 2002) indicate that the next important challenge in global seismic tomography is that of finding effective ways to improve the images' resolution. We describe in the following the role that high-performance computing might play, in reference to developments in tomographic imaging and the subsequent interpretation of mapped Earth structure.

A.2 Limiting factors of tomographic resolution

Tomographic resolution, or the smallest lateral extent of a velocity anomaly that can be correctly mapped by an inversion algorithm, is limited by (i) the geographic coverage of inverted seismic observations, (ii) the resolving power of the selected parameterization, (iii) the accuracy of the theoretical formulation, or the equation relating seismic data to the velocity field. The latter problem has been explored, for example, in the recent

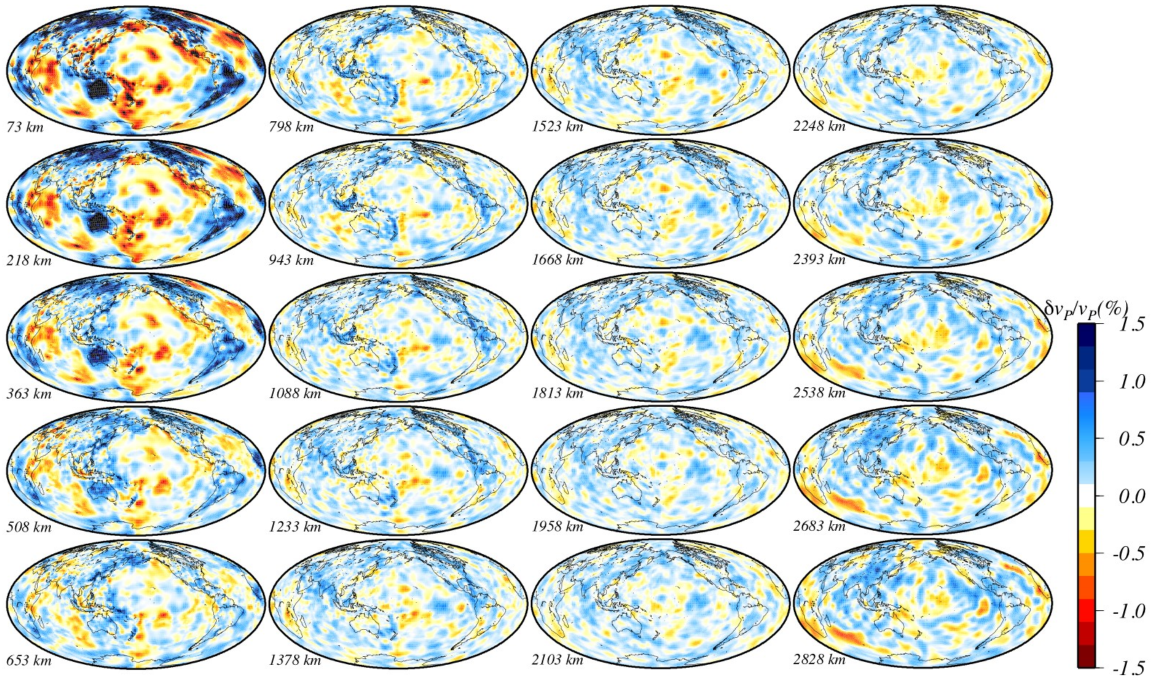
73 km
798 km
1523 km
2248 km
218 km
943 km
1668 km
2393 km
363 km
1088 km
1813 km
2538 km
508 km
1233 km
1958 km
2683 km
653 km
1378 km
2103 km
2828 km
δv_P/v_P(%)
1.5
1.0
0.5
0.0
-0.5
-1.0
-1.5

Figure A.1: P-velocity model *vox1.5p*, shown in its entirety. The mean depth of each layer is given below and to the left of the corresponding panel. *vox1.5p* was derived from Antolik *et al.*'s (2001)database of P-wave travel times.

works of Montelli *et al.* (2004, 2006), Boschi *et al.* (2006), and Boschi (2006), and while differences between ray-theory and finite-frequency models exist, they do not seem to be as important as those caused, at this stage, by (i) or (ii). (i) has been a major limiting factor in the past: the density of the parameterization is proportional to the number of basis functions (i.e. number of model coefficients, or "free parameters") used to describe the tomographic image, which in turn defines the size of the inverse problem to be solved. Pioneers of global seismic tomography like Dziewonski (1984) or Woodhouse & Dziewonski (1984), even using what at the time were regarded as very powerful computers, could only afford a model parameterization in terms of $\sim 10^2$ free parameters. The mid-90s breakthroughs of Grand (1994) and van der Hilst *et al.* (1997) consisted in employing a *voxel* parameterization (as opposed to the harmonic one of Dziewonski (1984) and Woodhouse & Dziewonski (1984)), resulting in a sparse inverse problem, solvable by iterative algorithms–hence, lower RAM and computation time requirements (e.g. Trefethen & Bau, 1997), allowing to invert for $\sim 10^5$ model coefficients. A decade later, this issue is not as relevant anymore. Owing to an adaptive-grid approach, Bijwaard *et al.* (1998) have been able to make use of a parameterization locally as fine as 0.6°, while keeping the total number of free parameters relatively low. More recently, model $vox1.5p$ of Boschi *et al.* (2007) (figure A.1) based on an approximately equal-volume grid, achieves instead a constant nominal resolution of 1.5°. It consists of 366,640 free parameters, and yet one inversion requires only minutes on a 1-CPU desktop computer.

We infer that at the current stage of global seismic tomography, the main factor limiting resolution is data coverage, which, without a large network of ocean-bottom receivers, will remain poor in regions underlying oceans. In the absence of uniform station coverage, the main challenge for seismic tomographers is to establish appropriate parameterization/regularization criteria, to damp instabilities caused by lack of data, without obscuring valuable information.

A.3 Statistically sound, linearized ray-theory tomography

Establishing a criterion to identify the highest-likelihood model in a family of solutions that would intuitively be considered “acceptable” has been a major problem–and limiting factor for resolution–in global seismic tomography, with the choice of a “best” model left to the author’s subjective consideration.

Since the seminal work of Akaike (1974), rigorous “information criteria” have been derived (e.g., Burnham & Anderson 2002; Hurvich & Tsai 1989; Leonard & Tsu 1999) to determine the actual number of free parameters needed to explain a given seismic database; they have not been applied often to global seismic tomography, probably because of their high computational cost. They require that many inversions be performed on grids of various density (nominal resolution); the “number of degrees of freedom” associated with each inversion must also be found, evaluating the model resolution matrix **R** and its trace (Boschi *et al.* 2006). This is the most time-consuming step, but can be perfectly parallelized as explained e.g. by Soldati *et al.* (2007).

We have experimented with Antolik *et al.*’s (2001) database of P-wave travel-time observations, inverting them for isotropic, 3-D structure in mantle P-velocity. The CPU-time needed to conduct a family of such inversions, spanning a broad range of solution-model complexity values, is shown in figure A.2 as a function of parameterization density. The CPU-time for one inversion at the highest resolution considered here ($\sim 10^5$ voxels of 1.5° horizontal extent) is $\sim 10^2$s in the "acceptable"-solution region, and to find **R** we must complete $\sim 10^5$ such inversions, resulting in a total single-CPU time of $\sim 10^7$s, or, from our benchmark of the CPU on which the exercise was conducted (speed $\sim 1 \times 10^9$ Flop per second), $\sim$ 10Petaflop. Two such computations will need to be performed.

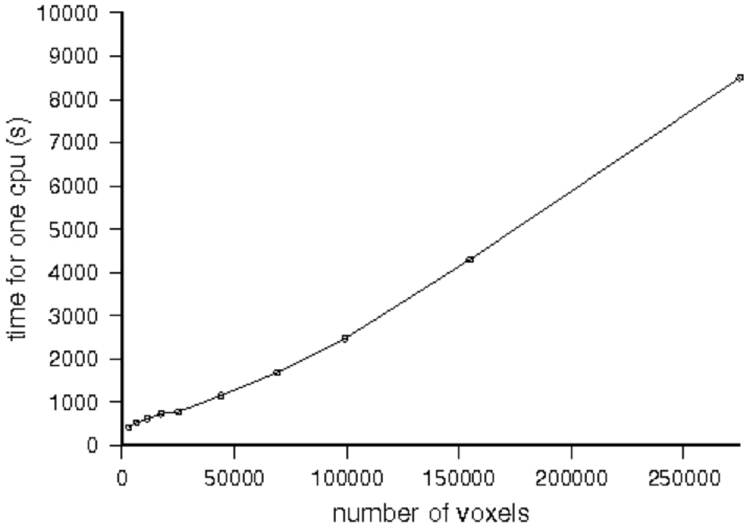

Figure A.2: At each parameterization level (horizontal axis, from 15° to 1.5° nominal resolution; 15 layers) we conduct 27 LSQR inversions, each with a different regularization parameter. The time needed to complete this exercise is plotted on the vertical axis. We find 27 solutions of variable roughness, ranging between the strongly underdamped and strongly overdamped regions.

We applied AICC, or Akaike corrected information criterion (Hurvich & Tsai 1989; Dal Forno *et al.* 2005) to the mentioned, global mantle P-velocity inverse problem. The densest grid we employed has 3.75° horizontal spacing, while the vertical parameterization remains constant (15, $\sim$ 200km-thick layers). Calculations of **R** were conducted on a 20-CPU Linux cluster. Results shown in figure A.3 indicate that the information content of both weakly and strongly regularized solutions continues to grow with growing number of degrees of freedom. To find the curve's maximum, the exercise needs to be iterated on even denser grids, requiring in practice (as one could estimate from figure A.2) petascale capacities.

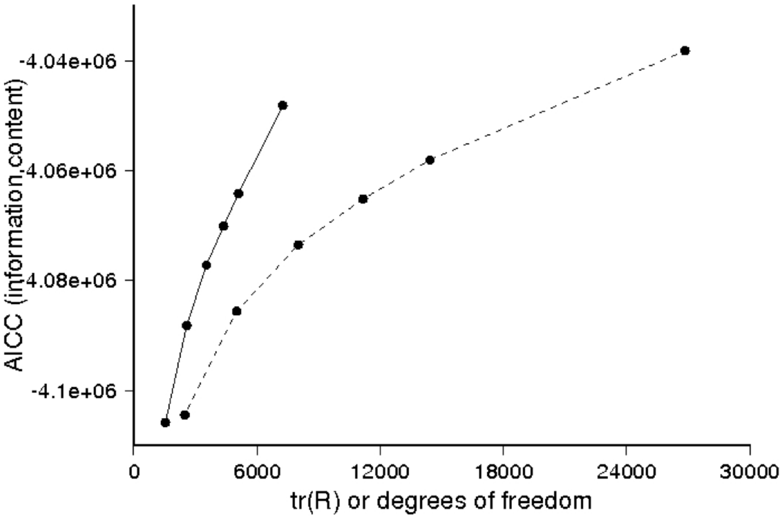

Figure A.3: Corrected Akaike-criterion likelihood as a function of the trace of the resolution matrix. The latter is a measure of the number of degrees of freedom of the solution. We change it by leaving the regularization constraints fixed, but varying the parameterization density (15 vertical layers with decreasing 15°, 10°, 7.5°, 6°, 5° and 3.75° horizontal gridsize). The solid line corresponds to strongly damped, but acceptable solutions; the dashed to weakly damped but acceptable.

AICC is a subjective choice, and we plan to explore other information criteria, the most popular alternative to AICC being perhaps the Bayesian information criterion, employed for example by Oda & Shibuya (1996), or Sambridge (2006).

A.4 Numerical finite-frequency tomography

An increasing number of authors in global seismology are beginning to use finite-frequency sensitivity kernels rather than simple ray theory to develop higher-resolution tomographic images of the Earth's mantle, inverting seismic observations made at relatively long periods, where finite-frequency effects might be more relevant and affect tomographic resolution strongly (Boschi (2006) for a list of more or less recent works in global finite-frequency tomography). High-performance computers allow to compute sensitivity kernels numerically, by means of the adjoint method (Tromp *et al.* 2005; Peter *et al.* 2007) and/or the scattering integral method (Chen *et al.* 2006). As opposed to the analytical approach (e.g. Dahlen *et al.* 2000), numerical methods are more flexible with respect to changes in the reference model, whose lateral heterogeneities will be properly accounted for.

An example of the effects of lateral heterogeneities on sensitivity kernels is shown in figure A.4, where the finite-element "membrane wave" approach (Tanimoto 1990; Tape 2003; Peter *et al.* 2007; Tape *et al.*, 2007) is used to compute the sensitivity of Love-wave phase anomalies to phase velocity at a period of 150s. Differences between spherical- and aspherical-Earth kernels are small, but comparable to the kernels themselves; while not affecting the long-wavelength character of our global tomographic images, they become increasingly relevant as features of shorter wavelength are to be resolved (Peter *et al.* 2007).

Figure A.4: Example of numerical kernels (dimensionless) derived with the adjoint method for 150 s Love waves in (a) homogeneous and (b) heterogeneous starting phase-velocity models. (c) Difference between (a) and (b). (From Peter *et al.* 2007.)

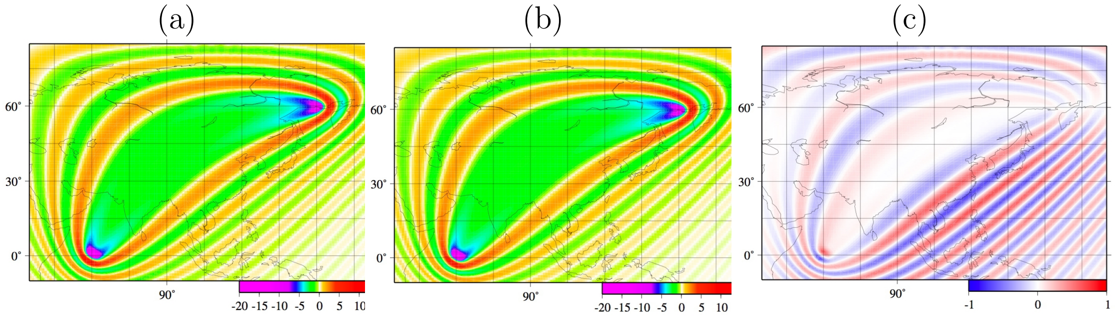

A.4.1 Implementation and computational cost

The computation of sensitivity kernels is by far the most expensive step of any finite-frequency tomography algorithm. There exists one kernel per source-receiver couple, i.e. one kernel per observation, and in principle the adjoint method requires that two simulations be conducted to compute each kernel. However, the total number of simulations to compute all kernels associated with a given database can be reduced in various ways (e.g., Capdeville *et al.* 2005; Tromp *et al.* 2006). Most recently, Chen *et al.* (2006)

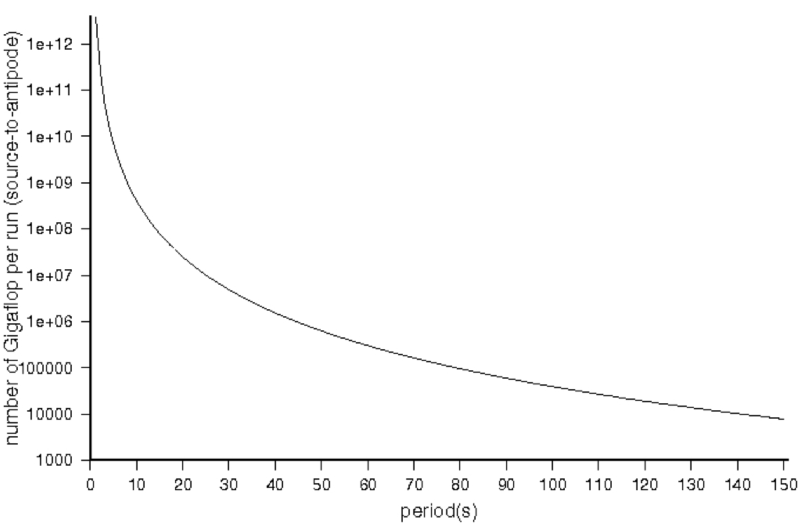

Figure A.5: Expected cost of one global spectral-element simulation of waves propagating from a source to its antipode, as a function of the shortest (and most expensive) accurately modeled period. We chose accuracy, defined as arrival time error normalized by total travel time, to be $\sim 10^{-4}$. (Based on Ampuero & Nissen-Meyer 2007.)

show that this number can be reduced to $3n_R + n_S$, where n_R denotes the number of (3-component) receivers, and n_S the number of sources.

Today, the most widely used, and possibly most efficient algorithm for numerical simulations of global seismic wave propagation is the spectral-element software package *Specfem* (e.g., Komatitsch *et al.* 2002). Ampuero & Nissen-Meyer (2007) show that the cost of one run of*Specfem* is related to the shortest (most expensive) period to be accurately modeled, T_{min}, by

$$\text{cost in Flop} = \left(\frac{2\pi\Delta}{c_0 T_{\mathrm{min}}}\right)^4 \times \Gamma, \tag{A.1}$$

where Δ denotes epicentral distance and c_0 reference (mean) phase velocity, and the parameter Γ depends on the largest tolerated error, which we define as arrival time error normalized by total travel time. Choosing the latter to be $\sim 10^{-4}$, the curve in figure A.5 is found.

If only minor-arc phase-anomaly observations are considered, then $\Delta \leq 180°$, and with

$T_{\text{min}} = 20$s (Qin *et al.* 2006) (hence the cost of one simulation $\sim 10^7$Gigaflop from figure A.5) and $n_R \sim n_S \sim 10^2$, we can expect the cost of computing all necessary kernels to be $\sim 10^3$ Petaflop. This figure does not include the cost of input/output operations (which might become necessary as the shortest modeled period is diminished, parameterization refined, and RAM subsequently becomes insufficient), or reconstruction of the *forward* wavefield by solving the wave equation backwards in time (Tromp *et al.*, 2005; Chen *et al.*, 2006). In our preliminary runs of *Specfem* on a 20-CPU cluster, we have found the backpropagation of the adjoint wavefield to take roughly as long as three normal forward propagations with the same source-receiver geometry.

Sensitivity kernels also need to be updated a few times, repeating each time the same number of *Specfem* runs, and taking the result of each inversion as the starting point for the next, until convergence is reached.

Specfem has been shown to perform and scale extremely well (Komatitsch *et al.*, 2003). Additionally, once an optimal number of processors per simulation has been found, the computation can be further parallelized by performing a number of simulations at the same time, each on a different chunk of the cluster (recall that $3n_R + n_S$ simulations have to be performed at each iteration).

A.5 Summary

Improving the resolution of tomographic maps is crucial to answer important questions on the nature of the Earth's mantle–the best current example being perhaps the debate on the origin of hotspots and on the very existence of mantle plumes (e.g., Sleep 2006), presumed narrow features that need high-resolution tomography to be properly mapped.

The RAM and speed of computers available to the scientific community are now sufficient to solve very large inverse problems in a short time, making it easy to derive very finely parameterized seismic images of the Earth. Nevertheless, as tomographers strive to enhance resolution, questions that still need to be addressed are (i) how to identify appropriate parameterization and/or regularization schemes, and (ii) how to surpass the resolution limit implicitly posed by the ray-theory approximation, still adopted by many researchers today.

We propose here to tackle (i) by means of computationally expensive statistical approaches like the Akaike criterion (Akaike 1974; Hurvich & Tsai 1989), now made feasible by the advent of petascale computing. We indicate the numerical approach to finite-frequency (Born-approximation) tomography as the best currently available answer to (ii), and analyze its cost as a function of increasing modeled/inverted seismic-wave frequency. The availability of petascale hardware will be integral to the implementation of numerical finite-frequency tomography at increasingly high resolution.

Bibliography

[1] Akaike, H., 1974. A new look at the statistical model identification, *IEEE Trans. Autom. Control*, **19**, 716–723.

[2] Ampuero J.-P., and T. Nissen-Meyer, 2007. High order conservative time schemes in spectral element methods for seismic wave propagation, in preparation.

[3] Antolik, M., G. Ekström, and A. M. Dziewonski, 2001. Global event location with full and sparse data sets using three-dimensional models of mantle P-wave velocity, *Pure Appl. Geophys.* **158**, 291–317.

[4] Becker, T. W., and L. Boschi, 2002. A comparison of tomographic and geodynamic mantle models *Geochem. Geophys. Geosyst.* **3**, 1003.

[5] Bijwaard, H., W. Spakman, and E. R. Engdahl, 1998. Closing the gap between regional and global travel time tomography *J. geophys. Res.,* **103**, 30055–30078.

[6] Boschi, L., 2006. Global multiresolution models of surface wave propagation: comparing equivalently regularized Born and ray theoretical solutions, *Geophys. J. Int.,* **167**, 238–252.

[7] Boschi, L., T. W. Becker, G. Soldati, and A. M. Dziewonski, 2006. On the relevance of Born theory in global seismic tomography, *Geophys. Res. Lett.,* **33**, L06302.

[8] Boschi, L., T. W. Becker, and B. Steinberger, 2007. Mantle plumes: seismic images and dynamic models, *Earth Planet. Sci. Lett.*, submitted.

[9] Burnham, K. P., and D. R. Anderson, 2002. *Model selection and multimodel inference. A practical information-theoretic approach*, Springer, New York, second edition.

[10] Capdeville, Y., Y. Gung, and B. Romanowicz, 2005. Towards global Earth tomography based on the spectral element method: a technique based on source stacking, *Geophys. J. Int.,* **162**, 541–554.

[11] Chen, P., T. H. Jordan, and L. Zhao, 2007. Full 3D waveform tomography: A comparison between the scatteringintegral and adjoint-wavefield methods, *Geophys. J. Int.*, in press.

[12] Dal Forno, G., P. Gasperini, and E. Boschi, 2005. Linear or nonlinear rheology in the mantle: A 3D finite-element approach to postglacial rebound modeling, *J. Geodyn.*, **39**, 183–195.

[13] Dziewonski, A. M., 1984. Mapping the lower mantle: determination of lateral heterogeneity in P velocity up to degree and order 6, *J. geophys. Res.,* **89**, 5929–5952.

[14] Grand, S. P., 1994. Mantle shear structure beneath the Americas and the surrounding oceans, *J. geophys. Res.,* **99**, 11591–11621.

[15] Hurvich, C. M., and C.-L. Tsai, 1989. Regression and time series model selection in small samples, *Biometrika*, **76**, 297–307.

[16] Ishii, M., and A. M. Dziewonski, 2003. Distinct seismic anisotropy at the centre of the Earth. *Phys. Earth Planet. Inter.*, **140**, 203–217.

[17] Komatitsch, D., J. Ritsema, and J. Tromp, 2002. The spectral-element method, Beowulf computing and global seismology, *Science*, **298**, 1737–1742.

[18] Komatitsch, D., S. Tsuboi, Ji. Chen, and J. Tromp, 2003. A 14.6 billion degrees of freedom, 5 teraflops, 2.5 terabyte earthquake simulation on the Earth Simulator, Proceedings of the Supercomputing 2003 Conference.

[19] Leonard, T., and S. J. Hsu, 1999. *Bayesian methods. An analysis for statisticians and interdisciplinary researchers*, Cambridge University Press, Cambridge, U.K.

[20] Montelli, R., G. Nolet, F. A. Dahlen, G. Masters, E. R. Engdahl, and S.-H. Hung, 2004. Finite-frequency tomography reveals a variety of plumes in the mantle, *Science* **303**, 338–343.

[21] Montelli, R., G. Nolet G, F. A. Dahlen, and G. Masters, 2006. A catalogue of deep mantle plumes: New results from finite-frequency tomography, *Geochem. Geophys. Geosyst.*, **7**, Q11007.

[22] Peter, D., C. Tape , L. Boschi, and J. H. Woodhouse, 2007. Surface wave tomography: global membrane waves and adjoint methods, *Geophys. J. Int.*, submitted.

[23] Qin, Y., Y. Capdeville, V. Maupin, and J.-P. Montagner, 2006. A SPICE blind test to benchmark global tomographic methods, abstract, AGU Fall meeting.

[24] Sambridge, M., K. Gallagher, A. Jackson, and P. Rickwood, 2006. Trans-dimensional inverse problems, model comparison and the evidence. *Geophys. J. Int.,* **167**, 528–542.

[25] Sleep, N. H., Mantle plumes from top to bottom, 2006. *Earth-Science Reviews*, **77**, 231–271.

[26] Soldati, G., L. Boschi, and A. Piersanti, 2007. Global seismic tomography and modern parallel computers, *Annals of Geophysics*, in press.

[27] Tanimoto, T., 1990. Modelling curved surface wave paths: membrane surface wave synthetics, *Geophys. J. Int.,* **102**, 89–100.

[28] Tape, C., 2003. *Waves on a spherical membrane*, M.Sc. Thesis, University of Oxford, U. K.

[29] Tape, C., Q. Liu, and J. Tromp, 2007. Finite-frequency tomography using adjoint methods–Methodology and examples using membrane surface waves, *Geophys. J. Int.,* submitted.

[30] Trefethen, L. N., and D. Bau III, 1997. *Numerical Linear Algebra*, Soc. for Ind. and Appl. Math., Philadelphia, Penn.

[31] Tromp, J., C. Tape, and Q. Liu, 2005. Seismic tomography, adjoint methods, time reversal and banana-doughnut kernels, *Geophys. J. Int.,* **160**, 195–216.

[32] Tromp, J., Q. Liu, C. Tape, and A. Maggi, 2006. Towards Seismic Tomography Based Upon Adjoint Methods, *Eos Trans. AGU*, **87**(52), Fall Meet. Suppl., Abstract S53C-05.

[33] van der Hilst, R. D., S. Widiyantoro, and E. R. Engdahl, 1997. *Nature*, **386**, 578–584.

[34] Woodhouse J. H., and A. M. Dziewonski, 1984. Mapping the upper mantle: three-dimensional modeling of Earth structure by inversion of seismic waveforms, *J. geophys. Res.,* **89**, 5953–5986.

Acknowledgments

This work was done under the guidance of Prof. Domencio Giardini. As co-supervisor, Dr. Lapo Boschi followed my work closely and this thesis benefitted a lot from his expertise. Additional stays at the IPG Paris with the collaboration and help of Dr. Yann Capdeville improved this research and will lead to future publications. Prof. John Woodhouse advised me during my research exchange visit at the University of Oxford and gave me access to the large computer cluster at the Department of Earth Sciences. This was becoming crucial for the second part of this thesis work, which would not have been possible without. Carl Tape (finishing his Ph.D. at Caltech now) was working with me on the membrane model. I am very grateful to Göran Ekström and Bill Fry for providing their excellent phase-anomaly databases. I also thank Prof. Jeannot Trampert to figure as external examiner for this thesis and for supplying his global phase-velocity maps to the research done here.

I was in the fortunate position of being supported as a Ph.D. of SPICE (Marie Curie Research Training Network). An essential help have been the SPICE workshops, where I appreciated a lot to discuss with Heiner Igel, Jean-Paul Montagner, Albert Tarantola, Ana Ferreira and Anne Sieminski. I also profited from interesting discussions with Adam Dziewonski, Guust Nolet, Barbara Romanowicz and Jeroen Tromp about this work. I'm thankful for the help and clarifying comments from Qinya Liu and Ying Zhou. Puis, je remercie aussi Julie Verbeke et Denis Lombardi d'avoir corrigé le résumé de ma thèse, évoquant la finesse de la langue française.

I want to mention two special thanks. The first goes to Domenico, because you gave me this opportunity after all. You made my life here very enjoyable. You have been very impressive to me in the way how you deal with the institute affairs: you made it very easy looking and you had always a joyful remark for everybody. Thank you very much, Domenico.

The second has to go to Lapo. Lapo is probably the person I have to thank most. You have been guiding me through this time, with live and work. You gave me the chance to learn more about science and I was always impressed about your insightful thoughts to my not so bright questions. You show a lot of patience and understanding, something I could never learn enough from you. After all, I tried to make you proud of the research done here, but I also hope you had some fun with it, as I did. Hopefully your expectations, by a tiny bit, were satisfied by this thesis work, which is all your merit, Lapo.

This thesis would not have been possible without the help of many more persons who have been truly inspiring during all this time. To all of you, I'm deeply thankful. It has been a precious time to live, to study and to work with you. There are many experiences and moments I will probably never forget. And some of you, I might even hope to meet you as friends the next time we see us. To friends and family, thanks a lot for making this experience very unique.

Institute of Geophysics, ETH Zurich, 2008 Daniel Peter

Curriculum vitae

DANIEL PETER
Greithstr.5
CH – 9402 Mörschwil

EDUCATION

Ph.D. in Geophysics, ETHZ (Swiss Federal Institute of Technology, Zurich), Switzerland, August 2004 - Mai 2008

Diploma in Physics, ETHZ (Swiss Federal Institute of Technology, Zurich), Switzerland, 1993 – 1998

1995-1996 exchange year studies at the Département de Physique, EPFL (École Polytechnique Fédérale Lausanne), Switzerland

Research activities accomplished at the Institute of Geophysics ETH Zurich:

- Implementation of a finite-differences software package 'membraneSphere' to model the propagation of membrane waves on a spherical shell
- 2-D sensitivity kernel database for surface wave phase-anomaly measurements
- Synthetic benchmark database of surface wave phase-anomaly measurements at different levels of heterogeneity

Research activities accomplished at the IACETH (Institute for Atmospheric and Climate Science, ETH Zurich):

- „snowflake recognition" software based on data by a 2D-Video-Distrometer
- diploma work called „strategies for ensemble prediction" about non-linear dynamics approaches for the short- and medium range weather prediction

Programming Languages: Fortan, C/C++, Python, Bash
OS Technologies: Linux Rocks cluster systems, OsX Xgrid

PROFESSIONAL PROFILE

- Independent programmer with training and expertise in feedforward backpropagation networks and genetic algorithms for optimisation, 3D-visualisations of complex user interfaces and Computer Telephony Integration
- Possess solid understanding of non-linear dynamics with Runge-Kutta solving algorithms and Monte Carlo ensemble generation especially with consideration of probabilistic density and singular vectors.
- Strong teamworker with troubleshooting and problem-solving skills.
- Experienced in international projects of software development.

PROFESSIONAL EXPERIENCE

Software Programmer, Petersvild, St.Gallen, Switzerland, May 2001 – July 2004

- Implemented genetic algorithms for optimisation of feed-forward backpropagation neural networks,
- 3D-visualisation applications for corporate communication,
- RAS (Remote Access Service) application to control modem calls.

Software Programmer, Enterprise Communications AG / Ansid AG, Winterthur, Switzerland, January 2001 – April 2001

- Performed trouble shooting in the development of Computer Telephony Integration (CTI) software products, mainly in system-analysis and program design.
- Implemented core components and test environments.

Software Programmer, Enterprise Communications AG, Zurich, Switzerland, February 1999 – May 2000

- Researched system-analysis and modelling of telephony interfaces of Microsoft (TAPI) and ECMA (TSAPI).
- Worked out analysis and design of core modules of the application set and their specification for outsourcing projects.
- Wrote technical feasibility studies and controlled their implementation in collaboration with the quality management.

Languages and Personal Information

German (mother language), English fluent, French fluent
Age 34, unmarried, Swiss citizenship